

國立臺灣大學理學院物理學系

博士論文

Department of Physics

College of Science

National Taiwan University

Doctoral Dissertation

局域性表面電漿子紅外線奈米光子元件之製作與應用

Preparation and applications of localized surface
plasmon polariton based infrared nanophotonic devices



鄭程文

Cheng-Wen Cheng

指導教授：施閔雄 博士

陳智泓 博士

Advisors: Min-Hsiung Shih, Ph.D.

Chyh-Hong Chern, Ph. D.

中華民國 101 年六月


June, 2012

國立臺灣大學博士學位論文
口試委員會審定書

局域性表面電漿子紅外線奈米光子元件之製作與應用
Preparation and applications of localized surface plasmon
based infrared nanophotonic devices

本論文係鄭程文君 (d95222035) 在國立臺灣大學物理學系、所
完成之博士學位論文，於民國 101 年 6 月 14 日承下列考試委員審查
通過及口試及格，特此證明

口試委員：

 陳智泓 (簽名)
(指導教授)

張書維

魏信坤
董奕鍾

致謝

在五年博士研究生涯中，充滿挑戰、挫折、忙碌、充實與成功。其研究成果要感謝曾經啟發、幫助與支持我的人。以下的文句絕對不足以表達描述我的致謝，但卻已在我生命的記憶中，留下不可抹去的足跡與色彩。

首先要感謝我的指導教授施閔雄老師，提供很好的研究環境與自由，並啟發我做研究的思維與方法。雖然研究過程有遇到挫折，但老師總能適時提供解決問題建議與想法，讓我能夠順利克服研究困難或避開一些不重要的次要問題。回想到此，能如其順利畢業與自我的成長，真是心中充滿感謝，感謝老師的栽培。

再者，我要感謝我TIGP同學Mohammed Nadhim Abbas的理論模擬與研究分享，沒有他的幫忙就沒今天的完整研究成果。在博士班期間，我必須感謝研究助理：怡君、湘諭與昭瑋幫忙處理行政瑣事和元件量測與製作，以及實驗室同學：功書和晉源研究上交流討論與光學量測。感謝學弟們：子倉、耀瑩、子庭與坤廷，在實驗上的大力幫助和許多做實驗熬夜戰鬥夜晚的陪伴。還有謝謝TIGP行政助理小姐亮慧和物理系辦季先生，學校行政事務的協助與幫忙。

最後，十分感謝與感恩我的家人，爺爺、奶奶、爸爸、媽媽、妹妹對我攻讀博士的支持，讓我在做研究時無後顧之憂，順利取得博士學位。

感謝曾經幫助我的人，期許在未來的日子自己能夠更精進並有所回饋，祝福大家一切平安順利。

應用奈米光子實驗室

鄭程文

中華民國一〇一年六月

中文摘要

在本論文中，我們利用表面電漿子和局域性表面電漿子的光學獨特性，在理論和實驗上展示一些主動與被動表面電漿元件，例如窄頻寬熱輻射器、與入射角和偏振無關紅外線濾波/吸收器、全向性紅外線偏振片和高性能折射率感測器。

根據克希荷夫熱輻射定律，利用金屬圓形碟盤結構，我們製作出一個高效率紅外線窄頻寬熱輻射器。對於 TE 與 TM 入射偏振光而言，此圓形結構具有一個局域性表面電漿子模態。此模態造成一個無偏振性窄頻寬熱輻射峰，其輻射波長與頻寬為 $4.27\mu\text{m}$ 和 $0.25\mu\text{m}$ 。其窄頻寬、下邊帶、高強度熱輻射特性，可應用在紅外線熱輻射光源。

關於應用在光學上的濾波/吸收器，我們通常需要高入射角度容忍度。不過，大多報告過的濾波/吸收器的濾波品質都與入射角度有關。在本文第四章，我們展示一個 T 型陣列結構製作在銀/二氧化矽/銀基板上，其結構具有一個與入射角度無關的表面電漿子模態。此結構可做為一個無入射角限制之反射式帶止濾波/吸收元件，應用在紅外線波段。藉由改變此結構幾何，其濾波頻帶位置可被調控。無入射角限制的特點，使此 T 型結構濾波元件設計，更加靈活彈性於光學波導模態共振濾波元件、表面電漿子濾波元件和多層表面電漿結構濾波元件。為了提升其元件吸收特性和降低製程技術困難，我們提出一個金屬圓形碟盤結構陣列，並具有一條局域性表面電漿子能帶，其入射角容許值接近達 90 度。有別於之前研究結果，我們實驗與嚴格耦合波理論模擬結果顯示，此局域性表面電漿子共振波長與圓形碟盤周期無關。利用與周期無關的特性，我們製作出一個大頻寬的紅外線吸收器，頻寬可到 2000nm。我們又發現調變圓形碟盤與單位晶胞面積比，一個高性能、廣角、無偏振性的雙波段吸收器可被實現，在寬廣入射角範圍下，其吸收器最大兩個吸收峰值可超過 84%。此結果，可靈活運用在吸收器設計，特別是在熱光電元件、感測器和偽裝等用途。

除了，金屬圓形碟盤結構陣列在第三與第四章所提的吸收與輻射特性外，我們

發現改變碟盤結構的長短軸比，其 TE 和 TM 共振峰可分開。因此，金屬橢圓形碟盤結構可以濾掉 TE 或 TM 反射光，做為一個便宜的全向性紅外線偏振片。在實驗上，使用碟盤結構長短軸比 0.65，發現極化率 99% 在波長 $4.12\mu\text{m}$ 為 TE 共振模態和 91% 在 $5.25\mu\text{m}$ 為 TM 共振模態，其實驗結果與模擬一致。TM 與 TE 共振模態消光比各為 20dB 和 15dB，藉由調變結構長短軸比，此消光比可進一步提高。

在最後第六章，我們利用橢圓碟盤陣列在蝕刻二氧化矽層的結構，成功製作出一個高性能表面電漿子折射率感測器，運作波長範圍從 1000nm 到 1800nm。感測器的靈敏度和品質因子各為 691nm/RIU 和 2.5，此靈敏度和品質因子數值，為目前為止近紅外線波段最高記錄。在本章中，我們會介紹一個新的概念有效提升其感測性能。此感測概念，有助維持局域性表面電漿子感測器性能。在將來工作中，我們與中央研究院應科中心董奕鐘教授合作，將靶細胞放在此元件上，做為細胞偵測用途。

在附錄 A 和 B，我們將介紹可調變表面電漿子能隙和感應光電壓在金光柵上的基礎性研究。根據上述 T 型陣列結構，當我們增加在二氧化矽夾層的金屬柱狀長度，表面電漿子能隙會存在出現。此能隙並非由額外半周期光柵造成，而是由於金屬-金屬和單層金屬折射率對比造成的。其能隙大小與金屬柱狀長度呈線性正比。此結構可廣範應用在能隙波導和缺陷共振腔雷射/發射器。

在附錄 B，我們與美國 Boise State 大學 Wan Kuang 教授合作，研究在金光柵上的感應光電壓。我們利用半古典電磁模型和弱非線性近似，來描述金光柵上的感應光電壓。此模型利用有限元素法來模擬並與量測結果比較。模擬感應光電壓是入射角和波長的函數，與我們實驗結果符合。此結果，提供一條描述更加詳細，研究光子-電子交互作用在元件上的路。

Abstract

In the thesis with the unique properties of surface plasmon polaritons (SPPs) and localized surface plasmon polaritons (LSPPs), a number of active and passive surface plasmon-based elements on chips were demonstrated numerically and experimentally, such as a narrow-band thermal emitter, wide-angle polarization independent infrared filters/absorbers, an omni-directional mid-infrared polarizer, and a high-performance index sensor.

Based on the Kirchhoff's law of thermal radiation with a round-shaped metal disk array, we demonstrated an efficient narrow-band thermal emitter in the MIR region. The structure exhibits one significant LSPP mode for both TM and TE polarizations, leading to an un-polarized narrow emission peak observed at $4.27\mu\text{m}$ with a FWHM of $0.25\mu\text{m}$. This kind of emission property with narrow bandwidth, low sideband and high intensity is very useful for the application in IR light sources.

For the applications in optical filters/absorber, large incident angle tolerance is always in demand. However, most of reported filters/absorbers are angle-dependent. In chapter 4, we demonstrated a T-shaped array in $A_g/\text{SiO}_2/A_g$ platform, showing an angle-independent LSPP mode. The structure can be as an angle-independent reflection-type band-stop filter/absorber in mid-infrared (MIR) region. The stop-band can also be adjusted by varying the structure geometry. The angle-independent feature makes the designed filter more flexible than a guided-mode resonance dielectric filter and a SPP filter as well as a plasmonic multilayer filter. To further improve the absorption performance and reduce the fabrication difficulty, a round-shaped metal disk array is applied because it has a LSPP band over a broad range of incidence angles of up to nearly 90° . Different from the previous work of the round-shaped metal disk array, our experimental results and numerical simulations performed by

using rigorous coupled-wave analysis (RCWA) clearly revealed that the resonant wavelength of the LSPP band is independent of the disk periodicity. Based on the periodic independent result, a broadband absorber with a bandwidth 2000nm operating at MIR region can be realized. We also found that by manipulating the disk area ratios per unit cell (ie area fill factors) and disk sizes, a high-performance, wide-angle, polarization-independent dual band absorber with two maximal absorptivity peaks greater than 84% over a wide of range of incident angles was experimentally achieved. The results demonstrated a substantial flexibility in absorber designs for applications in thermal photovoltaics, sensors, and camouflage.

In addition to the absorption and emission properties of the round-shaped disk structure in chapter 3 and chapter 4, we found that by tuning the aspect ratio b/a of the disk structure, both angle-independent TE- and TM- polarized resonant peaks can be separated. Therefore, the oval-shaped disk based structure can filter out completely one component of the light polarization and reflects perfectly the other component of the light polarization as a cheap omni-directional mid-IR polarizer. In our experiments, we found that such structure with $b/a=0.65$ ($a=1543\text{nm}$, $b=1009\text{nm}$) has a degree of polarization 91% at wavelength $4.12\mu\text{m}$ for TE mode and 99% at $5.25\mu\text{m}$ for TM mode, showing a good agreement with our simulation. The extinction ratios for both TM and TE modes are 20dB and 15dB, all of which can be further improved by tailoring the b/a axial ratio.

In the last chapter 6, based on the oval-shaped disk array structure with the SiO_2 layer etching, a highly performance plasmonic index sensor operating at wavelengths from 1000nm to 1800nm can be realized. The sensitivity $691\text{nm}/\text{RIU}$ and $\text{FOM}=2.5$ can be achieved as the highest record up to now in the NIR region. In the chapter, we also introduce a novel concept for the improvement in plasmonic sensing. The sensing strategy based on the concept can offer great potential to maintain the performance of

LSPP sensors. In the future work, we will cooperate with Professor Yi-Chung Tung at RCAS, Academic Sinica to produce target cells on such device for the cell detection.

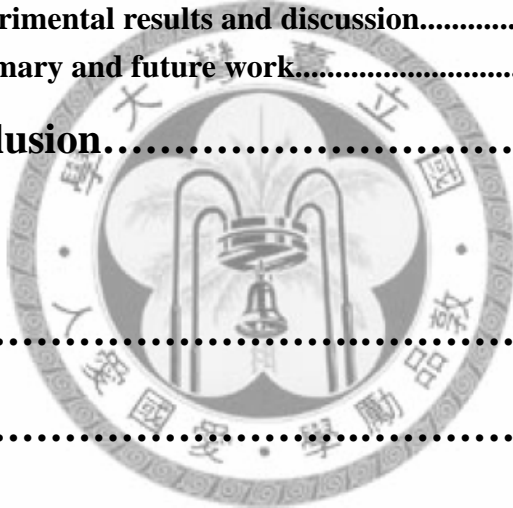
In Appendix A and B, fundamental studies of a tunable SPP band gap and photon induced voltage on an Au grating slab are introduced, respectively. Based on the T-shaped structure with the post under the top grating, a SPP band gap in Appendix A, can occur without using extra periodic grating $\Lambda_g/2$ when the post length is increased. The SPP band gap is attributed to the index contrast between the metal-metal and single metal regions, and is linearly proportional to the post length. Such a T-shaped structure with a tunable LSPP band gap can be widely exploited in various applications, such as band gap waveguides and defect cavity lasers/emitters.

In Appendix B, we cooperated with professor Wan Kuang's group at Boise State University, USA to study photon induced voltage on an Au grating slab. A semi-classical electrodynamic model is developed for the Au grating slab under the weak nonlinearity approximation. The model was solved by finite element method and compared with our measurements. The calculated photon induced voltage as a function of incident angles and wavelengths was found to be in qualitatively agreement with the experimental measurements, giving a pathway for the study of devices with more detailed photon electron interactions.

Contents

Chapter 1 Introduction and motivation.....	1
Chapter 2 Fundamentals of surface plasmon polaritons (SPPs) and localized surface plasmon polaritons (LSPPs)....	6
2.1 Basic principle of surface plasmon polaritons...6	
2.1.1 SPPs at a single dielectric/metal interface.....6	
2.1.2 SPPs at a dielectric/metal/dielectric double interface.....14	
2.1.3 SPPs at a metal/dielectric/metal double interface.....18	
2.2 Basic principle of localized surface plasmon polaritons.....	20
2.2.1 LSPPs at a sub-wavelength metal particle.....20	
2.2.2 LSPPs at a metal/dielectric/metal cavity.....25	
Chapter 3 Angle and polarization independent narrow-band thermal emitter made of metallic disk on SiO₂.....	30
3.1 Design and simulation.....31	
3.2 Experimental setup and results.....33	
3.3 Summary.....37	
Chapter 4 Wide-angle plasmonic infrared filters/absorber.38	
4.1 Design and simulation of the Ag/SiO ₂ /Ag T-shaped array39	
4.2 Fabrication of the Ag/SiO ₂ /Ag T-shaped array.....42	
4.3 FTIR measurement setup.....44	
4.4 Experimental results of the Ag/SiO ₂ /Ag T-shaped array.....45	
4.5 Design and simulation of the 2D metal disk array absorbers...48	
4.6 Fabrication of the 2D metal disk array absorbers.....42	
4.7 Experimental results of the 2D metal disk arrays.....51	
4.8 Summary.....57	

Chapter 5 Omni-directional mid-infrared (MIR) polarizer made of elliptical metal disk arrays.....	59
5.1 Design and simulation.....	60
5.2 Fabrication of the MIR polarizer.....	63
5.3 Experimental results and discussion.....	64
5.4 Summary.....	69
Chapter 6 Plasmonic index sensor made of elliptical metal disk array.....	70
6.1 Design and simulation.....	71
6.2 Fabrication of the Au/SiO ₂ cavity based structure.....	74
6.3 Experimental results and discussion.....	75
6.4 Summary and future work.....	78
Chapter 7 Conclusion.....	80
Appendix A.....	83
Appendix B.....	96
Appendix C.....	106
Bibliography.....	108



List of Figures

Fig. 1-1. Lycurgus cup is a Roman glass cup stored in the British Museum.....1

Fig. 2.1.1-1 Surface plasmons at interface between a metal and a dielectric material have a combined electromagnetic wave and surface charge distribution.....7

Fig. 2.1.1-2 Schematic diagram of TM-polarized fields in two media ϵ_1 and ϵ_2 when surface plasmon mode is excited by a polarized incident field. The surface charge density wave (or surface plasmon wave (SPW)) will propagate on a metal surface in the x direction.....8

Fig. 2.1.1-3 Dispersion relation of radiative and non-radiative surface plasmon modes where the dotted line is an asymptote of the blue curve for the radiative surface plasmon mode.....12

Fig. 2.1.1-4 Configuration of the ATR method where the evanescent field generated from the prism couples with the SPPs on the interface between ϵ_2 and ϵ_1 if k_x completely matches k_{SP}13

Fig. 2.1.1-5 By tuning the angle of incidence θ to the prism base in the ATR method, the SPPs at dielectric/metal interface can be excited when $k_x = k_{SP}$13

Fig. 2.1.2-1 Schematic diagram of TM-polarized fields in three media ϵ_1, ϵ_2 , and ϵ_3 . The metal thin film ϵ_2 lies between dielectric ϵ_1 and ϵ_3 . When SPPs are excited by an incoming TM-polarized field, surface plasmon waves (SPW) will propagate on both sides of the thin film surfaces.....14

Fig. 2.1.2-2 Distribution of fields for both high- and low- frequency modes in a symmetric plane of a metal thin film.....18

Fig. 2.2.1-1 Localised surface plasmon excitation by a metal nanoparticle in a nearly uniform quasi-static electric field.....21

Fig. 2.2.2-1 Lowest-order TM mode of metal/dielectric/metal (a) open and (b) closed cavities with a length of L.....26

Fig. 2.2.2-2 Schematic diagram of the investigated MD structure.....	27
Fig. 2.2.2-3(a) TM- and (b) TE-mode stimulated reflectance spectra of the MD structure.....	29
Fig. 2.2.2-4 TM-polarized $ H_y ^2$ distributions in one pitch of the MD array at 0.35 eV for normal incidence in (a) X-Y plane at Z=40 nm and (b) X-Z plane at Y=0 nm.....	29
Fig. 3.1-1 Absorption spectra ($1-R(\lambda)$) of the MD array structure with different diameters D for $\theta=0^\circ$ when $t=50\text{nm}$. The inset shows resonance wavelength (λ) versus the SiO_2 layer thickness (t) when $D=1000\text{nm}$	33
Fig. 3.2-1(a) Side view of thermal emitter chamber.....	34
Fig. 3.2-1(b) Top view of thermal emitter chamber.....	34
Fig. 3.2-2(a) Measured reflectance spectra of sample with $D=1.15\mu\text{m}$ and $\Lambda=3\mu\text{m}$...	35
Fig. 3.2-2(b) Simulated and measured emission spectrum of the IR emitter at 220 °C (blue line) and 300 °C (black line), respectively.....	36
Fig. 3.2-2(c) The measured emission spectrum for unpolarized, s-polarized (TE-polarized) and p-polarized (TM-polarized) for 220 °C.....	36
Fig. 4.1-1(a) Illustration of the T-shaped array structure. (b) Illustration of the reflection-type filter with the designed structure.....	39
Fig. 4.1-2(a) Stimulated reflectance spectra in x-z plane. (b) Stimulated reflectance spectra in y-z plane.....	41
Fig. 4.1-2(c) $ H_y ^2$ distribution at 0.35eV in x-z plane.....	42
Fig. 4.2-1 Fabrication process of the T-shaped array.....	42

Fig. 4.2-2(a) 45° angle SEM image of the T-shaped array. (b) Cross-sectional SEM image of the T-shaped structure.....	43
Fig. 4.3-1 Experimental setup for measurements.....	44
Fig. 4.4-1 (a) Incident (green), reflectance (red), and absorbance (blue) spectra at normal incidence. (b) Normal incident absorbance spectra from the T-shaped arrays with the widths $W_{Ag} = 300$ nm, 1540 nm, and 1910 nm. (c) Comparison of calculated and measured wavelengths of resonance.....	46
Fig. 4.4-2 Absorbance spectra from the T-shaped array with incident angles in x-z plane from 0° to 15°. The accuracy of the measured spectra is 3 nm.....	47
Fig. 4.6-1 SEM image of a fabricated MD structure.....	50
Fig. 4.7-1(a) Comparison of the calculated and measured wavelengths of resonances as functions of the disk diameter D	51
Fig. 4.7-1(b) Absorptivities at normal incidence of the 1 μ m MD arrays with several different periodicities Λ	53
Fig. 4.7-1(c) Absorptivities of the MD arrays with different diameters D for Λ fixed at 3 μ m.....	53
Fig. 4.7-1(d) Experimental peak absorptivity of the MD configuration as a function of its area-fill factor F	54
Fig. 4.7-2(a) Experimental absorptivity of the broadband absorber composed of the multi-sized disks with $D=800$ nm, 900 nm, 1.03 μ m, 1.12 μ m, 1.21 μ m, and 1.35 μ m and a SiO_2 spacer thickness, $t_{\text{SiO}_2}=32$ nm.....	55
Fig. 4.7-2(b) Absorptivity of the dual-band absorber consisting of two different disk sizes with dimensions $D=820$ nm, and 920 nm per unit cell when $t_{\text{SiO}_2}=80$ nm.....	56
Fig. 5.1-1 Illustration of the metallic disk array structure.....	60

Fig. 5.1-2 Dispersion relation of the metal disk structure for (a) TM mode and TE mode.....	61
Fig. 5.1-3(a) $ H_y ^2$ field distribution for TM-mode at 0.33eV in X-Z plane. (b) $ H_x ^2$ field distribution for TE-mode at 0.37eV in X-Z plane.....	62
Fig. 5.1-4 Calculated extinction ratio versus axial ratio.....	63
Fig. 5.2-1 SEM image of an elliptical disk array.....	64
Fig. 5.3-1(a) Measured reflectance spectra of the proposed metal disk structure for TM-polarized light (red), TE-polarized light (blue), and un-polarized light (green). The corresponding simulated spectra for TM- and TE- polarized light are shown in triangles and circles, respectively.....	66
Fig. 5.3-1(b) Polar diagram of the reflectance spectra versus polarizer rotating angle where the TE- and TM- polarizations of light by reflection are shown in red and blue curves.....	66
Fig. 5.3-2 Absorbance spectra at different incident angles from 0° to 15°	68
Fig. 5.3-3 Measured absorbance spectra for different minor axes from 585nm to 1511nm when a is fixed approximately 1511nm.....	68
Fig. 6.1-1 Illustration of the Au/SiO ₂ /Au cavity based structure.....	71
Fig. 6.1-2 $ H_y ^2$ distribution of the (a) round-shaped metal disk and (b) oval-shaped disk structures within one unit cell at the Y-Z plane when X=0.....	72
Fig. 6.1-3 (a) Illustration of the oval-shaped Au/SiO ₂ disk structure. (b) $ H_y ^2$ distribution within one unit cell at the Y-Z plane when X=0.....	72
Fig. 6.1-4 Numerical simulations of the sensitivities for the three structures.....	74
Fig. 6.2-1 SEM view of the oval-shaped Au/SiO ₂ disk structure.....	75

Fig. 6.3-1 Measured absorbance spectra of the three cavity based structures with liquid indices from 1 to 1.39.....

77

Fig. 6.3-2 Peak wavelength shifts in the TM-modes of the three structures.....

78

Fig. A-1 Schematic diagram of the T-shaped array structure.....

84

Fig. A-2 (a) Stimulated reflectance spectra of the multilayer structure with design parameters of $\Lambda_g=1 \mu\text{m}$, $W_{\text{top}}=550 \text{ nm}$, $t_{\text{top}}=200 \text{ nm}$, $W_{\text{post}}=200 \text{ nm}$, $d=0 \text{ nm}$, $t_{\text{post}}=0 \text{ nm}$, and $G_t=320 \text{ nm}$. (b) Stimulated reflectance spectra of the T-shaped structure when $d=50 \text{ nm}$, $t_{\text{post}}=170 \text{ nm}$, and $G_t=150 \text{ nm}$

85

Fig A-3 $|H_y|^2$ distribution at normal incidence in one period of (a) the Ag/SiO₂/Ag multilayer structure at the crossing point 0.87 eV, and (b) the first and (c) second branches of the T-shaped structure when $d=50 \text{ nm}$, $t_{\text{post}}=170 \text{ nm}$, and $G_t=150 \text{ nm}$

86

Fig. A-4 (a) Energy gap of the T-shaped structure varying with t_{post} when the W_{post} is fixed at 200 nm. (b) Energy gap versus W_{post} when the $t_{\text{post}}=170 \text{ nm}$

88

Fig. A-5 (a) The fabrication process of the T-shaped Ag/SiO₂/Ag structure. (b) SEM view of the T-shaped array with a displacement of $d=50 \text{ nm}$. The inset shows the details of the structure with a tilt angle of 25° at the ends of the grating slabs on the Ag posts. (c) AFM image profile of the T-shaped grating.....

89

Fig. A-6 Experimental absorbance spectra of the T-shaped grating ($\Lambda_g=1 \mu\text{m}$, $W_{\text{top}}=620 \text{ nm}$, $t_{\text{top}}=200 \text{ nm}$, $W_{\text{post}}=200 \text{ nm}$, $t_{\text{post}}=170 \text{ nm}$, and $G_t=150 \text{ nm}$) at normal incidence under TE-, TM-, and un-polarized illumination.....

91

Fig. A-7 Experimental absorbance spectra of (a) the multilayer structure ($\Lambda_g=1 \mu\text{m}$, $W_{\text{top}}=570 \text{ nm}$, $t_{\text{top}}=200 \text{ nm}$, $W_{\text{post}}=200 \text{ nm}$, $t_{\text{post}}=0 \text{ nm}$, and $G_t=320 \text{ nm}$) and (b) the T-shaped structure ($\Lambda_g=1 \mu\text{m}$, $W_{\text{top}}=620 \text{ nm}$, $t_{\text{top}}=200 \text{ nm}$, $W_{\text{post}}=200 \text{ nm}$, $t_{\text{post}}=170 \text{ nm}$, and $G_t=150 \text{ nm}$) for the different incident angles $\theta_i = 0^\circ, 5^\circ, \text{ and } 10^\circ$. In both (a) and (b), the simulated absorbance spectra are represented by black solid curves.....

93

Fig. A-8 1D photonic dispersion curve of the slab with the constituent dielectrics $n_1=1.414$ and $n_2=2.236$, when $\Lambda_g=1 \mu\text{m}$, $t_{\text{SiO}_2}=320 \text{ nm}$, and $W_{\text{post}}=200 \text{ nm}$ 94

Fig. B-1 Photon induced current density as calculated by the hydrodynamic model where the white open circles indicate the position of peak response.....100

Fig. B-2 SEM image of an Au grating. The inset shows the details of the grating....102

Fig. B-3 Induced voltage peaks as a function of incident angle for incident wavelengths of 1.2, 1.3, and 1.4 μm104

Fig. B-4 Measured photon induced voltage as a function of incident angle and wavelength..... 104





Chapter 1 Introduction and motivation

Surface plasmons (SPs) are quantized collective charge oscillations that occur at the interface between metal and dielectric. When SPs are coupled with photons, it can take various forms, ranging from freely propagating electron density wave along the interface (also called surface plasmon polaritons SPPs) to localized electron oscillations on the metal surface (also referred as localized surface plasmon polaritons LSPPs). The surface plasmon coupling effect has been employed for a long time by artists to generate vibrant colors in glass artefacts and in the staining of church windows. One of famous example is the Lycurgus cup (see Figure 1-1) dating from the 4th century A. D.



Fig. 1-1. Lycurgus cup is a Roman glass cup stored in the British Museum.

The glass cup shows a striking red when transmitted light is emitted from a light source placed inside the cup, while appearing green in reflection when light source is removed from the cup. This color change behavior is because of localized plasmonic

excitation of metallic particles in the glass matrix, leading to a bit change in the extinction (C_{ext}), scattering (C_{sca}), and absorption (C_{abs}) cross sections of the metallic particles.

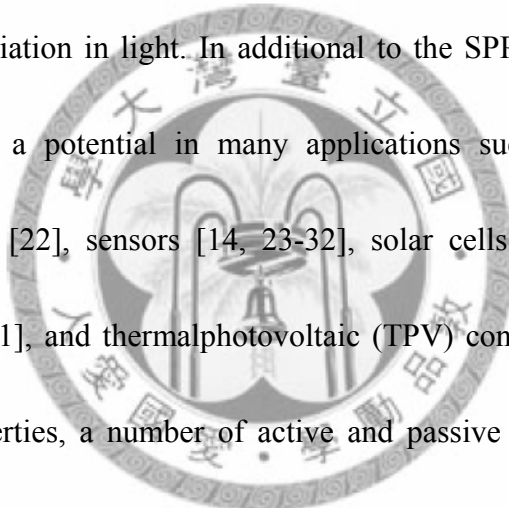
Some of the first scientific research in surface plasmons was observed at the beginning of the 20 century. In the year 1902, extraordinary phenomenon in optical reflection measurements on metallic gratings were first observed by Robert W. Wood [1]. In 1904, bright colors found in metal-doped glasses was described by Maxwell Garnett using the Drude theory of metals [2], and the electromagnetic properties of small spheres [3] were derived by Lord Rayleigh (J. W. Strutt) who won the Nobel Prize in physics in this year. Four years later, the theory of light scattering by spherical particles (particle size is about the same size as wavelength of incident light), which is well known as Mie theory [4], was developed by Gustav Mie. After some 50 years, in 1956, David Pines theoretically described the energy losses from electrons traveling through metals [5], corresponding to the collective oscillations of free electrons in the metal. He called such oscillations 'plasmons'. In 1957, Rufus Ritchie found that plasmons can exist near the surface of metals when electron energy losses occur [6]. A major advance in the study of surface plasmon polaritons was in 1968 (nearly 70 years after Wood's original observations) when Andreas Otto [7] and Erich Kretschman as well as Heinz Reather [8] developed a method called attenuated total

reflection (ATR). The method makes the excitation of surface plasmon polaritons easier and is accessible to many fields of research. In terms of the optical properties of localized surface plasmon polaritons, in 1970, Uwe Kreibig and Peter Zacharias first described the optical properties of gold and silver nanoparticles [9]. As the field, sometimes called plasmonics, continually developing, the coupling effect between the oscillating electrons and the electromagnetic field become more interesting and important in many applications.

The recent surge in surface plasmon-based applications is mostly focused on the research areas such as optical lithography, optical data storage, and high density photonic integrated circuits. The design and manufacturing in the research areas are all approaching fundamental physical limits. Such challenges could be overcome by using the properties of surface plasmons. Owing to many recent studies, a wide range of surface plasmon-based applications and techniques are developed, such as light guiding and manipulation at nanoscale [10, 11], surface-enhanced Raman scattering (SERS) from molecules adsorbed on small metal particles [12], single molecule biodetection [13, 14], optical transmission enhancement via sub-wavelength apertures [15], high resolution imaging below the diffraction limit [16], and so on.

In terms of communication systems, nm-sized electronic (metallic) circuits are inherently slow due to resistor-capacitor (RC) delay time limiting its

data-transmission speed, whereas optical (dielectric) circuits having high data-transmission speed are μ m-sized due to optical diffraction limit. However, it is fascinating to note that surface plasmon-based photonic circuits can combine the compactness of the electronic circuits with the broad bandwidth of the optical circuits. By employing the unique property of SPPs, most attractive surface plasmon components are mainly designed for reflectors [17], resonators [18, 19], and subwavelength waveguides [10, 20-22] with the guiding and confinement properties of electromagnetic radiation in light. In addition to the SPPs, the non-propagating LSPP property offers a potential in many applications such as filters [20, 21], metamaterial coatings [22], sensors [14, 23-32], solar cells [23-26], spasers [27], thermal emitters [28-31], and thermal photovoltaic (TPV) converters [32, 33]. Using those plasmonic properties, a number of active and passive surface plasmon-based elements have been developed, bringing the dream of a surface plasmon-based photonic integrated circuit into reality. A surface plasmon-based photonic integrated circuit includes a range of elements on a chip such as waveguides, modulators, filters, detectors, emitters and lasers. In the thesis with the unique properties of LSPPs, a narrow-band emitter [31], wide-angle plasmonic filter [21]/absorbers [34], an omni-directional mid-infrared polarizer, and a high-performance index sensor will be introduced and demonstrated.



The thesis content is organized as follows: in chapter 2, the basic theoretical background on SPPs at single and double interfaces and LSPPs on metal nanoparticles and metal/dielectric/metal cavities are looked at. Later on, we will develop and characterize a narrow-band thermal emitter in chapter 3, angle-independent filters/absorbers in chapter 4, a mid-infrared polarizer with an ultrahigh immunity to incident angles in chapter 5, and a high-performance plasmonic sensor in chapter 6. Finally, in chapter 7, we conclude the results and offer some suggestions for those localized surface plasmon-based devices.



Chapter 2 Fundamentals of surface plasmon polaritons (SPPs) and localized surface plasmon polaritons (LSPPs)

In the chapter, surface plasmon polaritons (SPPs) at a single dielectric/metal interface, the SPP propagation and decay lengths, and the condition of SPP excitation are introduced. In addition to the properties of the SPPs, SPP multiple-interface systems including dielectric/metal/dielectric (DMD) and metal/dielectric/metal (MDM) heterostructures are also looked at. As to localized surface plasmon polaritons (LSPPs), the LSPP properties of a sub-wavelength metal particle and MDM resonant cavities will be discussed.

2.1 Basic principle of surface plasmon polaritons

2.1.1 SPPs at a single dielectric/metal interface

Surface plasmon polaritons (SPPs) are electromagnetic waves coupled to the surface charge oscillations of a metal surface. The electron charges on the metal surface can perform coherent electron oscillations propagating along the surface (ie surface plasmon wave) as shown in Fig. 2.1.1-1. The surface charge distribution is described by

$$\sigma(x) = \sigma_0 \exp[i(k_x x - \omega t)] \quad (2.1.1-1)$$

where σ_0 is a constant for the surface charge density on the surface, and k_x is a

wave vector of the surface wave. At the surface boundary, a condition $\hat{z} \cdot (\vec{D}_2 - \vec{D}_1) = 4\pi\sigma$ must be satisfied where \hat{z} is a normal directed from side 1 to 2, and \vec{D}_i displacements are $\vec{D}_i = \epsilon_i \vec{E}_i$ with dielectric constants ϵ_i produced by bound charges, not free charges. Thus, from the surface condition formula, it can be understood that SPPs only occur in the field with TM modes (p-polarization), the modes on the plane of incidence allowing the existence of a normal component of electric field E_z .

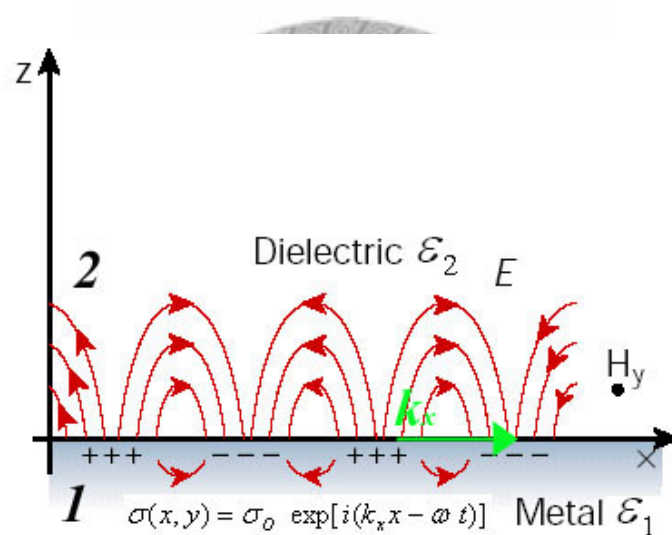


Fig. 2.1.1-1 Surface plasmons at interface between a metal and a dielectric material have a combined electromagnetic wave and surface charge distribution.(Adapted from [35])

Assuming there is an interface between a dielectric medium ($\mu_2=1, \epsilon_2$) and a metallic layer ($\mu_1=1, \epsilon_1$) where dielectric constants ϵ_i ($i = 1, 2$) are more generally allowed to be complex including bound charge and free charge contributions. When SPPs occur, the TM-polarized fields with a sinusoidal time dependence term $e^{-i\omega t}$ propagating through the layer system as seen in Fig. 2.1.1-2 are as follows:

$$\vec{H}_2 = (0, H_{2y}, 0) \exp i(k_{2x} x + k_{2z} z - \omega t) \quad (2.1.1-2)$$

$$\vec{E}_2 = (E_{2x}, 0, E_{2z}) \exp i(k_{2x} x + k_{2z} z - \omega t) \quad (2.1.1-3)$$

$$\vec{H}_1 = (0, H_{1y}, 0) \exp i(k_{1x} x - k_{1z} z - \omega t) \quad (2.1.1-4)$$

$$\vec{E}_1 = (E_{1x}, 0, E_{1z}) \exp i(k_{1x} x - k_{1z} z - \omega t) \quad (2.1.1-5)$$

where $z > 0$ for \vec{H}_2 and \vec{E}_2 , $z < 0$ for \vec{H}_1 and \vec{E}_1 , and $-\infty < x < \infty$ for all fields.

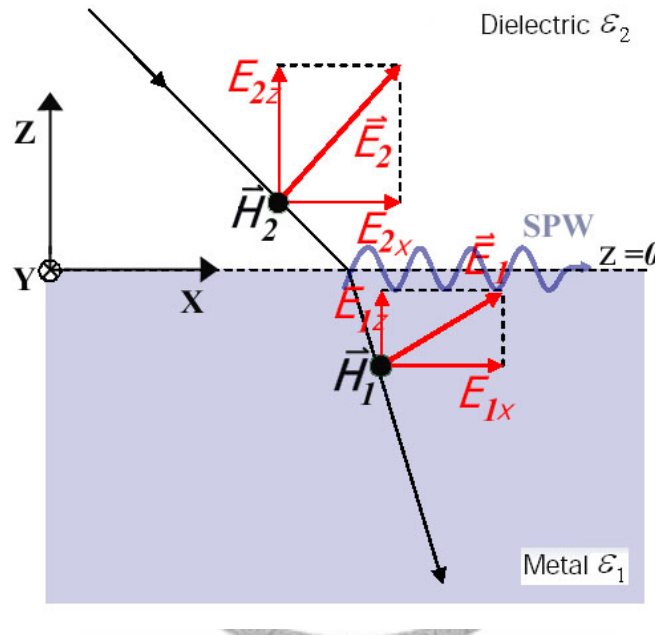


Fig. 2.1.1-2 Schematic diagram of TM-polarized fields in two media ϵ_1 and ϵ_2 when surface plasmon mode is excited by a polarized incident field. The surface charge density wave (or surface plasmon wave (SPW)) will propagate on a metal surface in the x direction.

These fields above at $z > 0$ and $z < 0$ fulfil the following Maxwell's equations:

$$\vec{\nabla} \cdot \epsilon_i \vec{E}_i = 0 \quad \text{and} \quad \vec{\nabla} \times \vec{E}_i = -\frac{1}{c} \frac{\partial \vec{H}_i}{\partial t} \quad i=1, \text{ and } 2 \quad (2.1.1-6)$$

$$\vec{\nabla} \cdot \vec{H}_i = 0 \quad \text{and} \quad \vec{\nabla} \times \vec{H}_i = \epsilon_i \frac{1}{c} \frac{\partial \vec{E}_i}{\partial t} \quad i=1, \text{ and } 2 \quad (2.1.1-7)$$

From the Maxwell's equations, the boundary conditions at $z=0$ are given by

$$E_{2x} = E_{1x}, \quad H_{2y} = H_{1y}, \quad \text{and} \quad \varepsilon_2 E_{2z} = \varepsilon_1 E_{1z} \quad (2.1.1-8)$$

In addition, the existence of the boundary conditions at $z=0$ must be satisfied at all points on the plane at all time, which means the spatial and time variation of all fields must be the same. Consequently, the phase factors at $z=0$ we require are [36]

$$(\vec{k}_2 \cdot \vec{r})|_{z=0} = (\vec{k}_1 \cdot \vec{r})|_{z=0} \quad (2.1.1-9)$$

By the phase factor requirement at $z=0$, \vec{k}_2 and \vec{k}_1 would be located on the same plane of incidence with $k_{2x} = k_{1x} = k_x$ and $k_{2y} = k_{1y} = 0$. With $k_{2x} = k_{1x} = k_x$, the boundary condition $H_{2y} = H_{1y}$ and (2.1.1-7) into which (2.1.1-2) to (2.1.1-5) substitute, we can obtain the following simultaneous linear equations in 2 unknowns:

$$\begin{aligned} H_{1y} - H_{2y} &= 0 \\ \frac{k_{1z}}{\varepsilon_1} H_{1y} + \frac{k_{2z}}{\varepsilon_2} H_{2y} &= 0 \end{aligned} \quad (2.1.1-10)$$

To obtain non-trivial solution of the simultaneous equations (ie H_{1y} and H_{2y} are non-zero), the determinant $\det(A)$ of the equations must be zero, where

$$\det(A) = \begin{vmatrix} 1 & -1 \\ \frac{k_{1z}}{\varepsilon_1} & \frac{k_{2z}}{\varepsilon_2} \end{vmatrix} = \frac{k_{1z}}{\varepsilon_1} - \frac{k_{2z}}{\varepsilon_2} = 0 \quad (2.1.1-11)$$

and $k_{iz}^2 = \varepsilon_i \left(\frac{\omega^2}{c^2}\right) - k_x^2$ $i=1, \text{ and } 2$.

From equation (2.1.1-11) together with $k_{iz}^2 = \varepsilon_i \left(\frac{\omega^2}{c^2}\right) - k_x^2$ $i=1, \text{ and } 2$, the well-known dispersion relation for the case of interface SPPs is obtained:

$$k_x = \frac{\omega}{c} \sqrt{\frac{\varepsilon_1 \varepsilon_2}{\varepsilon_1 + \varepsilon_2}} \quad (2.1.1-12)$$

In general, $k_x(\omega)$ can be complex. If we assume $\varepsilon_1 = \varepsilon_1' + i\varepsilon_1''$ and $|\varepsilon_1''| \ll |\varepsilon_1'|$,

$k_x(\omega) = k_x' + ik_x''$ can be obtained with

$$k_x' = \frac{\omega}{c} \sqrt{\frac{\varepsilon_2 \varepsilon_1'}{\varepsilon_2 + \varepsilon_1'}} \quad (2.1.1-13)$$

$$k_x'' = \frac{\omega}{c} \left(\frac{\varepsilon_2 \varepsilon_1'}{\varepsilon_2 + \varepsilon_1'} \right)^{3/2} \frac{\varepsilon_1''}{2(\varepsilon_1')^2} \quad (2.1.1-14)$$

where k_x' determines the wave propagation of surface plasmons, and k_x'' is related to internal absorption produced by ε_1'' .

The propagating SPP wave will be damped with an energy attenuation length L (also called propagation length) defined as $L = \frac{1}{2k_x''}$. As can be seen, when the metal loss associated with ε_1'' is increased, L tends to be decreased. Regarding the penetration depth δ (also called skin depth) of the SPP wave, the depth is defined as the SPP field along z-axis falling off exponentially with a value of e^{-1} . δ is therefore given by $\frac{1}{\text{Im}(k_{iz})} = \frac{1}{\sqrt{k_x^2 - \varepsilon_i \left(\frac{\omega^2}{c^2}\right)}}$. For a dielectric/metal interface, $\varepsilon_1' < 0$

and $\varepsilon_2 > 0$ ($|\varepsilon_2| < |\varepsilon_1'|$) which in turn results $\delta_2 > \delta_1$. The relation between the

complex refractive index $\tilde{n} = n + ik$ and permittivity $\varepsilon = \varepsilon' + i\varepsilon''$ is given by

$\tilde{n}^2 = \mu\varepsilon$ where $\mu=1$. This explicitly yields

$$\varepsilon' = n^2 - k^2 \quad \text{and} \quad \varepsilon'' = 2nk \quad (2.1.1-15)$$

To further simplify the dispersion relation $k_x(\omega)$ in (2.1.1-12), if we just concern

k_x real with ε_2 (pure dielectric medium) and $\varepsilon_1 = 1 - \frac{\omega_p^2}{\omega^2}$ where ω_p called plasma

frequency (ε_1 produced by Drude model for a simple metallic medium), then

$k_x(\omega) = k'_x \equiv k_{SP}$ can be written as

$$k_{SP} = k_x = \frac{\omega}{c} \sqrt{\frac{\varepsilon_2(1 - \frac{\omega_p^2}{\omega^2})}{\varepsilon_2 + (1 - \frac{\omega_p^2}{\omega^2})}} \quad (2.1.1-16)$$

As $k_x \rightarrow \infty$, there is a horizontal asymptote $\omega = \frac{\omega_p}{\sqrt{\varepsilon_2 + 1}}$. Further from (2.1.1-16),

$k_{iz}^2 = \varepsilon_i(\frac{\omega^2}{c^2}) - k_x^2$ becomes

$$k_{1z} = \frac{\omega}{c} \sqrt{\frac{(1 - \frac{\omega_p^2}{\omega^2})^2}{\varepsilon_2 + (1 - \frac{\omega_p^2}{\omega^2})}} \quad (2.1.1-17)$$

$$k_{2z} = \frac{\omega}{c} \sqrt{\frac{\varepsilon_2^2}{\varepsilon_2 + (1 - \frac{\omega_p^2}{\omega^2})}} \quad (2.1.1-18)$$

when $\omega \leq \frac{\omega_p}{\sqrt{\varepsilon_2 + 1}}$ (ie $\varepsilon_2 + (1 - \frac{\omega_p^2}{\omega^2}) < 0$), the SPP wave is also called “nonradiative”

surface plasmon polaritons because both k_{1z} and k_{2z} from (2.1.1-17) and (2.1.1-18) are

imaginary, leading to exponentially radiation decay near the surface boundary. In

contrast, when $\omega > \frac{\omega_p}{\sqrt{\varepsilon_2 + 1}}$, it is called “radiative” surface plasmon polaritons.

When $\omega < \omega_p$, the permittivity ε_1 of metal becomes $\varepsilon_1 < 0$. If the SPPs exists with k_x

in (2.1-11) required to be $k_x > 0$, $\varepsilon_1\varepsilon_2 < 0$ and $(\varepsilon_1 + \varepsilon_2) < 0$ must be satisfied.

The dispersion relation from (2.1.1-16) can be sketched as seen in Fig. 2.1.1-3. It

can be seen that the wave vector k_{SP} of nonradiative surface plasmons is larger than

that of an incident light with an angle θ_o . Therefore, nonradiative SPPs will not happen naturally when light strikes on a metallic surface.

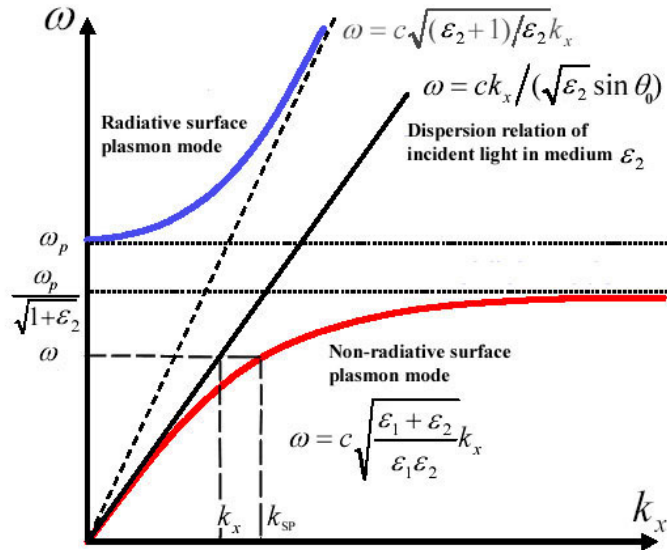


Fig. 2.1.1-3 Dispersion relation of radiative and non-radiative surface plasmon modes where the dotted line is an asymptote of the blue curve for the radiative surface plasmon mode.

There are many ways to excite the SPPs such as diffraction on a grating, diffraction on surface features, excitation with an SNOM (scanning near-field optical microscopy) probe, and excitation with a prism [37]. One of common ways is to use attenuated total reflection (ATR) coupler to excite SPPs. As to the configuration of the ATR coupler shown in Fig. 2.1.1-4, a prism with $\epsilon_3 \geq \epsilon_2$ is utilised to generate an evanescent light wave with $k_x = \sqrt{\epsilon_3}(\omega/c)\sin\theta$ where $\theta \geq \theta_c$ (critical angle). By adjusting θ into a proper angle, the wave vector k_x from the prism would completely match the SPPs of wave vector k_{sp} shown in Fig.2.1.1-5, which in turn result in the

excitation of SPPs.

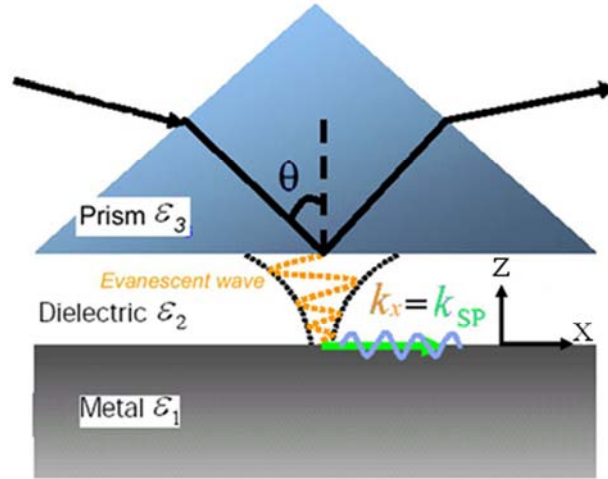


Fig. 2.1.1-4 Configuration of the ATR method where the evanescent field generated from the prism couples with the SPPs on the interface between ϵ_2 and ϵ_1 if k_x completely matches k_{SP} .

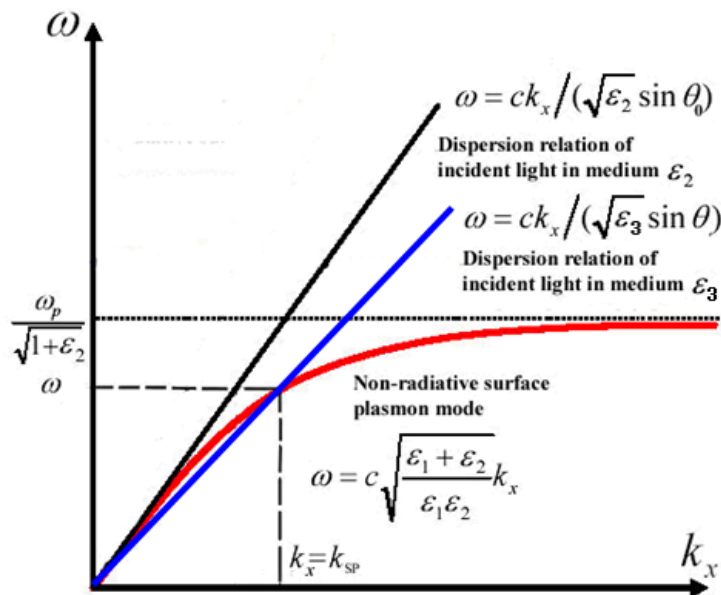


Fig. 2.1.1-5 By tuning the angle of incidence θ to the prism base in the ATR method, the SPPs at dielectric/metal interface can be excited when $k_x = k_{SP}$.

2.1.2 SPPs at a dielectric/metal/ dielectric double interface

Up to now we have treated the physics of SPP propagating on a smooth interface of dielectric/metal. SPPs also exist on thin films. Their properties depend on the thickness of the thin film system and the dielectric medium on both sides of the thin film. For the case of SPPs on the thin films, let us first concern a thin film system with a thickness d as displayed in Fig. 2.1.2-1. The metallic thin film between asymmetric dielectrics ε_1 and ε_2 allows the excitation of SPPs by irradiation with TM-polarized light.

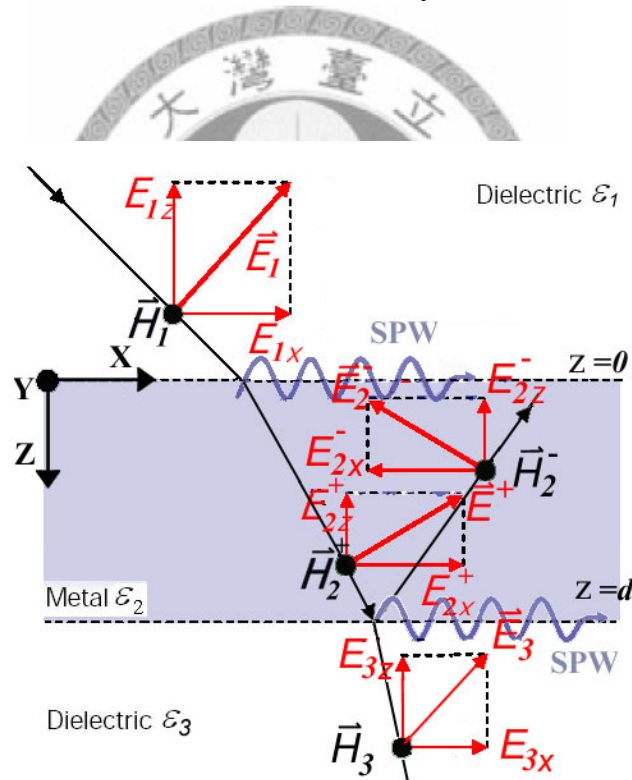


Fig. 2.1.2-1 Schematic diagram of TM-polarized fields in three media ε_1 , ε_2 , and ε_3 . The metal thin film ε_2 lies between dielectric ε_1 and ε_3 . When SPs are excited by an incoming TM-polarized field, surface plasmon waves (SPW) will propagate on both sides of the thin film surfaces.

The TM-polarized fields in the thin film layer system are given by

in zone 1 where $z < 0$,

$$\vec{H}_1 = (0, H_{1y}, 0) \exp i(k_{1x} x - k_{1z} z - \omega t) \quad (2.1.2-1)$$

$$\begin{aligned} \vec{E}_1 &= (E_{1x}, 0, E_{1z}) \exp i(k_{1x} x - k_{1z} z - \omega t) \\ &= \left(\frac{-c}{\omega}\right) \frac{H_{1y}}{\varepsilon_1} (k_{1z}, 0, k_{1x}) \exp i(k_{1x} x - k_{1z} z - \omega t) \end{aligned} \quad (2.1.2-2)$$

in zone 2 where $0 < d < z$,

$$\vec{H}_2 = [(0, H_{2y}^+, 0) \exp i(k_{2z}) + (0, H_{2y}^-, 0) \exp i(-k_{2z})] \exp i(k_{2x} x - \omega t) \quad (2.1.2-3)$$

$$\begin{aligned} \vec{E}_1 &= [(E_{2x}^+, 0, E_{2z}^+) \exp i(k_{2z}) + (E_{2x}^-, 0, E_{2z}^-) \exp i(-k_{2z})] \exp i(k_{2x} x - \omega t) \\ &= \left(\frac{-c}{\omega}\right) \frac{1}{\varepsilon_2} [H_{2y}^+(-k_{2z}, 0, k_{2x}) \exp i(k_{2z}) + H_{2y}^-(k_{2z}, 0, k_{2x}) \exp i(-k_{2z})] \exp i(k_{2x} x - \omega t) \end{aligned} \quad (2.1.2-4)$$

in zone 3 where $z < d$,

$$\vec{H}_3 = (0, H_{3y}, 0) \exp i(k_{3x} x + k_{3z} z - \omega t) \quad (2.1.2-5)$$

$$\begin{aligned} \vec{E}_3 &= (E_{3x}, 0, E_{3z}) \exp i(k_{3x} x + k_{3z} z - \omega t) \\ &= \left(\frac{-c}{\omega}\right) \frac{H_{1y}}{\varepsilon_3} (-k_{3z}, 0, k_{3x}) \exp i(k_{3x} x + k_{3z} z - \omega t) \end{aligned} \quad (2.1.2-6)$$

where \vec{E}_i and \vec{H}_i ($i=1,2,\text{and }3$) satisfy the equation (2.1.1-7).

With the phase factor requirement mentioned in (2.1.1-9) at $z=0$, and $z=d$, the wave vectors of the fields at different zones have following relations:

$$k_{1x} = k_{2x} = k_{3x} \equiv k_x \quad \text{and} \quad k_{1y} = k_{2y} = k_{3y} = 0 \quad (2.1.2-7)$$

By (2.1.2-7) with the boundary conditions where the tangential components of \vec{E}_i

and \vec{H}_i (i=1,2,and 3) are continuous at z=0 and z=d, we therefore obtain:

at z=0,

$$H_{1y} = H_{2y}^+ + H_{2y}^- \quad (2.1.2-8)$$

$$\frac{k_{1z}}{\varepsilon_1} (-H_{1y}) = \frac{k_{2z}}{\varepsilon_2} H_{2y}^+ - \frac{k_{2z}}{\varepsilon_2} H_{2y}^- \quad (2.1.2-9)$$

at z=d,

$$H_{2y}^+ \exp i(k_{2z}d) + H_{2y}^- \exp i(-k_{2z}d) = H_{3y} \exp i(k_{3z}d) \quad (2.1.2-10)$$

$$\frac{k_{2z}}{\varepsilon_2} H_{2y}^+ \exp i(k_{2z}d) - \frac{k_{2z}}{\varepsilon_2} H_{2y}^- \exp i(-k_{2z}d) = \frac{k_{3z}}{\varepsilon_3} H_{3y} \exp i(k_{3z}d) \quad (2.1.2-11)$$

where (2.1.2-8) and (2.1.2-10) are for the tangential components of \vec{H}_i continuous at z=0 and z=d. As to (2.1.2-9) and (2.1.2-11), they have tangential components of \vec{E}_i

continuous at z=0 and z=d. These four equations above from (2.1.2-8) to (2.1.2-11) can be rearranged to be

$$H_{2y}^+ (\varepsilon_2 k_{1z} + \varepsilon_1 k_{2z}) + H_{2y}^- (\varepsilon_2 k_{1z} - \varepsilon_1 k_{2z}) = 0 \quad (2.1.2-12)$$

$$H_{2y}^+ \exp i(k_{2z}d) (\varepsilon_2 k_{3z} - \varepsilon_3 k_{2z}) + H_{2y}^- \exp i(-k_{2z}d) (\varepsilon_2 k_{3z} + \varepsilon_3 k_{2z}) = 0 \quad (2.1.2-13)$$

If H_{2y}^+ and H_{2y}^- are required not to be zero, then the following relation in (2.1.2-14)

must be satisfied.

$$\begin{vmatrix} (\varepsilon_2 k_{1z} - \varepsilon_1 k_{2z}) & (\varepsilon_2 k_{1z} + \varepsilon_1 k_{2z}) \\ -(\varepsilon_3 k_{2z} - \varepsilon_2 k_{3z}) \exp i(k_{2z}d) & (\varepsilon_2 k_{3z} + \varepsilon_3 k_{2z}) \exp i(-k_{2z}d) \end{vmatrix} = 0 \quad (2.1.2-14)$$

If the metallic thin film is between symmetric dielectrics (ie $\varepsilon_1 = \varepsilon_3 \equiv \varepsilon_1$), (2.1.2-4)

can be simply rearranged and split into two following independent equations.

$$\omega^+ \equiv \varepsilon_2 k_{1z} - i\varepsilon_1 k_{2z} \tan\left(\frac{k_{2z}d}{2}\right) = 0 \quad (2.1.2-15)$$

$$\omega^- \equiv \varepsilon_2 k_{1z} + i\varepsilon_1 k_{2z} \cot\left(\frac{k_{2z}d}{2}\right) = 0 \quad (2.1.2-16)$$

ω^+ is called odd mode (symmetric SPP mode) while ω^- is called even mode (anti-symmetric SPP mode), all with respect to the x-component of \vec{E} fields (the transverse components E_z) at the thin film mid-plane [38].

When k_x is extremely large, the above dispersion relation of SPPs (2.1.2-15)

and (2.1.2-16) together with $k_{iz} = \sqrt{\varepsilon_i \left(\frac{\omega^2}{c^2}\right) - k_x^2}$ (ie $k_{1z} = k_{2z} = ik_x$ as $k_x \rightarrow \infty$),

$\tan(ix) = i \tanh(x)$, and $\cot(ix) = -i \coth(x)$ yields

$$\omega^+ \equiv \frac{\varepsilon_1 + \varepsilon_2}{\varepsilon_1 - \varepsilon_2} + \exp(-k_x d) = 0 \quad (2.1.2-17)$$

$$\omega^- \equiv \frac{\varepsilon_1 + \varepsilon_2}{\varepsilon_1 - \varepsilon_2} - \exp(-k_x d) = 0 \quad (2.1.2-18)$$

Substituting $\varepsilon_2 = 1 - \frac{\omega_p^2}{\omega^2}$ into (2.1.2-17) and (2.1.2-18), ω^\pm are obtained as follows

[39]:

$$\omega^\pm = \frac{\omega_p}{\sqrt{1 + \varepsilon_1}} \left(\frac{1 \pm \exp(-k_x d)}{1 \mp \frac{\varepsilon_1 - 1}{\varepsilon_1 + 1} \exp(-k_x d)} \right)^{1/2} \quad (2.1.2-19)$$

where $\omega^+ > \omega^-$. It is interesting to note that in the case of the symmetric dielectric/metal/dielectric system, the SPPs on both sides of the thin film will be coupled. As a result, the SPP resonance frequencies are split into two ω^\pm where ω^+ a high-frequency mode (electric field E_x asymmetric to the plane at $z=d/2$), and ω^- a low-frequency mode (electric field E_x symmetric to the plane at $z=d/2$), as shown in

Fig. 2.1.2-2.

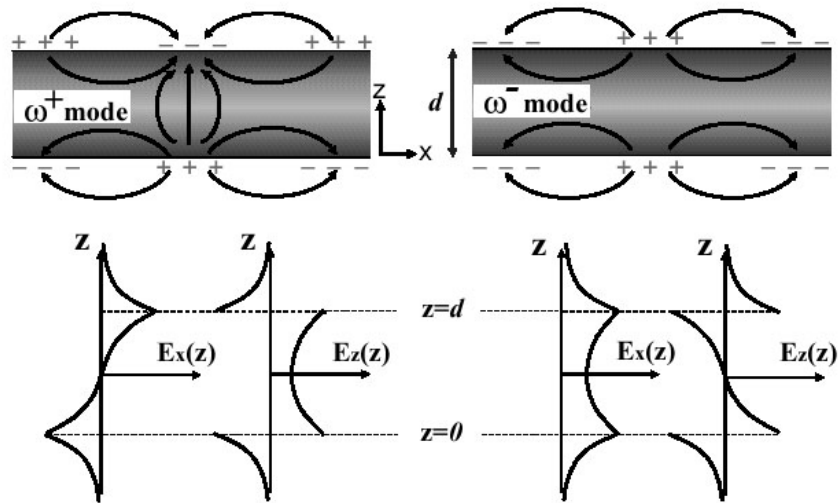


Fig. 2.1.2-2 Distribution of fields for both high- and low- frequency modes in a symmetric plane of a metal thin film. (Adapted from [40])

The odd mode is considerably smaller attenuation than the even mode because of the two different E_x field confinement in the metal film related to metal loss. The odd mode is therefore conventionally called long-range SPP (ie longer L) and the even one short-range SPP (ie shorter L). When the film thickness d becomes larger (or say $k_x d \gg 1$), the SPPs on both sides become uncoupled with $\omega^\pm \rightarrow \omega_p / \sqrt{\epsilon_1 + 1}$ which is identical to the SPPs on a dielectric/metal interface as $k_x \rightarrow \infty$.

2.1.3 SPPs at a metal/dielectric/metal double interface

Let us now consider the SPP modes (or gap SPP modes) in the symmetric metal/dielectric/metal configuration with the thickness d of a thin dielectric layer sandwiched between two metal surfaces. The deduction of the gap SPP dispersion

relations is exactly the same as the case of the dielectric/metal/dielectric configuration as we define $\varepsilon_1 = \varepsilon_3 = \varepsilon_m$ (metal) and $\varepsilon_2 = \varepsilon_d$ (dielectric). With (2.1.2-15) and (2.1.2-16), the dispersion relations are as follows:

$$\omega^+ \equiv \tanh\left(i \frac{k_{dz} d}{2}\right) = \frac{\varepsilon_d k_{mz}}{\varepsilon_m k_{dz}} \quad (2.1.3-1)$$

$$\omega^- \equiv \coth\left(i \frac{k_{dz} d}{2}\right) = \frac{\varepsilon_d k_{mz}}{\varepsilon_m k_{dz}} \quad (2.1.3-2)$$

For small gap widths (ie $d \rightarrow 0$), one can use the approximation $\tanh(ix) \sim ix$ and $\coth(ix) \sim (1/ix)$. Therefore, (2.1.3-1) and (2.1.3-2) become the following expressions:

$$\omega^+ \equiv \frac{k_{mz}}{\varepsilon_m} = \frac{k_{dz}}{\varepsilon_d} \left(\frac{ik_{dz} d}{2} \right) \quad (2.1.3-3)$$

$$\omega^- \equiv \frac{k_{mz}}{\varepsilon_m} = \frac{i2}{\varepsilon_d d} \quad (2.1.3-4)$$

With $k_{dz}^2 - k_{mz}^2 = (\varepsilon_d - \varepsilon_m)k_0^2$, (2.1.3-3) and (2.1.3-4) can be deduced as a function of k_{dz} shown below:

$$\omega^+ \equiv k_{dz}^2 \left(1 + k_{dz}^2 \left(\frac{\varepsilon_m}{\varepsilon_d} \right)^2 \left(\frac{d}{2} \right)^2 \right) = (\varepsilon_d - \varepsilon_m)k_0^2 \quad (2.1.3-5)$$

$$\omega^- \equiv k_{dz}^2 + \left(\frac{\varepsilon_m}{\varepsilon_d} \right)^2 \left(\frac{d}{2} \right)^2 = (\varepsilon_d - \varepsilon_m)k_0^2 \quad (2.1.3-6)$$

For the ω^+ gap SPP guiding mode, the k_x derived from (2.1.3-5) with

$k_{dz}^2 = \varepsilon_d k_0^2 - k_x^2$ becomes [41]

$$k_x \cong k_0 \left(\varepsilon_d + \frac{1}{2} \left(\frac{2\varepsilon_d}{d\varepsilon_m k_0} \right)^2 + \sqrt{\left(\frac{2\varepsilon_d}{d\varepsilon_m k_0} \right)^2 (\varepsilon_d - \varepsilon_m + \frac{1}{4} \left(\frac{2\varepsilon_d}{d\varepsilon_m k_0} \right)^2)} \right)^{1/2} \quad (2.1.3-7)$$

Thus, the effective index of the guiding mode ω^+ is given by

$$n_{eff} = \frac{k_x}{k_0} = \left(\varepsilon_d + \frac{1}{2} \left(\frac{2\varepsilon_d}{d\varepsilon_m k_0} \right)^2 + \sqrt{\left(\frac{2\varepsilon_d}{d\varepsilon_m k_0} \right)^2 (\varepsilon_d - \varepsilon_m + \frac{1}{4} \left(\frac{2\varepsilon_d}{d\varepsilon_m k_0} \right)^2)} \right)^{1/2} \quad (2.1.3-8)$$

As can be seen, the effective index is dramatically increased as the gap width become narrow. Similarly to the ω^+ mode, the k_x of the ω^- guiding mode is

$$k_x \cong \sqrt{\varepsilon_m k_0^2 + \left(\frac{2\varepsilon_m}{d\varepsilon_d} \right)^2} \quad (2.1.3-9)$$

However, for the ω^- mode, there is a limitation of the dielectric layer thickness d .

When $d < d_c$ (critical thickness), the ω^- mode does not exist any more. Because of

$k_{dz} > 0$ required for the ω^- guiding mode in (2.1.3-6), the critical thickness d_c can

be obtained and given by

$$d_c = \frac{2}{k_0 \sqrt{\varepsilon_d - \varepsilon_m}} \left(\frac{-\varepsilon_m}{\varepsilon_d} \right) \quad (2.1.3-10)$$

2.2 Basic principle of localized surface plasmon polaritons

2.2.1 LSPPs at a sub-wavelength metal particle

For a spherical metallic particle $\varepsilon_m(\omega)$ with its radius $a \ll \lambda$ (incoming wavelength) placed in a surrounding medium ε , the conduction electrons inside the particle driven by an incoming field $\vec{E} = E_0 \hat{z}$ move all in phase, leading to the build-up of induced charges on the particle surface. The charges act like an induced dipole \vec{p} (see Fig. 2.2.1-1), giving raise to an effective restoring force that allows a

non-propagating resonance (ie localized resonance) at a specific frequency. Due to $a \ll \lambda$, the spatially varying incoming field around the spherical particle can be treated as a uniform static field, which is also called a quasi-static approximation.

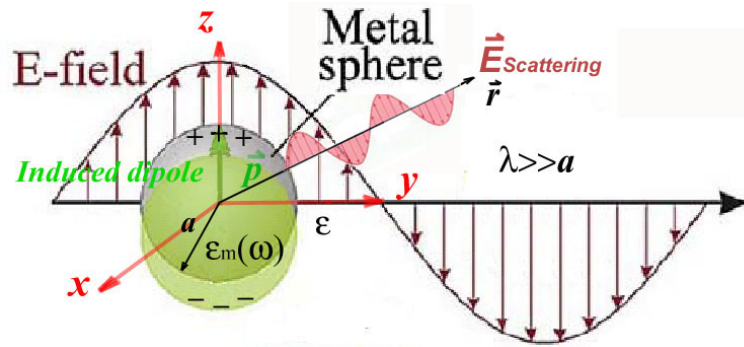


Fig. 2.2.1-1 Localised surface plasmon excitation by a metal nanoparticle in a nearly uniform quasi-static electric field.

In the electrostatic approach, we start to solve the Laplace equation $\nabla^2\phi = 0$ for the potential ϕ of the metal particle. Because of the azimuthal symmetry of the problem, the solution for the potentials inside and outside the spherical particle can be written as

$$\phi_{in}(r, \theta) = \sum_{l=0}^{\infty} A_l r^l P_l(\cos\theta), \quad r \leq a \quad (2.2.1-1)$$

$$\phi_{out}(r, \theta) = -E_0 r \cos\theta + \sum_{l=0}^{\infty} \frac{B_l}{r^{l+1}} P_l(\cos\theta), \quad r \geq a \quad (2.2.1-2)$$

where $P_l(\cos\theta)$ are the Legendre polynomials of order l and θ the angle between the position vector \vec{r} and z-axis. The coefficients A_l and B_l can be

determined by the following boundary conditions at the sphere surface $r = a$.

$$\phi_{in}(a, \theta) = \phi_{out}(a, \theta) \quad (2.2.1-3)$$

$$-\varepsilon_m \frac{\partial \phi_{in}(r, \theta)}{\partial r} \Big|_{r=a} = -\varepsilon \frac{\partial \phi_{out}(r, \theta)}{\partial r} \Big|_{r=a} \quad (2.2.1-4)$$

Therefore, the solution of the potential for the particle is given by

$$\phi_{in}(r, \theta) = -\left(\frac{3\varepsilon}{\varepsilon_m + 2\varepsilon}\right)E_0 r \cos \theta, \quad r \leq a \quad (2.2.1-5)$$

$$\phi_{out}(r, \theta) = -E_0 r \cos \theta + \frac{\bar{p} \cdot \hat{r}}{4\pi\varepsilon r^2}, \quad r \geq a \quad (2.2.1-6)$$

where \bar{p} induced dipole moment is defined as $\bar{p} = \varepsilon\alpha E_0$ with the polarizability

$\alpha = 4\pi a^3 \frac{\varepsilon_m - \varepsilon}{\varepsilon_m + 2\varepsilon}$. It is apparent that under the condition $\varepsilon_m = -2\varepsilon$, the \bar{p} (or

polarizability) experiences a resonant enhancement. By the Drude model

assumption $\varepsilon_m = 1 - \frac{\omega_p^2}{\omega^2}$, the resonant frequency is estimated to be $\omega = \frac{\omega_p}{\sqrt{1+2\varepsilon}}$

which is also called Fröhlich frequency.

For the most general smooth metallic particle, its shape is an ellipsoid with

principal axes $a > b > c$, the particle surface specified by

$$\frac{x^2}{a^2} + \frac{y^2}{b^2} + \frac{z^2}{c^2} = 1 \quad (2.2.1-7)$$

When an applied field \vec{E}_0 is in arbitrarily direction, the induced dipole moment \bar{p} can

be written as

$$\bar{p} = \varepsilon_m (\alpha_1 E_0^x \hat{x} + \alpha_2 E_0^y \hat{y} + \alpha_3 E_0^z \hat{z}) \quad (2.2.1-8)$$

where E_O^x, E_O^y, E_O^z are the components of \vec{E}_O relative to the principal axes of the ellipsoid. As to the particle polarizability α_i ($i=1,2,3$), they are given by [42]

$$\alpha_i = 4\pi abc \frac{\varepsilon_m - \varepsilon}{3\varepsilon + 3L_i(\varepsilon_m - \varepsilon)} \quad (2.2.1-9)$$

where L_i ($i=1,2,3$) is called geometrical depolarization factor with the relation

$\sum_{i=1}^3 L_i = 1$. The depolarization factors of spherical and spheroidal particles, for instance, are $L_1 = L_2 = L_3 = 1/3$ and $L_1 = L_2$ (for oblate spheroids) or $L_2 = L_3$ (for prolate spheroids), respectively. Similarly to the spherical metal particle with $\varepsilon_m = 1 - \frac{\omega_p^2}{\omega^2}$,

the resonant frequency along an axis i is therefore given by $\omega = \frac{\omega_p}{\sqrt{1 + (\frac{1-L_i}{L_i})\varepsilon}}$.

From the viewpoint of optics, it is much more interesting to note that a metal nanoparticle scatters and absorbs light. The scattered field outside the induced dipole (see Fig. 2.2.1-1) from the metal particle at far field (ie $kr \gg 1$) is given by [36]

$$\vec{E}_S = \frac{k^2}{4\pi\varepsilon} \frac{e^{ikr}}{r} [(\hat{r} \times \vec{p}) \times \hat{r}] \quad (2.2.1-10)$$

where $\vec{p} = \varepsilon\alpha E_o e^{-i\omega t} \hat{z}$ at $z=0$ induced by an incoming field $\vec{E}_{inc} = E_o e^{i(kx - \omega t)} \hat{z}$. If

\vec{p} in (2.1-10) is replaced by $\varepsilon\alpha E_o e^{-i\omega t} \hat{z}$, equation (2.2.1-10) can be rewritten as [42]

$$\vec{E}_S = \frac{e^{ik(r-x)}}{-ikr} \bar{X} E_{inc} \quad (2.2.1-11)$$

where $\bar{X} = \frac{ik^3}{4\pi} \alpha [\hat{r} \times (\hat{r} \times \hat{z})]$. The magnetic field therefore is given by

$$\vec{H}_S = \frac{k}{\mu\omega} (\hat{r} \times \vec{E}_S) \quad (2.2.1-12)$$

The corresponding cross section for scattering C_{sca} (extinction C_{ext}) can be calculated

via the ratio of the total scattering power W_{sca} (total extinction power W_{ext}) to incident power flux density $S_{inc} = \frac{\epsilon\omega}{2k} E_0^2 = \frac{k}{2\mu\omega} E_0^2$. The W_{sca} and W_{ext} are expressed as

$$W_{sca} = \int_0^{2\pi} \int_0^\pi (\bar{S}_{sca} \cdot \hat{r}) r^2 \sin^2 \theta \, d\theta \, d\phi = \frac{\omega k^3 \epsilon}{12\pi} |\alpha|^2 E_0^2 \quad (2.2.1-13)$$

$$W_{ext} = \int_0^{2\pi} \int_0^\pi (\bar{S}_{ext} \cdot \hat{r}) r^2 \sin^2 \theta \, d\theta \, d\phi = \frac{k^3}{2\mu\omega} E_0^2 \text{Im}(\alpha) \quad (2.2.1-14)$$

where $\bar{S}_{sca} = \frac{1}{2} \text{Re}(\bar{E}_S \times \bar{H}_S^*)$ and $\bar{S}_{ext} = \frac{1}{2} \text{Re}(\bar{E}_S \times \bar{H}_{inc}^* + \bar{E}_{inc} \times \bar{H}_S^*)$. With the S_{inc} , we therefore can obtain [43]:

$$C_{sca} = \frac{W_{sca}}{S_{inc}} = \frac{k^4}{6\pi} |\alpha|^2 \quad (2.2.1-15)$$

$$C_{ext} = \frac{W_{ext}}{S_{inc}} = k \text{Im}(\alpha) \quad (2.2.1-16)$$

The extinction cross section C_{ext} presents the sum of the absorption cross section C_{abs} and scattering cross section C_{sca} (ie $C_{ext} = C_{sca} + C_{abs}$). For a small spherical particle with $a \ll \lambda$, the efficiency of extinction (ie C_{ext}), scaling with a^3 , dominates over the scattering efficiency (ie C_{sca}), scaling with a^6 . Consequently, C_{ext} is roughly equal to C_{abs} [38].

In scattering problems, the coordinate axes are usually chosen to be fixed relative to the applied field \bar{E}_{inc} . Let \bar{E}_{inc} be in such a coordinate system $(\hat{x}'_1, \hat{x}'_2, \hat{x}'_3)$. From the optical cross-section theorem [44], the scattering and absorption cross sections for the incident field in \hat{x}'_1 -polarized, \hat{x}'_2 -polarized, and \hat{x}'_3 -polarized directions are:

$$C_{sca}(\hat{x}_i') = \frac{k^4}{6\pi} (|\alpha_1|^2 |\hat{x} \cdot \hat{x}_i'|^2 + |\alpha_2|^2 |\hat{y} \cdot \hat{x}_i'|^2 + |\alpha_3|^2 |\hat{z} \cdot \hat{x}_i'|^2) \quad (2.2.1-17)$$

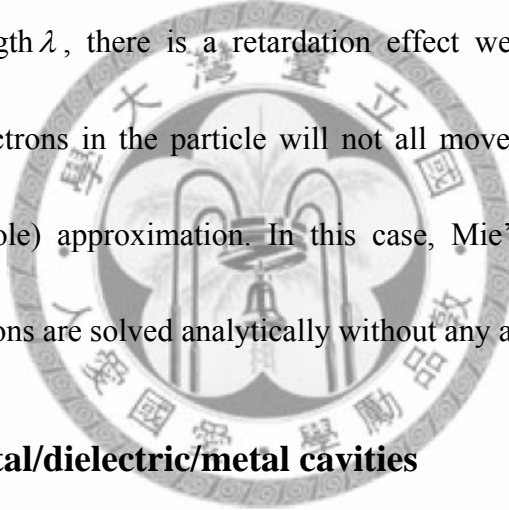
$$C_{abs}(\hat{x}_i') = k \text{Im}(\alpha_1 |\hat{x} \cdot \hat{x}_i'|^2 + \alpha_2 |\hat{y} \cdot \hat{x}_i'|^2 + \alpha_3 |\hat{z} \cdot \hat{x}_i'|^2) \quad (2.2.1-18)$$

In most experiments and observations, the quantities of interest are the average cross sections $\langle C_{sca}(\hat{x}_i') \rangle$ and $\langle C_{abs}(\hat{x}_i') \rangle$, which are given by [42]

$$C_{sca}(\hat{x}_i') = \frac{k^4}{6\pi} (|\alpha_1|^2 \frac{1}{3} + |\alpha_2|^2 \frac{1}{3} + |\alpha_3|^2 \frac{1}{3}) \quad (2.2.1-19)$$

$$C_{abs}(\hat{x}_i') = k \text{Im}(\alpha_1 \frac{1}{3} + \alpha_2 \frac{1}{3} + \alpha_3 \frac{1}{3}) \quad (2.2.1-20)$$

It is interesting to note that when the size of a particle becomes large compared with an incoming wavelength λ , there is a retardation effect we cannot ignore, which means conduction electrons in the particle will not all move in phase, leading to a poor quasi-static (dipole) approximation. In this case, Mie's theory [45] is used, where Maxell's equations are solved analytically without any approximations.



2.2.2 LSPPs at metal/dielectric/metal cavities

We have introduced the SPP metal/dielectric/metal waveguides in chapter 2.1.3. Based on the metal/dielectric/metal configuration, two kinds of boundaries with one open end and the other closed end capped by metal are concerned (see Figure 2.2.2-1). When the SPP in the MDM waveguide is excited, the major part of energy is confined in the dielectric core. With the boundaries, the reflection of the SPPs at both metal/dielectric interfaces can occur. Therefore, the forward and backward SPPs will

form a standing wave also called a Fabry–Pérot resonance (ie $v_g = \frac{d\omega}{dk} = 0$) which is independent of the angle of incidence (ie tilting angle of the dispersion relation $\omega(k)$).

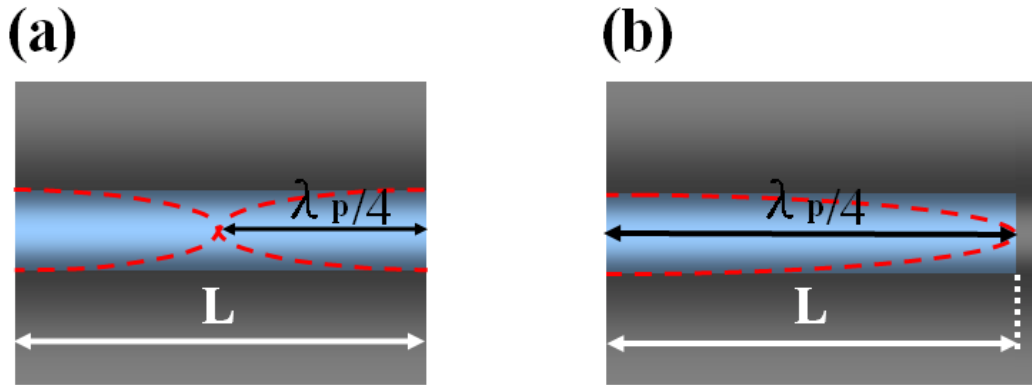


Fig. 2.2.2-1 Lowest-order TM mode of metal/dielectric/metal (a) open and (b) closed cavities with a length of L .

Such resonance conditions in the open and closed cavities are as follows [46]:

$$L = (2m - 1)\lambda_p / 4 \quad (2.2.2-1)$$

$$L = m\lambda_p / 2 \quad (2.2.2-2)$$

where λ_p is the resonant wavelength in a cavity with a length of L . When the waveguide core is decreased, the effective index of the core for the SPP propagation becomes larger, giving a red-shifted resonant wavelength λ_p . The λ_p for both types of cavities is linearly proportional to L . For the m th resonance, the resonant wavelength in the closed-end cavity is $\frac{2m}{(2m - 1)}$ times larger with respect to that in the open-ended resonance cavity. Thus, the resonance energy for the closed-end

cavity is much lower than the energy for the open-ended one. Moreover, one of differences between the both cavities is field intensity enhancement on its core entrance. Light in the closed-end cavity is mostly reflected back from the end metal wall, while light in the open cavity is partially transmitted through the other side entrance. As a result, the closed cavity generally produce higher field enhancement.

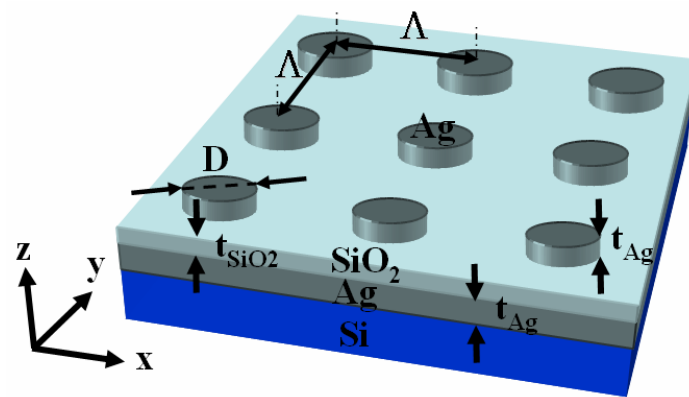
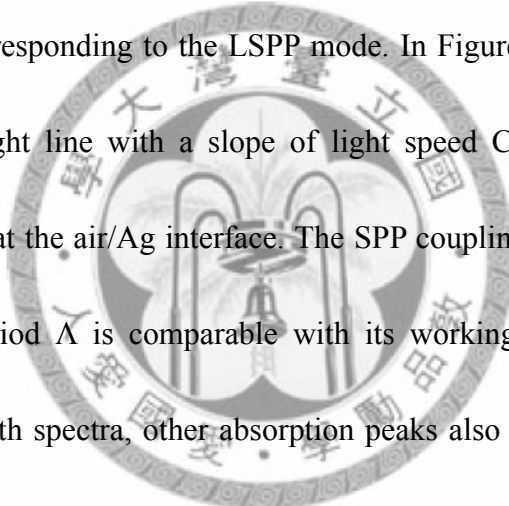


Fig. 2.2.2-2 Schematic diagram of the investigated MD structure.

For two-dimensional metal/dielectric/metal cavities, one of simple open-end cavity structures is a round-shaped metal disk array based on a dielectric/metal substrate. Figure 2.2.2-2 shows illustrates the geometry of the metallic disk (MD) array structure. An array of a Λ periodic MD with diameter D and thickness t_{Ag} is deposited on the top and a silver (Ag) ground plane is on the bottom separated by a thin SiO_2 layer with a thickness t_{SiO_2} . The bottom layer acts as a mirror to reflect incident light and block light transmittance. Similar to the one-dimensional open-end metal/dielectric/metal cavity as shown in Figure 2.2.2-1 (a), a LSPP mode can occur.

Figure 2.2.2-3(a) and 2.2.2-3(b) show the TM- and TE- polarized reflectance spectra of the structure ($D=1\ \mu\text{m}$, $\Lambda=1.5\ \mu\text{m}$, $t_{\text{Ag}}=100\ \text{nm}$, and $t_{\text{SiO}_2}=80\ \text{nm}$) simulated by Rigorous Coupled Wave Analysis (RCWA) algorithm [47-50] with photon energy ranging from 0.12 eV to 0.64 eV, and the angle of incidence θ_i varying from 0° to 90° . The frequency-dependent complex dielectric constants of silver (Ag) and SiO_2 for the RCWA simulation are taken from the reference [51]. As shown in both TM and TE polarized reflectance spectra, a clear angle-independent resonance absorption band occurs at 0.35 eV, corresponding to the LSPP mode. In Figure 2.2.2-3(a), there is an angle dependent straight line with a slope of light speed C , corresponding to the grating-coupled SPPs at the air/Ag interface. The SPP coupling effect becomes much obvious when the period Λ is comparable with its working wavelength. At large incidence angles in both spectra, other absorption peaks also occur due to excitation of horizontal resonance modes. The LSPP mode at 0.35eV is from a strong coupling between the SPP modes of the top MD and bottom silver layers (see Figure 2.2.2-4 (a)). This strong coupling forms a Fabry-Pérot-like resonance in the SiO_2 cavity, as displayed in Figure 2.2.2-4 (b).



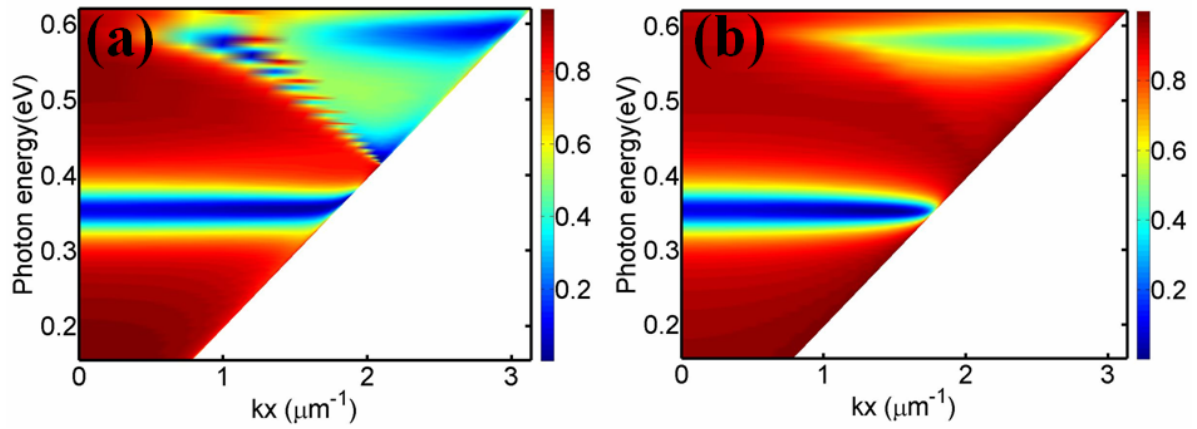


Fig. 2.2.2-3 (a) TM- and (b) TE- mode stimulated reflectance spectra of the MD structure.

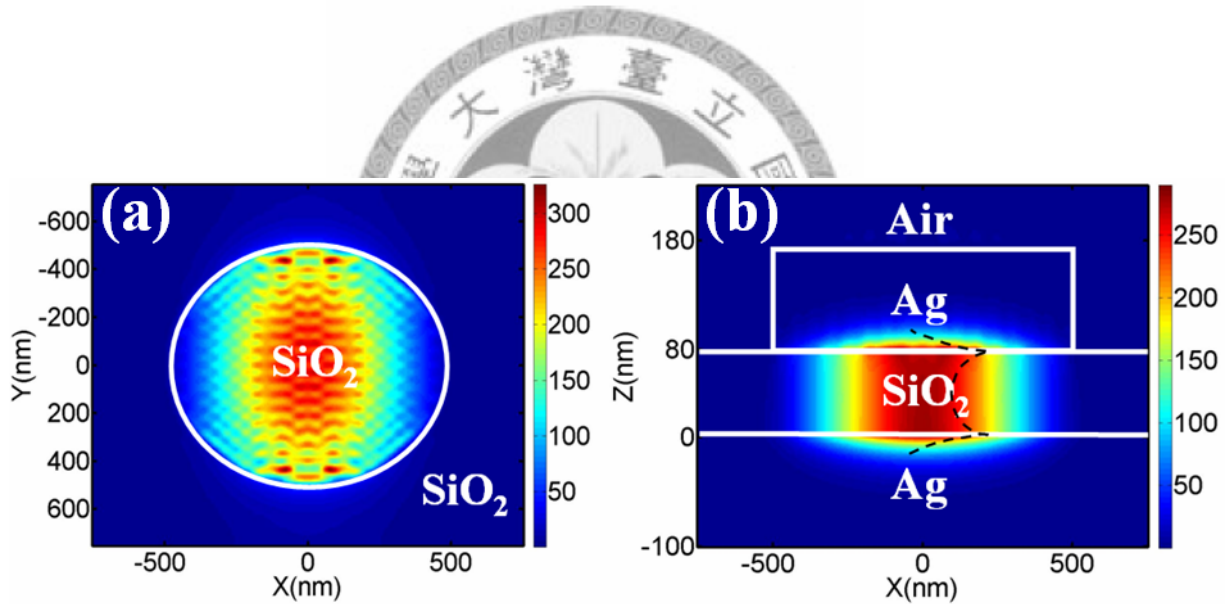
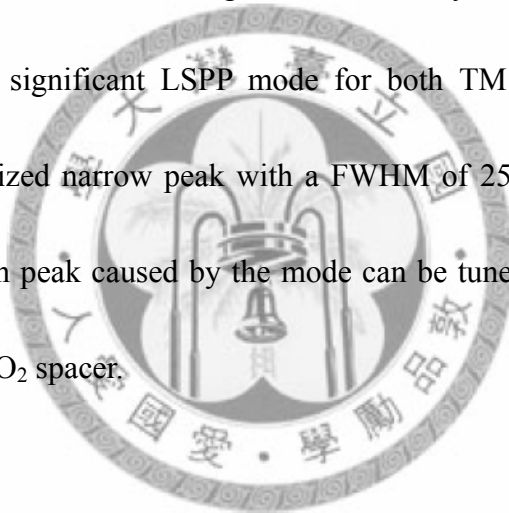


Fig. 2.2.2-4 TM-polarized $|H_y|^2$ distributions in one pitch of the MD array at 0.35 eV for normal incidence in (a) X-Y plane at $Z=40$ nm and (b) X-Z plane at $Y=0$ nm.

3. Angle and polarization independent narrow-band thermal emitter made of metallic disk on SiO₂

Based on the Kirchhoff's law of thermal radiation [52], good light absorbers are good light emitters when they are heated. We demonstrated an efficient narrow-band thermal emitter as an active plasmonic device. The device is made of the metallic disk (MD) structure as mentioned in the section 2.2.2. The absorption and emittance spectra of such structure were investigated theoretically and experimentally. The structure exhibits one significant LSPP mode for both TM and TE polarizations, leading to an un-polarized narrow peak with a FWHM of 250nm and low sideband emission. The emission peak caused by the mode can be tuned by either varying the disk diameter or the SiO₂ spacer.



3.1 Device description

The MD array structure as shown in Figure 2.2.2-2 is based on a silicon substrate. An array of Λ periodic silver disks with diameter D and thickness 100nm is deposited on top of a uniform SiO_2 layer with thickness $t=50\text{nm}$. Below the SiO_2 layer is a 100nm metallic silver thin film to block the light transmittance. The fabrication of the structure began with e-gun deposition of a 5nm Cr adhesion layer and a 100 nm silver layer on the top of a silicon (Si) substrate, followed by a thickness of SiO_2 thin film deposited by plasma-enhanced chemical vapor deposition (E-gun deposition and PECVD recipes shown in Appendix C). A photoresist layer was then spin-coated on the top of the SiO_2 thin-film layer. An array of the round-shaped disks periodically spaced with a lattice constant Λ in x and y directions was defined on the resist by using photolithography. After developing the resist, a 100-nm-thick silver layer was deposited. Then, a lift-off process was carried out by rinsing the sample in acetone for a few minutes and cleaning it with isopropyl alcohol and de-ionized water, respectively. Finally, the completed structure was dried with nitrogen gas. The size of the array sample was $1\text{cm}\times 1\text{cm}$. To heat up the sample, a DC current was applied through the molybdenum (Mo) thin film deposited on the backside of the silicon wafer. Due to no transmission for the case, the thermal emittance spectrum of the sample can be predicted by the equation

$$Emission(\lambda, T) = B(\lambda, T) \left(\int (1 - R(\lambda, \theta, \phi)) \cos(\theta) d\Omega \right)$$

where the reflectance $R(\lambda, \theta, \phi)$ can be estimated by the Rigorous Coupled Wave Analysis (RCWA) method [47-50]. Through the equation, the thermal emittance peaks are mainly dominated by the reflectance spectrum. In the simulation part of the structure, we collaborated with Mr. Mohammed Nadhim Abbas (a PhD student of the Director Yia-Chung Chang in the RCAS at Academia Sinica). We found that both TM- and TE- polarized reflectance spectra show one clear resonant dip at 0.33eV for full incident angles, as shown similarly in Fig. 2.2.2-3(a) and 2.2.2-3(b). The angle and polarization independent peak feature will give an un-polarized thermal emission peak. The wavelength of the emission peak also can be tuned by varying either disk diameter or SiO₂ layer thickness. Figure 3.1-1 shows the absorption spectra $1 - R(\lambda, \theta, \phi)$ for various disk diameters when $t=50\text{nm}$. The reduction of the disk diameter results in a blue shift in the resonance wavelength. On the other hand, when thickness of SiO₂ layer (spacer) increases, the coupling of top and bottom interface decreases, resulting in a blue shift.

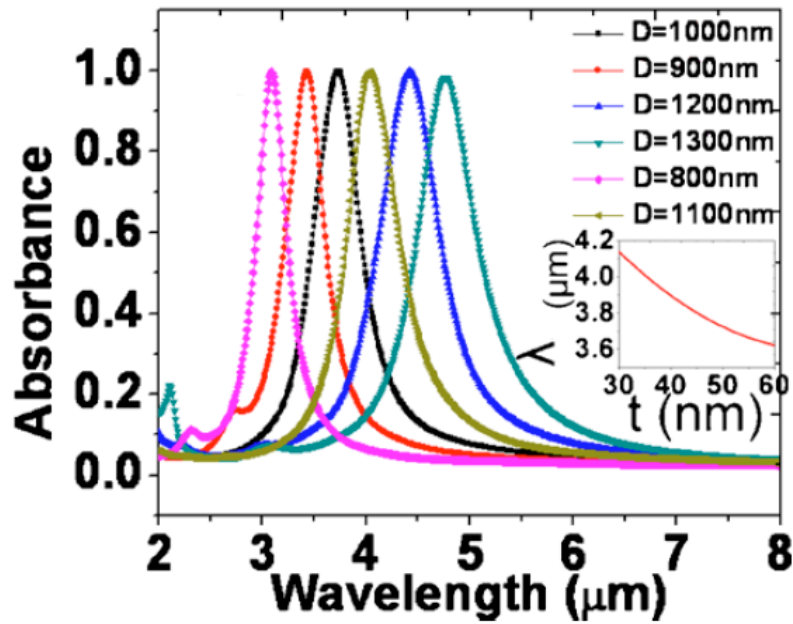


Fig. 3.1-1 Absorption spectra ($1-R(\lambda)$) of the MD array structure with different diameters D for $\theta=0^\circ$ when $t=50\text{nm}$. The inset shows resonance wavelength (λ) versus the SiO_2 layer thickness (t) when $D=1000\text{nm}$.

3.2 Experimental setup and results

To characterize the thermal emission peak, we corroborated with professor Si-Chen Lee's group. A Perkin Elmer 2000 Fourier transform infrared spectrometer system was adopted to measure the thermal radiation spectra. A 1cm^2 sample with $D=1.15\mu\text{m}$ and $\Lambda=3\mu\text{m}$ was fixed across the electrodes in a chamber with a pressure of 3 mTorr (see Figure 3.2-1(a) and 3.2-1(b)). A Dc current was then applied through the Mo film to heat up the sample. The thermal radiation of the sample was collected by a 45° off-axis mirror with a NA of 0.1 and then reflected into the FTIR system

input port. An external wire-grid polarizer was set up between the sample and the FTIR system for the polarized thermal radiation measurement.

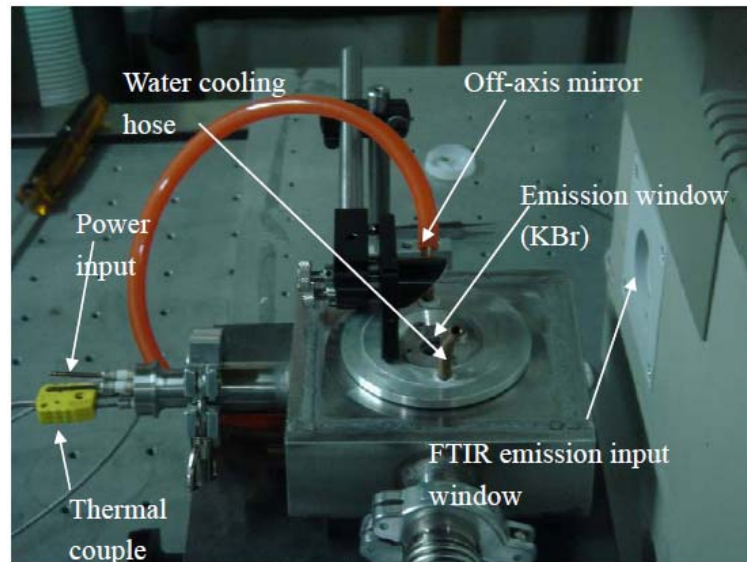


Fig. 3.2-1(a) Side view of thermal emitter chamber [53].

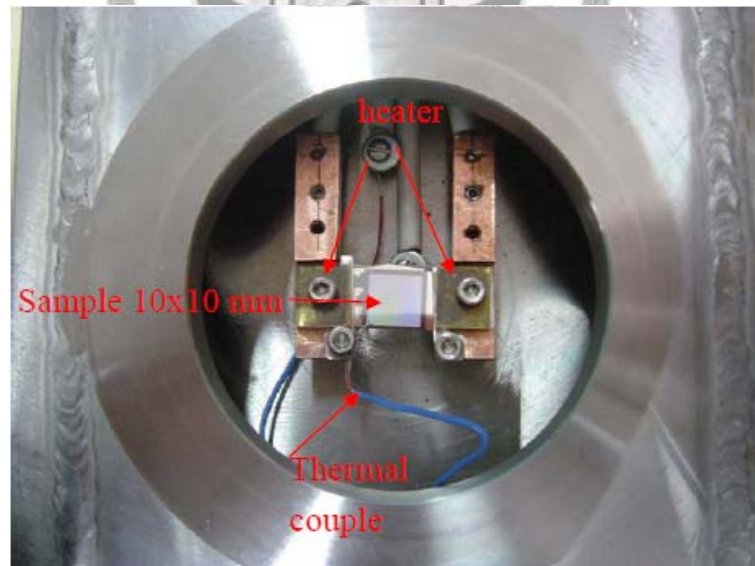


Fig. 3.2-1(b) Top view of thermal emitter chamber [53].

Figure 3.2-2(a) shows the dispersion relation of reflectance spectra of the sample, the gray scale from dark to bright represents the reflectance from low to high. The

measurement was done by varying the incident angle from 12° to 65° . The dip at 0.29eV ($4.27\ \mu\text{m}$) corresponding to the LSPP mode of the metallic disk. Figure 3.2-2(b) shows the measured thermal emission spectrum of the IR emitter when the sample was heated up to 220°C (blue line) and 300°C (black line), respectively. The emission peak was observed at $4.27\ \mu\text{m}$ with a full-width at half-maximum (FWHM) of $0.25\ \mu\text{m}$. By performing both emittance and reflectance spectra measurements, we found that the emission and resonant peak wavelengths agree well as predicted by the Kirchhoff's law of thermal radiation. Because of the TE- (s-) and TM-polarized (p-) spectra are almost identical (see Figure 3.2-2(c)), we can clearly confirm that the thermal radiation peak is un-polarized.

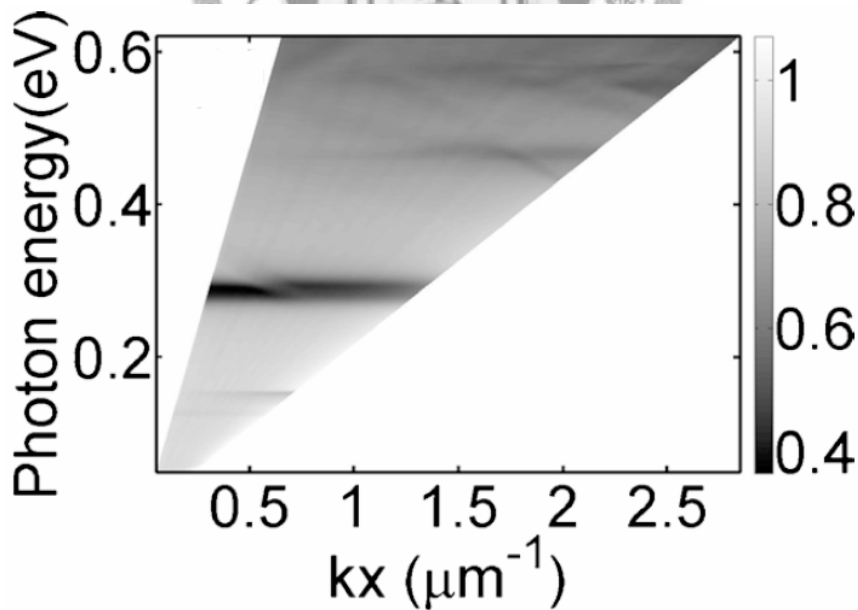


Fig. 3.2-2(a) Measured reflectance spectra of sample with $D=1.15\ \mu\text{m}$ and $\Lambda=3\ \mu\text{m}$.

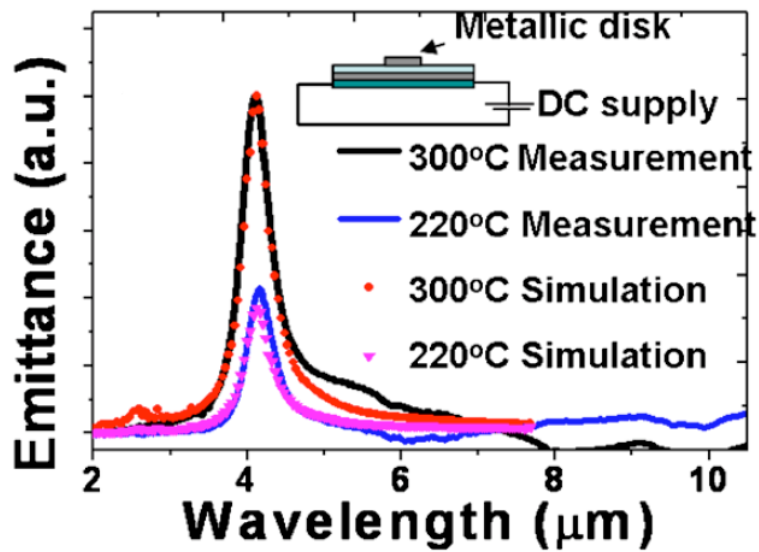


Fig. 3.2-2(b) Simulated and measured emission spectrum of the IR emitter at 220 °C (blue line) and 300 °C (black line), respectively.

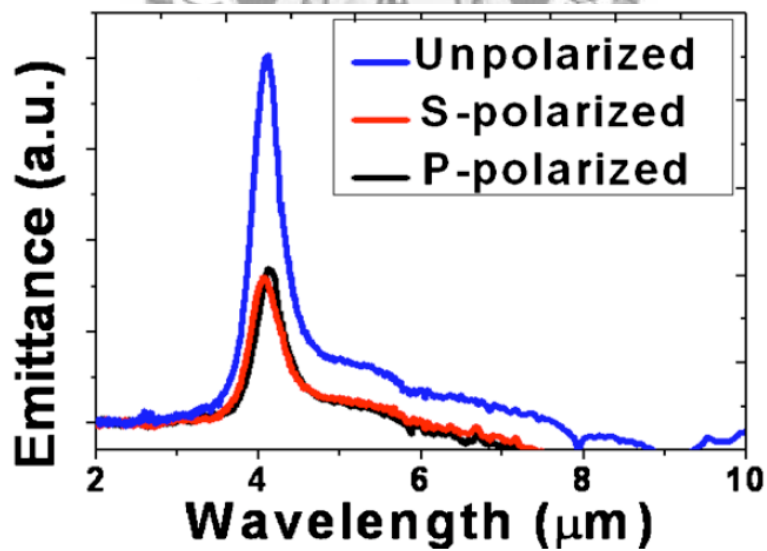


Fig. 3.2-2(c) The measured emission spectrum for unpolarized, s-polarized (TE-polarized) and p-polarized (TM-polarized) for 220 °C.

3.3 Summary

The plasmon-polariton band structures of metallic disk structure for both TM and TE polarizations have been investigated. We show that a narrow band thermal emitter at IR region can reach an emission peak at $4.27\mu\text{m}$ with a FWHM of $0.25\mu\text{m}$. The peak can be tuned by either changing the disk diameter or SiO_2 thickness. This kind of emission spectrum with narrow bandwidth, low sideband and high intensity is very useful for the application in IR light sources.



Chapter 4 Wide-angle plasmonic infrared filters/absorbers

One-dimensional plasmonic filter/absorber assisted by LSPPs in a symmetric Ag/SiO₂/Ag T-shaped array was theoretically and experimentally investigated. An angle-independent LSPP resonant mode caused by a Fabry-Pérot resonance in the structure was observed in agreement with our RCWA simulation. The resonant wavelength of the mode can also be controlled by modifying the geometry of the T-shaped structure. The LSPP angle-independent feature makes the designed filter more flexible than a guided-mode resonance (GMR) dielectric filter [54-56] and a surface plasmon-polariton (SPP) filter [57] as well as a plasmonic multilayer filter related to our previous work [58]. To further improve the absorption performance and reduce the fabrication difficulty, a two-dimensional round-shaped metal disk array is applied. Different from the previous work [59, 60], the our results clearly revealed that the resonant wavelength of a LSPP angle-independent band is independent of the disk periodicity. Therefore, a broadband thermal emitter made of six distinct disks in one unit cell can be realized. We also first experimentally found that the absorptivity of the disk absorber obeying the Beer Lambert law can be enhanced by increasing the ratio of disk size to the unit cell area. By modifying the area filling ratio, we demonstrated a high-performance, wide-angle, polarization-independent dual band

absorber with two maximal absorptivity peaks greater than 84% over a wide range of incident angles.

4.1 Design and simulation of the Ag/SiO₂/Ag T-shaped array

Figure 4.1-1(a) shows the illustration of the proposed Ag/SiO₂/Ag T-shaped array with geometric parameters as follows: $\Lambda_g=3000\text{nm}$, $t_{\text{Ag}}=100\text{nm}$, $t_w=50\text{nm}$, $W_T=800\text{nm}$, and $W_{\text{Ag}}=1100\sim 2000\text{nm}$. Figure 4.1-1(b) is a schematic sketch of the T-shaped structure as a notch filter when light is reflected back toward a signal detector. In the simulation, the incident light is TM-polarized (i.e. magnetic field parallel to the y-axis) with different incident angles in the x-z plane. The frequency-dependent complex dielectric constants of silver (Ag) and SiO₂ are taken from Ref. [61].

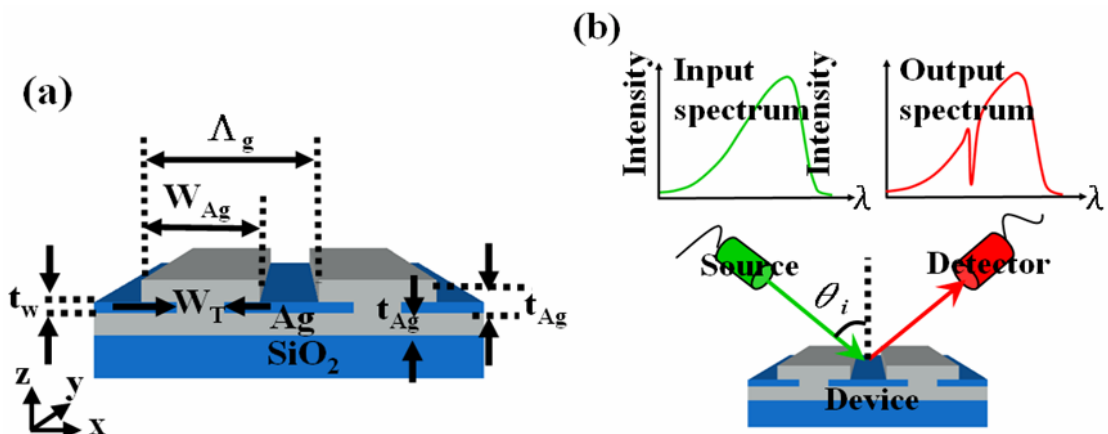


Fig. 4.1-1(a) Illustration of the T-shaped array structure. (b) Illustration of the reflection-type filter with the designed structure

To find the resonant energy and understand the behavior of the resonant mode in the designed T-shaped array, reflectance spectra are calculated. Figure 4.1-2(a) shows the calculated reflectance spectra for $W_{Ag} = 1500\text{nm}$ and photon energy ranging from 0.12eV to 0.62 eV, while the angle of incidence varies from 0° to 90° . An angle-independent flat band is found at the photon energy of 0.35eV. This flat band indicates the group velocity ($\partial \omega / \partial K_x$) in the x-direction is zero and the mode at the band is highly-localized at the metal-dielectric interface, which is called a LSPP mode. The reflectance spectra with various incident angles in the y-z plane are also examined as shown on Figure 4.1-2(b). The dispersion curve in K_y is parabolic. Therefore, a small deviation of K_y from zero will not lead to significant change in resonance energy. The angle-independent mode is due to a strong coupling between the SPP modes of the cap silver layer and bottom layer. This strong coupling will form the Fabry-Pérot type resonance in the closed-end Ag/SiO₂/Ag cavities under the cap [62]. The resonance not only can be excited at any incident angle, giving a strong angular tolerance of the structure compared with the GMR and SPP filters [54-57], but also can offer a single flat band in IR region, which is better for single-band rejection applications compared with the 1D plasmonic multilayer filter [58]. Figure 4.1-2(c) shows the $|H_y|^2$ distribution of the LSPP mode in one unit cell of the periodic structure when the photon energy is tuned to 0.35eV (ie resonant wavelength 3.54 μm)

with normal incidence. The $|H_y|^2$ field has nodes at the open ends ($x = \pm 750\text{nm}$) and anti-nodes at the closed ends ($x = \pm 400\text{nm}$), showing the spatial response of the first Fabry-Pérot resonance mode. When the SiO_2 layer increases, the coupling will be weaker and the LSPP band becomes broad, blur, and blue-shift. For a thicker SiO_2 spacer, the effective index of the mode in the resonant cavities will be decreased [63, 64]. Therefore, the resonant wavelength of the band is blue-shifted. One of the advantages of this T-shaped array is that the LSPP resonance wavelength has a strong dependence on the geometrical parameter W_{Ag} due to its Fabry-Pérot type resonance. It can be found that the resonance wavelength increases linearly as W_{Ag} varies from 1100nm to 2000nm. The wavelength tuning rate is approximately 3.8 nm per nm in W_{Ag} .

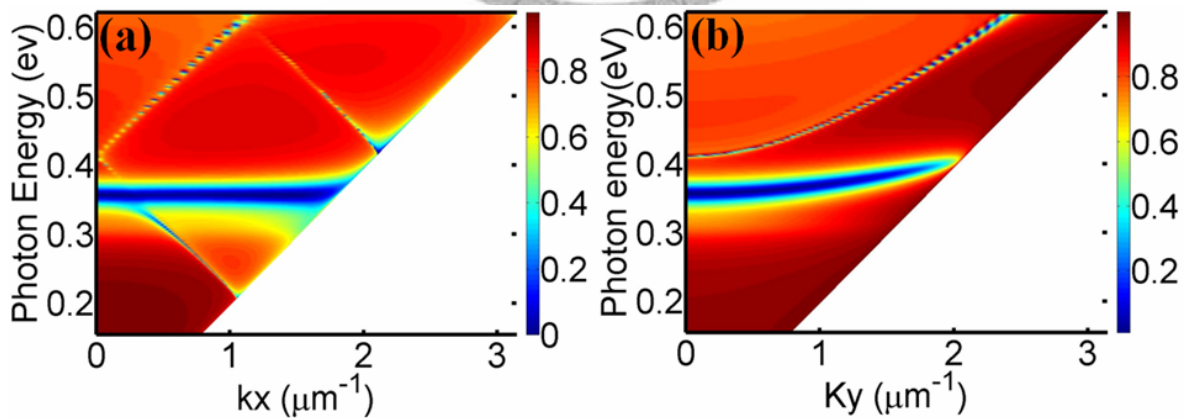
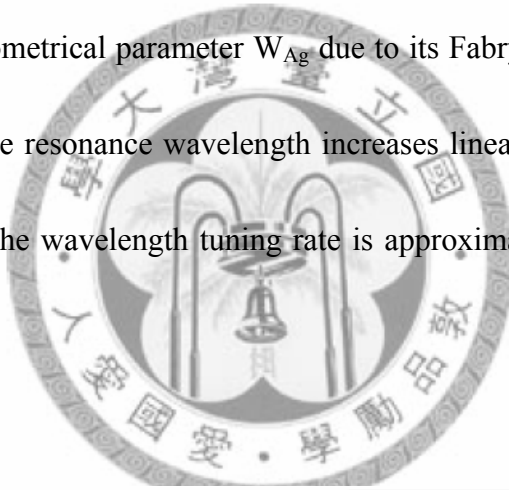


Fig. 4.1-2(a) Stimulated reflectance spectra in x-z plane. (b) Stimulated reflectance spectra in y-z plane

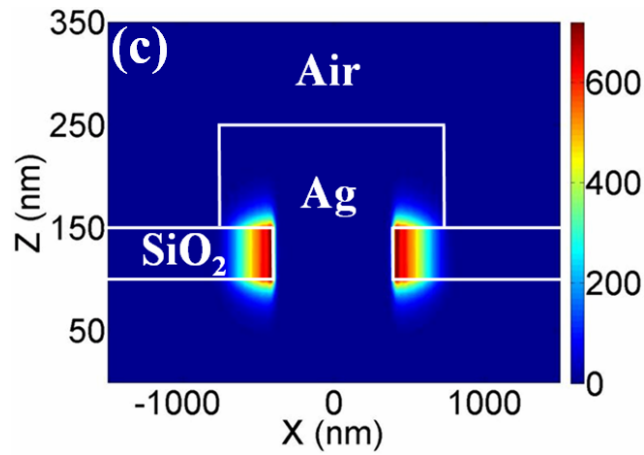


Fig. 4.1-2(c) $|H_y|^2$ distribution at 0.35eV in x-z plane.

4.2 Fabrication of the Ag/SiO₂/Ag T-shaped array

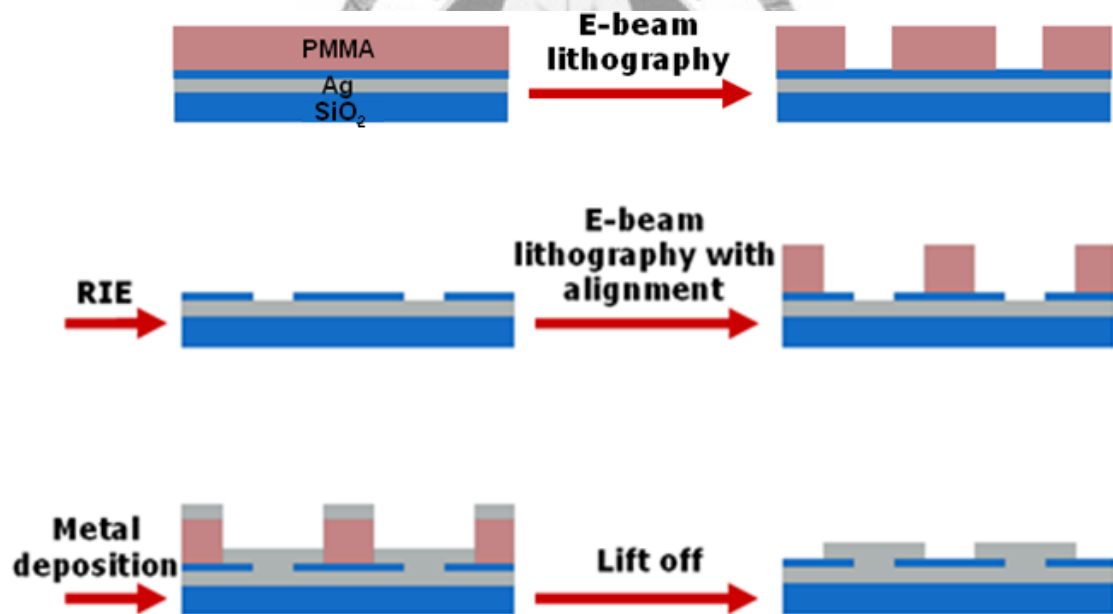


Fig. 4.2-1 Fabrication process of the T-shaped array.

The Ag/SiO₂/Ag T-shaped structure was fabricated on a silica substrate. A 100 nm Ag film and a 50nm SiO₂ film were deposited on the substrate by using E-gun

evaporator and RF sputtering system (E-gun deposition and RF sputtering recipes shown in Appendix C). A PMMA layer was coated on the SiO₂ layer, as shown in Figure 4.2-1. A grating structure with a lattice constant (Λ_g) of 3 μm and a line spacing of 800nm (W_T) was defined on the PMMA layer by electron beam lithography. The pattern was transferred to SiO₂ layer by reactive ion etching (RIE recipe in Appendix C). The second EB lithography was executed to make another PMMA periodic structure on top of the SiO₂ layer with a line width W_{Ag} . Finally, a 100nm Ag layer was deposited, and the T-shaped structure was obtained by lifting PMMA layer off. The size of the structure is 400 μm \times 400 μm , which is large enough to obtain clear signals from the structure. Figure 4.2-2(a) is the image of T-shaped array with a tilt angle of 45°. Figure 4.2-2(b) is the cross-sectional image of the structure.

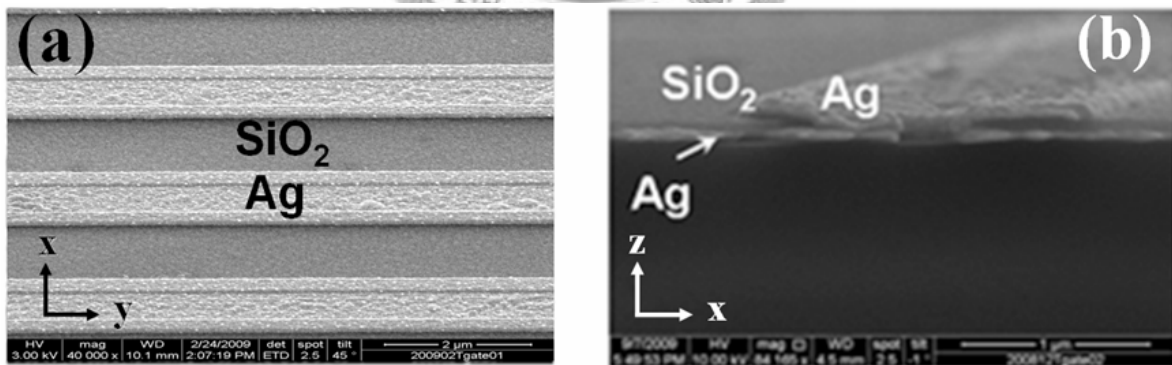


Fig. 4.2-2(a) 45° angle SEM image of the T-shaped array. (b) Cross-sectional SEM image of the T-shaped structure.

4.3 FTIR measurement setup

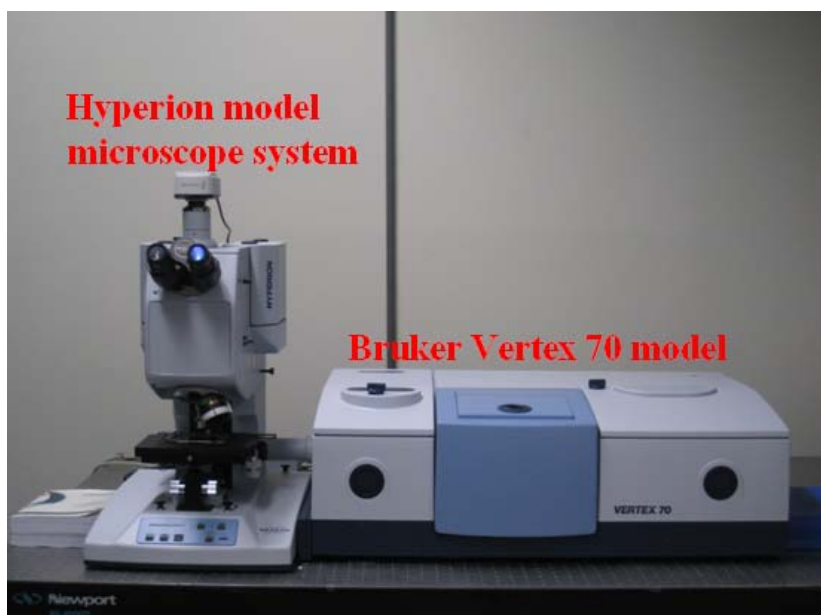


Fig. 4.3-1 Experimental setup for measurements.

A Bruker Vertex 70 model Fourier-transform-infrared (FTIR) spectrometer coupled to a Hyperion model microscope system was applied for sample measurements (see Figure 4.3-1). The Hyperion unit includes transmission and reflection modules. In the experiment, a MIR reflection module was used. In this module, a MIR un-polarized light source was focused a sample and reflected back with a 15X objective lens ($NA=0.4$ and focus length $f=24\text{mm}$). The back-reflected light through a controllable $50\mu\text{m}\times 50\mu\text{m}$ slit was collected and detected using a MCT (mercury-cadmium-telluride) photodetector with a spectral resolution of 2 cm^{-1} . Because of the slit size $50\mu\text{m}\times 50\mu\text{m}$ back of the objective lens, the maximum reflected light acceptable angle can be reduced from 23.5° to 0.05° , giving a narrow

range of angles of incidence. Based on the setup, the measured reflectance or absorbance spectra varying with incident angles from 0° to 15° can be observed by using a tilt-angle wedge on which a sample is placed.

4.4 Experimental results of the Ag/SiO₂/Ag T-shaped array

To characterize the optical filtering property of the Ag/SiO₂/Ag T-shaped array, the reflectance and absorbance spectra (see Figure 4.4-1(a)) of the T-shaped structure at normal incidence were measured. A resonance peak (dip) in the absorbance (reflectance) spectrum is at $3.34\mu\text{m}$ with a FWHM of $0.29\mu\text{m}$, where this bandwidth is much narrower than that of the plasmonic multilayer structure $0.5\mu\text{m}$ [58]. To increase the contrast of the dip, a TM polarized light can be applied. The location of the resonance peak (or stop-band center wavelength) can also be controlled by varying the top width W_{Ag} or the neck width W_{T} . Figure 4.4-1(b) shows the absorbance spectra at normal incidence for $W_{\text{Ag}} = 1300\text{nm}$, 1540nm and 1910nm and $W_{\text{T}} = 800\text{nm}$. It is seen that the resonance peaks occur at $2.80\mu\text{m}$, $3.48\mu\text{m}$ and $5.08\mu\text{m}$, respectively, while CO₂ and water vapor absorptions in the atmosphere are also visible. Figure 4.4-1(c) shows the measurement and simulation results of the resonant wavelengths as functions of W_{Ag} . The resonance wavelength of the peak is red-shifted linearly as W_{Ag} increases with an error smaller than 5%. These resonance peaks

correspond to the LSPP flat bands. This strong dependence in W_{Ag} verifies the LSPP mode in the plasmonic filter, and excludes SPP modes propagating around the Ag/air grating area.

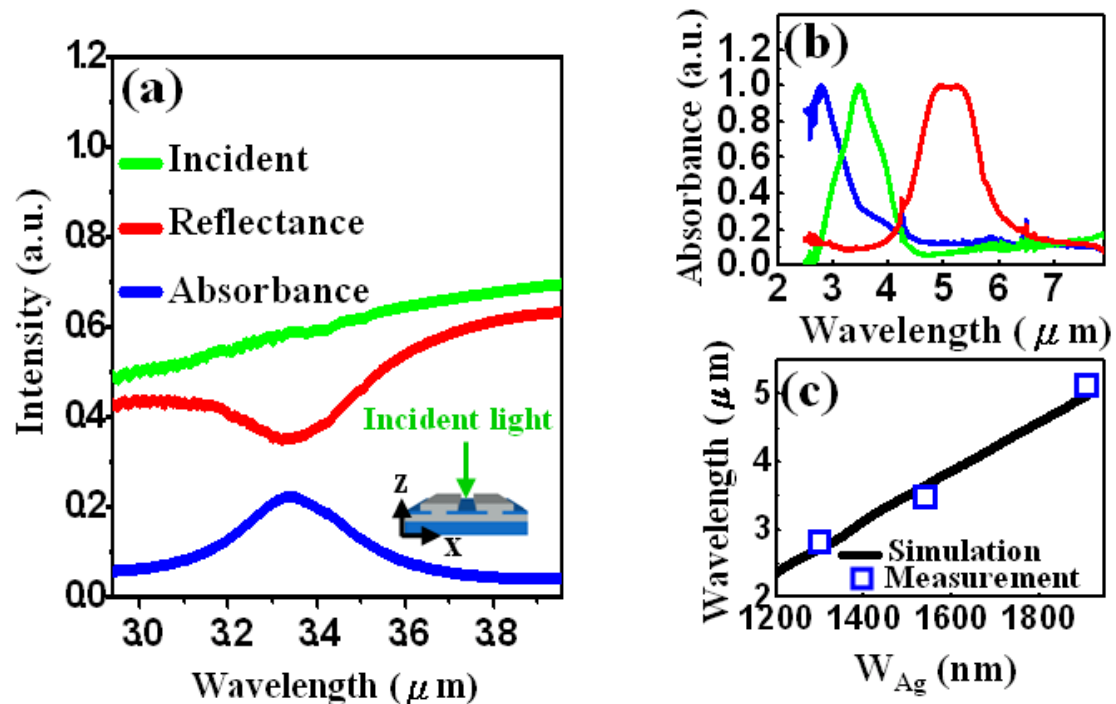


Fig. 4.4-1 (a) Incident (green), reflectance (red), and absorbance (blue) spectra at normal incidence. (b) Normal incident absorbance spectra from the T-shaped arrays with the widths $W_{Ag} = 300$ nm, 1540 nm, and 1910 nm. (c) Comparison of calculated and measured wavelengths of resonance.

To confirm the angle-independent property of the LSPP band, the absorbance spectra with different incident angles in the x-z plane were measured. Figure 4.4-2 shows the measured spectra of the T-shaped array with the incident angles of 0° , 5° , 10° and 15° . The resonance peaks of four spectra all appear at the same wavelength of

3.54 μm . These results verified the omni-directional absorption of the LSPP band at 0.35eV, in agreement with our simulation. These unique optical properties of the T-shaped array suggest that it can be applied as an angle-independent plasmonic filter capable of operating in a broad range of IR spectrum.

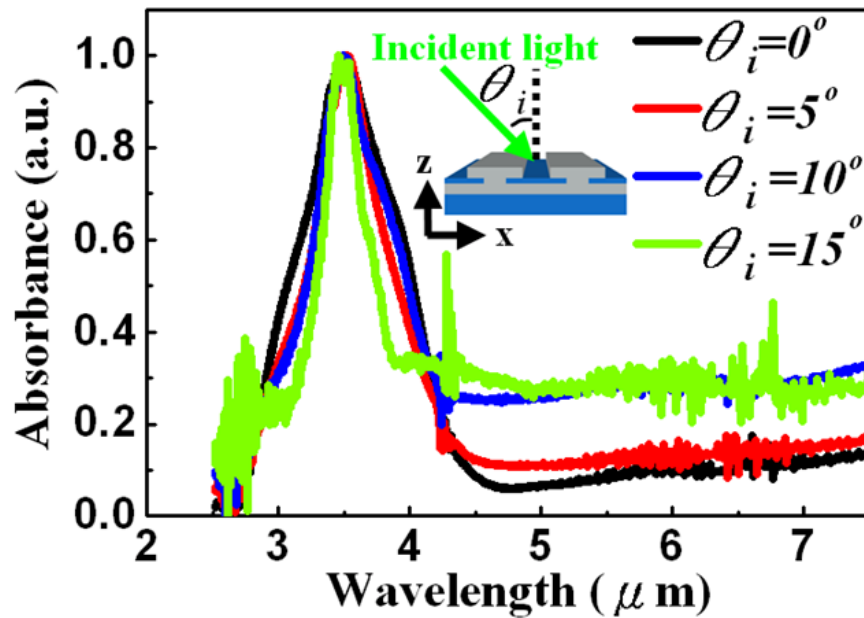


Fig. 4.4-2 Absorbance spectra from the T-shaped array with incident angles in x-z plane from 0° to 15° . The accuracy of the measured spectra is 3 nm.

4.5 Design and simulation of two-dimensional (2D) metal disk array absorbers

To further improve the absorption performance of the one-dimensional T-shaped array as shown in Figure 4.4-1(a), two-dimensional metallic disk (MD) arrays based on a SiO₂/Ag/Si substrate are proposed (see Figure 2.2.2-2). In this study, a round-shaped metal disk absorber is applied because it can provide an angle and polarization independent LSPR band over a broad range of incidence angles up to nearly 90° [31, 59]. The TM- and TE- polarized reflectance spectra of the MD structure ($\Lambda=1.5\ \mu\text{m}$, $D=1\ \mu\text{m}$, $t_{\text{Ag}}=100\ \text{nm}$, and $t_{\text{SiO}_2}=80\ \text{nm}$) have been simulated and shown in Figure 2.2.2-3(a) and 2.2.2-3(b). As can be seen in both TM and TE polarized reflectance spectra, a clear angle-independent resonance absorption band occurs at 0.35 eV, corresponding to a LSPR mode. According to the calculated LSPR mode profiles (see Figure 2.2.2-4(a) and 2.2.2-4(b)), 82% of $|H_y|^2$ is localized in the SiO₂ layer, and only 16% of $|H_y|^2$ is distributed within the metal region. Because of the $|H_y|^2$ distributions mostly localized within the SiO₂ cavity and less coupling between neighbor MDs, the resonant wavelength is independent of its periodicity; however, it is sensitive to individual MD size and the effective index of the medium in the cavity. When the SiO₂ spacer is decreased, the resonant light is much attracted

into the cavity and is red-shifted because of increasing the effective index of the mode in the resonant cavity.

Due to the resonance immune to the MD period, it is promisingly feasible for the applications in broadband emitters and absorbers consisting of different sublattices with different MD resonators corresponding to different absorption bands. According to the Kirchhoff's law of thermal radiation, at equilibrium the emittance normalized by the blackbody emittance should be equal to absorptivity. The equality has been demonstrated and reported [65]. If there is no transmission, the thermal emittance spectrum can be predicted by the product of the blackbody radiation profile and the absorptivity integrated over solid angles

$$Emission(\lambda, T) = B(\lambda, T) \left(\int (1 - R(\lambda, \theta, \phi)) \cos(\theta) d\Omega \right)$$

where $B(\lambda, T)$ denotes the thermal radiation spectrum of a perfect blackbody (with a unit of W/m^2) at temperature T and $1 - R(\lambda, \theta, \phi)$ is the absorptivity of the designed sample. Through the equation, the thermal emittance peaks of the sample can therefore be enhanced by the increased absorptivity at given resonant wavelengths and temperature. The absorptivity or absorbance is particularly governed by an absorbing species of cross-sectional area and species concentration, which is the well-known Beer Lambert law [66]. By tailoring the absorption cross section and concentration, one can improve the absorber absorptivity or emissivity.

4.6 Fabrication of the 2D metal disk array absorbers

The MD array was fabricated on a Cr(5nm)/Si substrate. A 100 nm Ag film and a 50nm SiO₂ film were deposited on the substrate by an electron gun evaporator and PECVD system (E-gun and PECVD recipes shown in Appendix C). A 350nm PMMA layer was coated on the SiO₂ layer. A disk array with a diameter of D and lattice constants of Λ in x and y directions was first defined on the PMMA layer by electron beam lithography. The pattern was then developed and a 100nm silver layer was deposited on the top surface. Finally, the MD disk array was obtained by lifting the PMMA layer off. The size of the structure is approximately 220 $\mu\text{m} \times 220 \mu\text{m}$, which is large enough to obtain obvious signals from the structure during the measurement. Figure 4.6-1 is the SEM image of a fabricated sample where the inset displays one unit cell of the MD structure with a tilt angle of 35°.

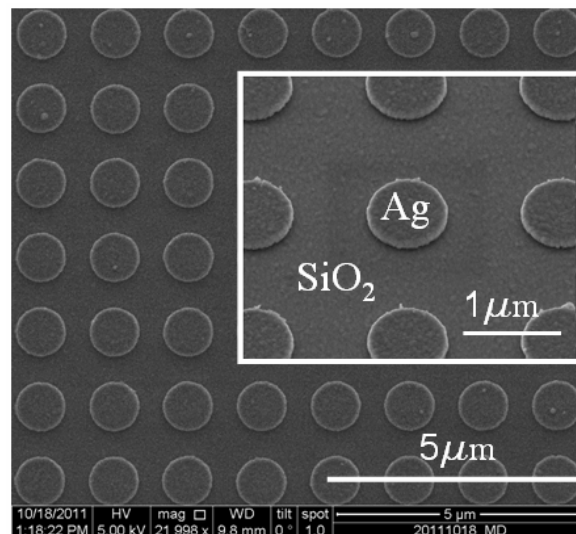
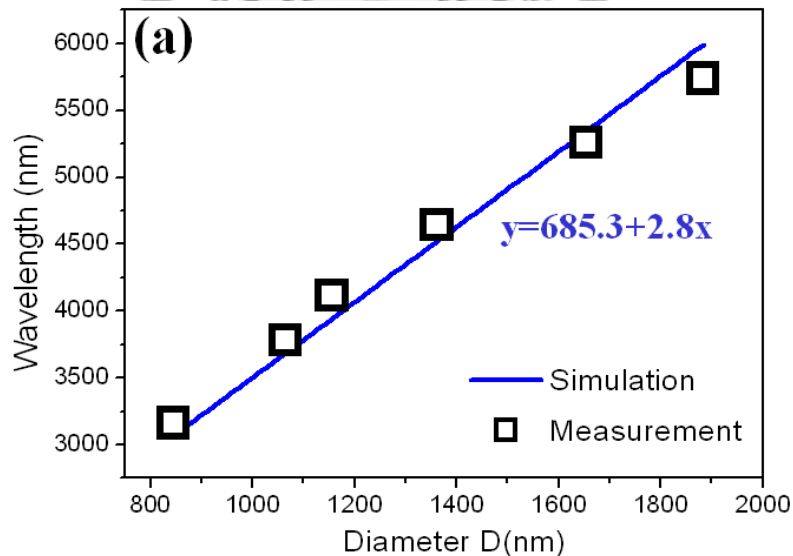


Fig. 4.6-1 SEM image of a fabricated MD structure.

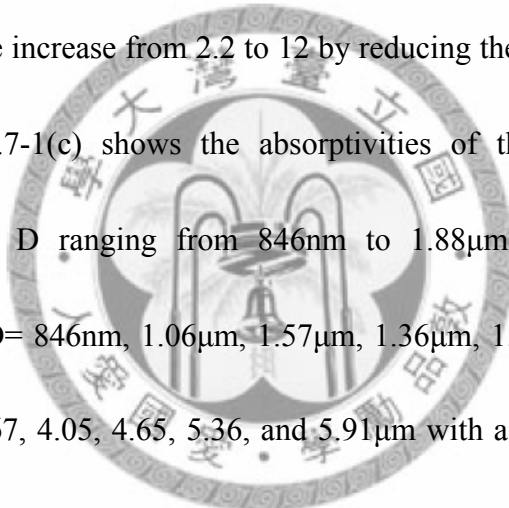
4.7 Experimental results of the 2D metal disk arrays

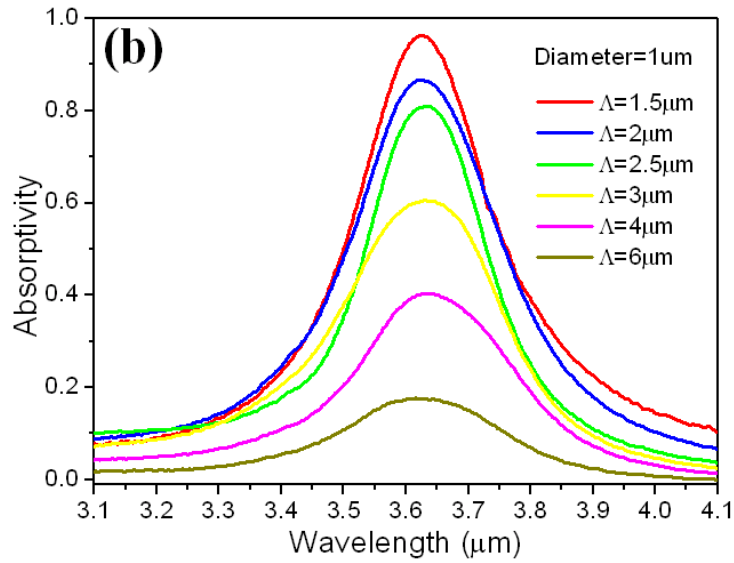
To characterize the resonant mode and absorptivity $A(\lambda) = 1 - R(\lambda)$ of the structure, the reflectivities $R(\lambda)$ at normal incidence normalized with respect to a bare Ag/Si substrate were measured by using a FTIR spectrometer with a MIR unpolarized source and a resolution of 2 cm^{-1} . Figure 4.7-1(a) shows the measured resonant wavelengths of the SiO_2 cavities with varying disk size when $t_{\text{SiO}_2} = 80 \text{ nm}$. The resonant wavelength (black open square) is linearly proportional to the MD size, in accordance with our simulation (blue solid line). The wavelength tuning rate is approximately 2.8 nm per nm in D.



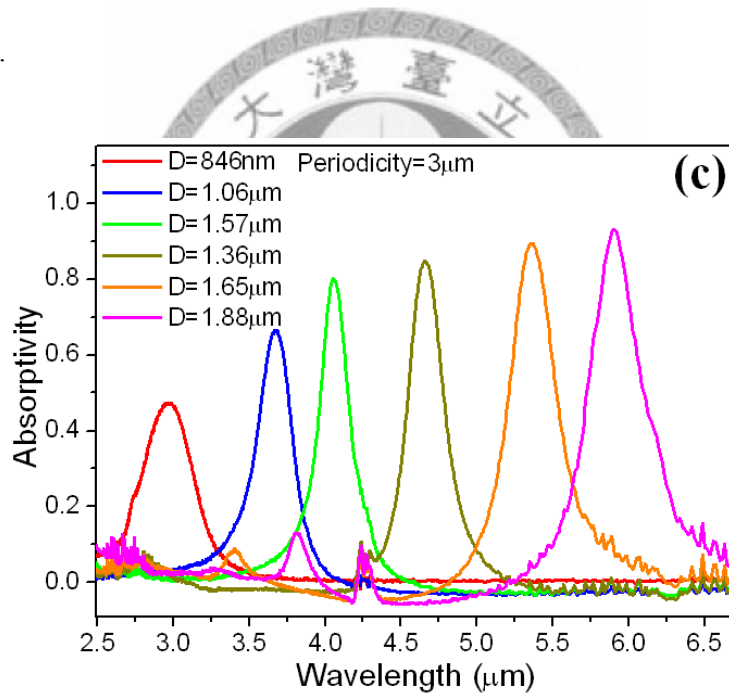
4.7-1(a) Comparison of the calculated and measured wavelengths of resonances as functions of the disk diameter D.

The absorptivities of the MD arrays varying in density and size were also examined. Figure 4.7-1(b) displays the absorptivities of the 1 μm MD absorbers with $\Lambda = 1.5, 2, 2.5, 3, 4,$ and $6\mu\text{m}$. All the absorption peaks are observed at $3.63\mu\text{m}$ with approximately the same FWHM $0.28\mu\text{m}$. The peak absorptivity is increased from 17% to 94% as we diminish the periodicity of the MD array (ie an increase in the MD density). The figure of merit (FOM) of the absorber defined as $\text{FOM} = AQ$ [67], where A and $Q = \lambda / \text{FWHM}$ are absorptivity and quality factor. The FOM of the metal disk array can be increase from 2.2 to 12 by reducing the periodicity from $6\mu\text{m}$ to $1.5\mu\text{m}$. Figure 4.7-1(c) shows the absorptivities of the absorbers with the considered disk sizes D ranging from 846nm to $1.88\mu\text{m}$ when $\Lambda = 3\mu\text{m}$. The absorption peaks for $D = 846\text{nm}, 1.06\mu\text{m}, 1.57\mu\text{m}, 1.36\mu\text{m}, 1.65\mu\text{m},$ and $1.88\mu\text{m}$ are found at $\lambda = 2.96, 3.67, 4.05, 4.65, 5.36,$ and $5.91\mu\text{m}$ with a maximum absorptivity of 47%, 66%, 75%, 85%, 90%, and 95% respectively, while other high-order modes for $D = 1.65\mu\text{m}$ and $1.88\mu\text{m}$ at $\lambda = 3.40\mu\text{m}$ and $3.81\mu\text{m}$, CO_2 and water vapor absorption features in the atmosphere are also visible. When we expand the disk size proportional to its absorption cross section, the energy absorbed to form the Fabry–Pérot-like resonance in the MD resonator per unit area will increase, resulting a pronounced increase in the absorptivity.





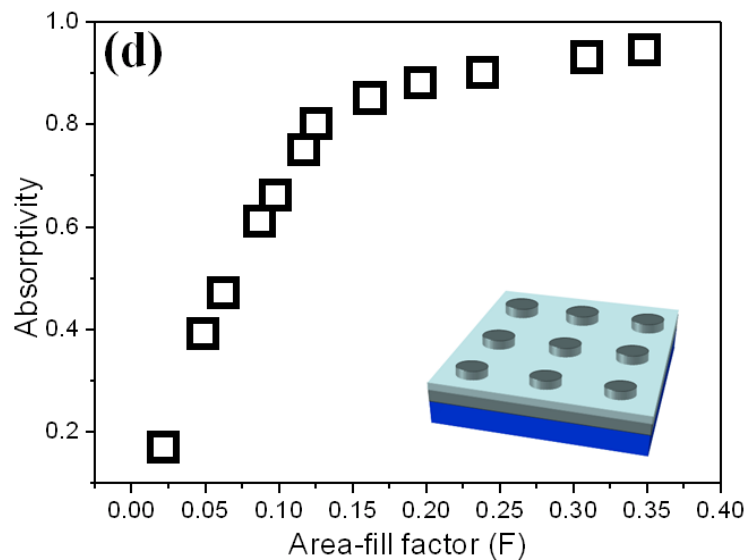
4.7-1(b) Absorptivities at normal incidence of the 1 μm MD arrays with several different periodicities Λ .



4.7-1(c) Absorptivities of the MD arrays with different diameters D for Λ fixed at 3 μm .

Since the MD density and size are associated with the area-fill factor (F) defined as the ratio of MD size to the unit cell area, the dependence of the absorptivity on the fill factor is shown in Figure 4.7-1(d). The absorptivity is linearly proportional to the fill

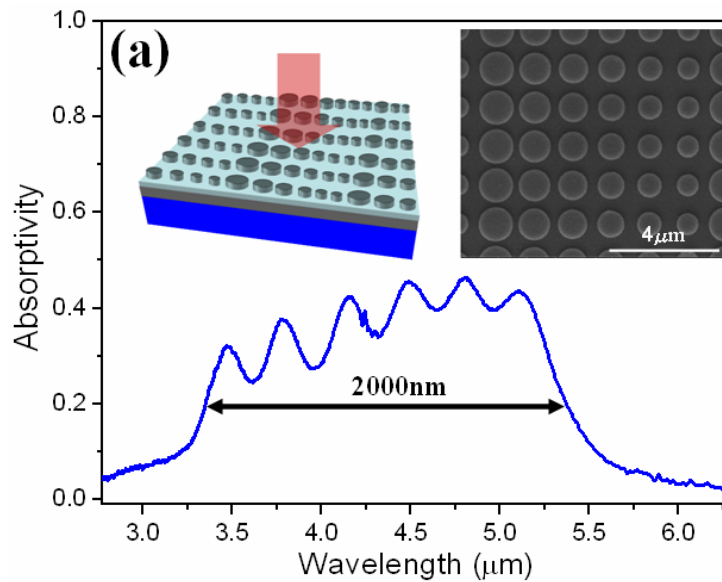
factor as $F < 0.24$ and it becomes saturated over 90% of absorption when F is greater than or equal to 0.24. The result that behaves similarly to the Beer Lambert law when $F < 0.24$ therefore allows us to control the absorption of the MD configuration.



4.7-1(d) Experimental peak absorptivity of the MD configuration as a function of its area-fill factor F .

With the above-mentioned absorption properties, we now turn toward experimental demonstrations of a broadband emitter and a high-performance dual-band absorber. Figure 4.7-2(a) shows the absorptivity of the broadband thermal emitter composed of the sublattices with six different disks from 800nm to 1.35 μm , where the distance between the nearest-neighbor disks is kept 1.5 μm . The absorbing spectrum is evidently broad as a result of the merging of six close peaks located closely to the resonant peaks for each of the single-sized MD absorbers. Although the

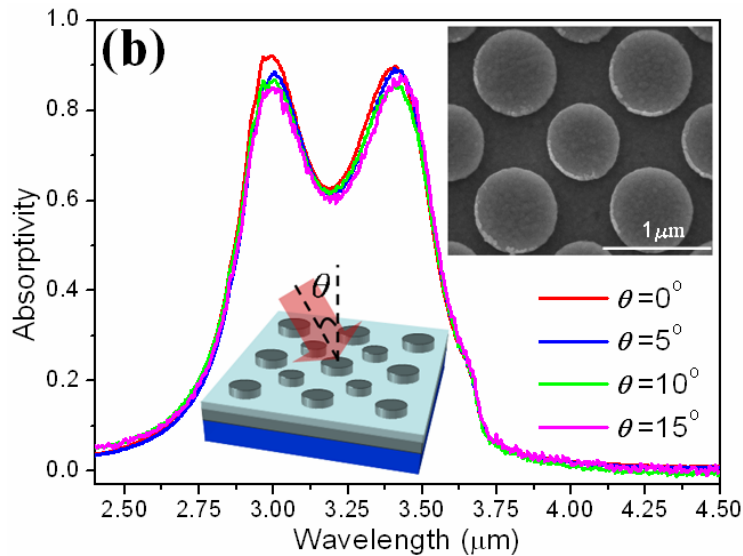
broadband emitter has a low absorptivity approximately 35% with a FWHM of 2000nm centered at the wavelength 4.32 μ m, high thermal emittance peaks of the emitter can be achieved by easily increasing heating temperature to modify the thermal dependence of the blackbody emittance curve $B(\lambda, T)$ as demonstrated in chapter 3 (see Figure 3.2-2(b)) and the literatures [31, 65] without changing emissivity.



4.7-2(a) Experimental absorptivity of the broadband absorber composed of the multi-sized disks with $D=800$ nm, 900 nm, 1.03 μ m, 1.12 μ m, 1.21 μ m, and 1.35 μ m and a SiO_2 spacer thickness, $t_{\text{SiO}_2}=32$ nm.

To obtain a broadband absorber with higher absorptivity, multi-sized MD disks within one unit cell and large area-fill factors for each of the disks are essentially required. However, if all the disks are patterned on the same layer, there is a design

trade-off between the multi-sized disks and fill factors corresponding to a number of absorption bands and absorption intensities. In spite of the trade-off, a high performance angle and polarization independent dual-band absorber can be realized.



4.7-2(b) Absorptivity of the dual-band absorber consisting of two different disk sizes with dimensions $D=825$ nm, and 960 nm per unit cell when $t_{\text{SiO}_2}=80$ nm.

Figure 4.7-2(b) exhibits the absorptivity of the dual-band absorber with a SiO_2 spacer of 80nm where the incident angle varies from 0° and 15° . The two molecule-like disks $D=825\text{nm}$, and 960nm are arranged to form a $1.5\mu\text{m}$ face-centered unit cell with the area-fill factors of the disks $F=0.24$ and 0.32 . As can be seen, the two strong absorption bands found at $2.99\mu\text{m}$ and $3.40\mu\text{m}$ have a maximum absorptivity of 92% and 90% , exhibiting consistency with that predicted by their area-fill factors in Figure 4.7-1(d). The absorptivity in both peaks remains at

more than 84% at an oblique incident angle. By effectively modifying the disk sizes and area-fill factors as well as the SiO₂ spacer, such dual-band absorber configuration not only can achieves high absorptivity, but also can offer wide-angle polarization independent flat absorption bands over an angle of incidence 50° compared with the H-shaped metamaterial coating [22].

4.8 Summary

In summary, we have demonstrated a 1D plasmonic IR filter/absorber with a localized, angle-independent LSPP mode by using the Ag/SiO₂/Ag T-shaped array. The resonance wavelength can be shifted by varying the geometry, and the angle-independence of LSPP mode was also verified. The T-shaped structure with the LSPP resonance has a strong advantage in the application as angle-independent band-stop filters. To further improve the absorption performance of the T-shaped structure, we therefore studied the two-dimensional round-shaped MD array.

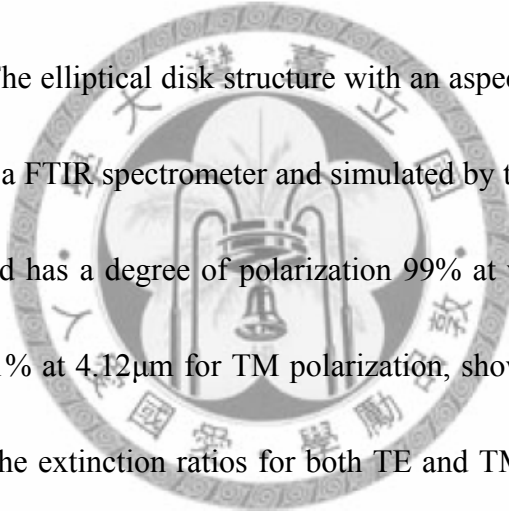
In the study, we have presented a method to control the absorptivity of the MD absorber by modifying its area-fill factor. Because of the LSPP resonances for the MD absorbers not affected by their array periodicities, a broadband emitter made of a multi-sized MD array can be realized. By controlling the disk sizes and fill factor, we have shown an angle and polarization independent dual-band absorber with two

maximal absorptivities over 84%. The incidence angle of the absorber can be achieved near 90° in the operating mid-infrared region from 2.85μm to 3.65μm. The approach is applicable for thermal photovoltaic, sensor, and camouflage applications.



5. Omni-directional mid-infrared (MIR) polarizer made of elliptical metal disk arrays

We have shown in chapter 4 that the metallic round-shaped disk array possesses a LSPP mode for both TE and TM polarizations. In the chapter, we found that by tuning the aspect ratio of the disk structure, both angle-independent TE- and TM-polarized resonant peaks can be separated. Because of its low-cost building materials and strong absorptivities occurring at both peaks, a cheap mid-IR polarizer possibly used can be realized. The elliptical disk structure with an aspect ratio of $b/a=0.65$ was characterized by using a FTIR spectrometer and simulated by the RCWA method. The disk structure we found has a degree of polarization 99% at wavelength $5.25\mu\text{m}$ for TE polarization and 91% at $4.12\mu\text{m}$ for TM polarization, showing a good agreement with our simulation. The extinction ratios for both TE and TM resonances are found to be 20dB and 14dB respectively. The ratios can be further improved by tailoring the aspect ratio of the disk structure.



5.1 Design and simulation of the MIR polarizer

Figure 5.1-1 shows the geometry of the elliptical disk array structure. The array structure consists of three layers: Ag disk layer, SiO₂ layer, and Ag reflective layer. The first Ag layer is an array of elliptical metal disks with two axes: major axis (a) along x-direction and minor axis (b) along y-direction. The periodicity of the array is denoted by Λ_g . The thickness of elliptical disk is given by $t_{Ag}=100\text{nm}$. The second layer is a uniform layer of SiO₂ with thickness $t_{SiO_2}=50\text{nm}$. To block the light transmittance, we used Ag thin film (100 nm) in the third layer to act as a reflector layer. Our simulation based on the RCWA algorithm specially is designed for the arrays.

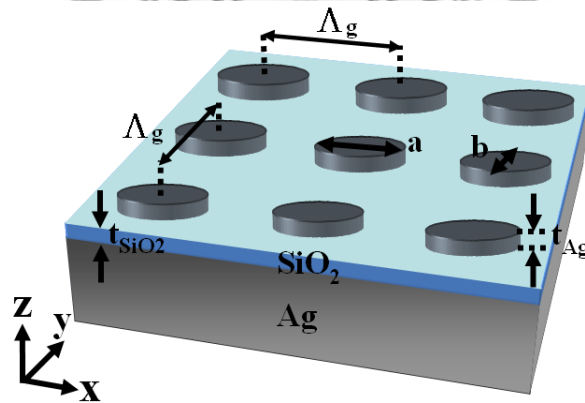


Fig. 5.1-1 Illustration of the metallic disk array structure.

Figure 5.1-2(a) and 5.1-2(b) show the TM-mode and TE-mode reflectance spectra of an elliptical disk array with parameters of $\Lambda_g=1500\text{nm}$, $a=1000\text{nm}$, and

$b=850\text{nm}$. The resonance energies (wavelengths) occur at 0.337eV ($3.68\mu\text{m}$) and at 0.378eV ($3.28\mu\text{m}$) for TM mode and TE mode, respectively. It is clear that both energy bands for the TM and TE modes are angle-independent due to the strong coupling of SPPs from the top and bottom Ag layers. The $|H_y|^2$ and $|H_x|^2$ field distributions at the SiO_2 layer becomes a linear combination of two exponentially decaying SPPs from the two Ag/ SiO_2 interfaces, as shown in Figure 5.1-3(a) for the TM modes and 5.1-3(b) for the TE mode. The coupling of SPPs will form a Fabry-Pérot-like resonance in the Ag/ SiO_2 /Ag elliptical metal disk cavity. The resonant mode is also called LSPP mode which is independent of incidence angles. The TM and TE modes are respectively resonances along the major axis x and minor axis y .

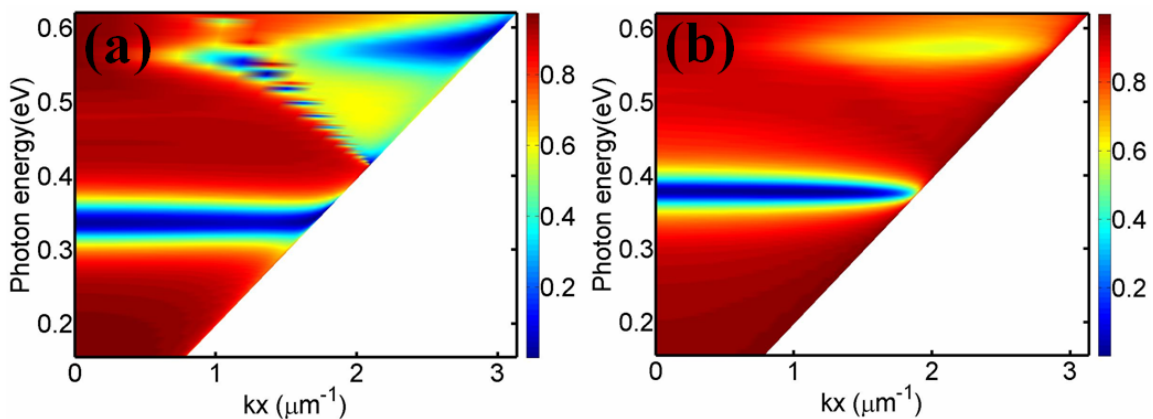
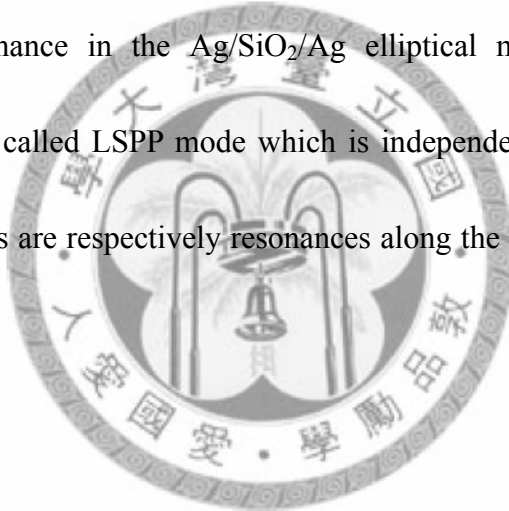


Fig. 5.1-2 Dispersion relations of the metal disk structure for (a) TM mode and TE mode.

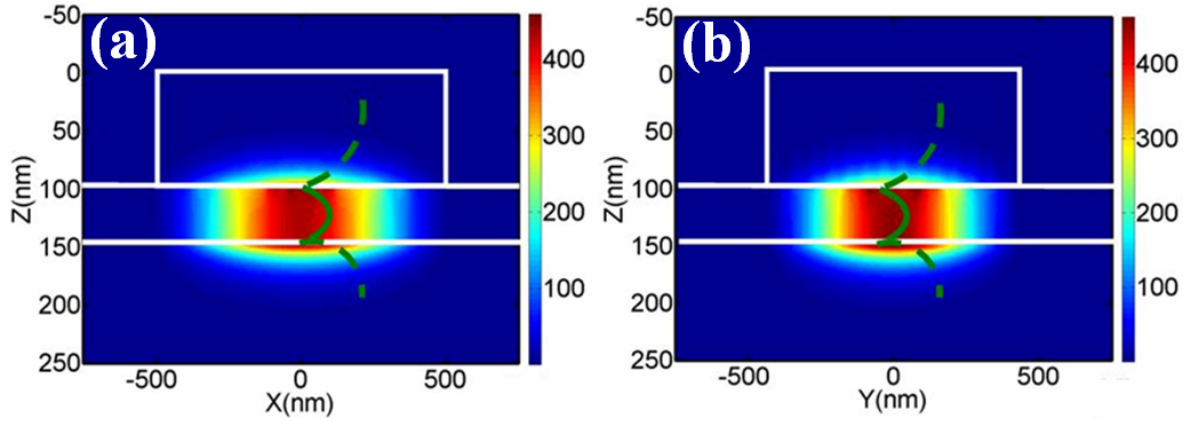


Fig. 5.1-3(a) $|H_y|^2$ field distribution for TM-mode at 0.33eV in X-Z plane. (b) $|H_x|^2$ field distribution for TE-mode at 0.37eV in Y-Z plane.

One of the useful features in the elliptical metallic disk is that the structure can filter out completely one component of the light polarization and reflects perfectly the other component of the light polarization because of the highly absorptions caused by the TE and TM modes. Therefore, the elliptical disk structure is a good candidate as a polarizer at mid-infrared region. We also found that by modifying the b/a ratio, the extinction ration defined as $10\log\left(\frac{I_{\text{wanted}}}{I_{\text{unwanted}}}\right)$ can be tuned, where I_{wanted} and I_{unwanted} are the reflection of the wanted and unwanted intensities. For the TM mode, it can filter out TM-polarized input light and reflect TE-polarized out light. Therefore, I_{wanted} and I_{unwanted} for the mode are I_{TE} and I_{TM} .

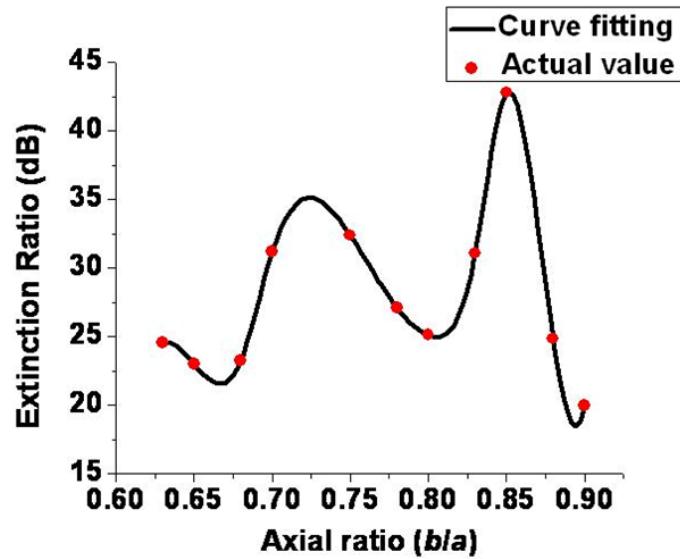


Fig. 5.1-4 Calculated extinction ratio versus axial ratio

Fig. 5.1-4 shows the extinction ratio of the TM mode versus the b/a ratio where $a=1000\text{nm}$ is fixed. As the ratio of axes decrease from $b/a=1$, the extinction ratio becomes higher than 20dB and the optimum value can be observed when the axes ratio is 0.85 which can lead to extinction ratio higher than 40dB. In addition to the polarization feature, the building material cost of the elliptical disk structure is cheaper compared with the IR-transmitting building materials such as CaF_2 , BaF_2 , and ZnS [68] used for the commercial polarizers.

5.2 Fabrication of the MIR polarizer

The fabrication processes of the oval-shaped metal disk arrays are described as follows. A 100 nm thick silver film was deposited on a silicon substrate by an electron gun evaporator to act as a reflector layer, which is followed by the deposition of a 50

nm SiO₂ film using plasma-enhanced chemical vapor deposition (PECVD) (Recipes for the SiO₂ and Ag depositions shown in Appendix C). Then, a PMMA layer was coated on the top of the SiO₂ layer. An array of elliptical holes (with the major axis a and minor axis b) periodically spaced with a lattice constant of Λ_g in both the x and y directions were defined on the PMMA layer by electron beam lithography. The pattern was then developed and a 100 nm thick silver layer was deposited to fill the holes. Finally, the metal disk array was obtained by lifting the PMMA layer off. Figure 5.2-1 is a SEM image of the fabricated structure with a=1.5 μ m, b=650nm, t_{SiO_2} =50nm and Λ_g =2 μ m.

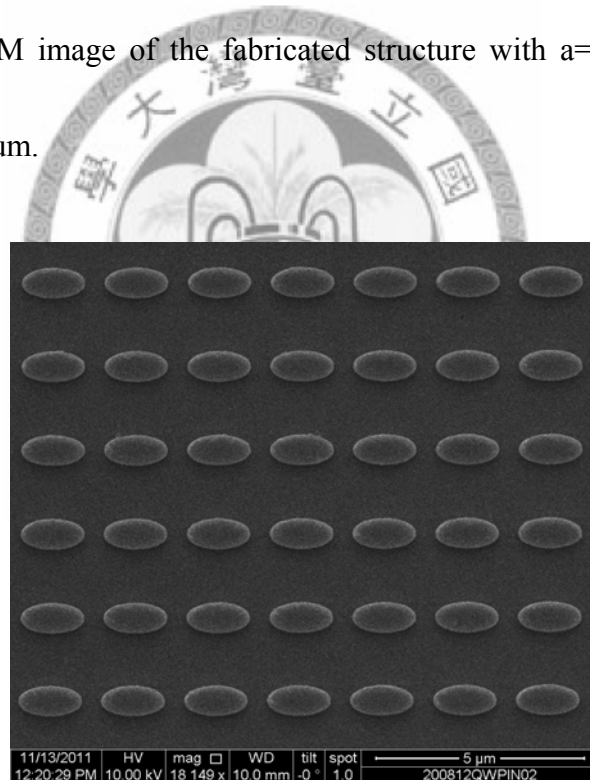


Fig. 5.2-1 SEM image of an elliptical disk array.

5.3 Experimental results and discussion

The reflectance spectrum of the fabricated device with geometric parameters of

$\Lambda_g=2000\text{nm}$, $a=1500\text{nm}$, $b=1000\text{nm}$, $t_{\text{SiO}_2}=50\text{nm}$, and $t_{\text{Ag}}=100\text{nm}$ was measured by a FTIR system. The back-reflected light from the sample through a $50\mu\text{m}\times 50\mu\text{m}$ slit was collected and detected using a MCT (mercury-cadmium-telluride) photodetector with a spectral resolution of 2 cm^{-1} . Figure 5.3-1(a) shows the reflectance spectra at normal incidence for TM-, TE- and un-polarized incident light. The dip with a FWHM of 430nm in the TM-mode reflectance spectra occurs at the wavelength $5.25\mu\text{m}$ and dip with a FWHM of 323nm for TE-mode at wavelength $4.12\mu\text{m}$. The degree of polarization is 99% for TE-polarized reflectance at $5.25\mu\text{m}$ and 91% for TM-polarized reflectance at $4.12\mu\text{m}$. The unpolarized incident light spectrum shows two dips, one due to the absorbance of the TM mode and the other due to the absorbance of the TE mode. The corresponding simulation of the TE- (circle) and TM- (triangle) polarized modes is also shown in Figure 5.3-1(a). This shows a good agreement with our measurement. The extinction ratios for both TE- and TM-polarized reflectance are 20dB and 15dB.

In order to determine the polarization state of the reflective beam from the sample, a MIR polarizer was used and placed in front of the device. As the polarizer was rotated, the signal intensity as a function of the rotation angle was observed and shown in Figure 5.3-1(b).

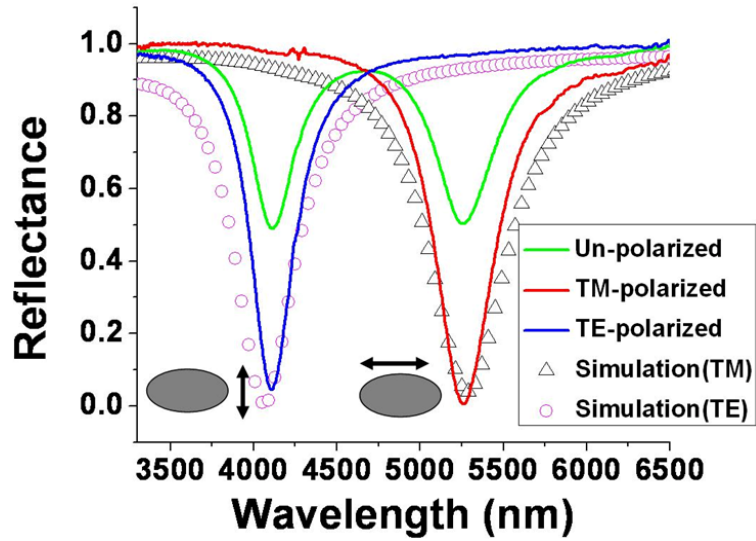


Fig. 5.3-1(a) Measured reflectance spectra of the proposed metal disk structure for TM-polarized light (red), TE-polarized light (blue), and un-polarized light (green). The corresponding simulated spectra for TM- and TE- polarized light are shown in triangles and circles, respectively.

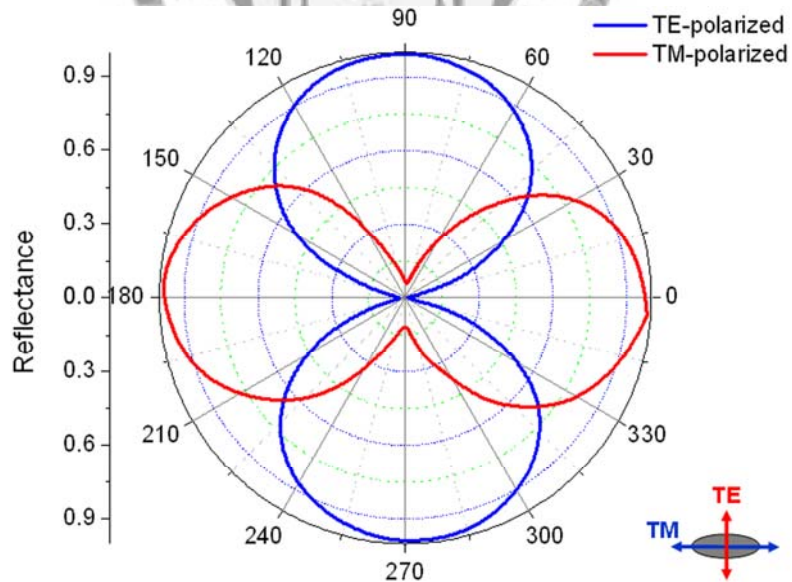
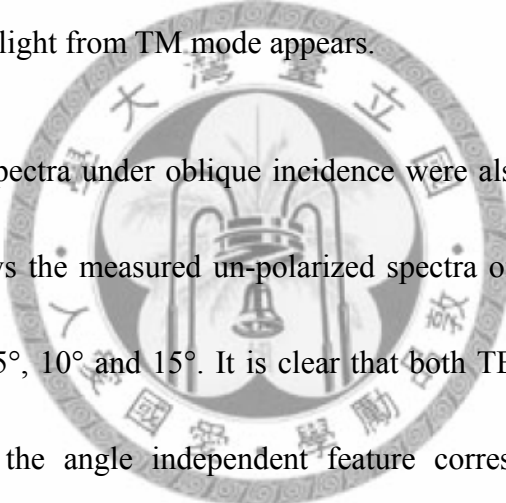


Fig. 5.3-1(b) Polar diagram of the reflectance spectra versus polarizer rotating angle where the TE- and TM- polarizations of light by reflection are shown in red and blue curves.

The maximum TM-polarized reflection light intensity occurs at a rotation angle of 0° and 180° , corresponding to the TE-polarized resonance along the minor axis. For the TE-polarized reflection light, the maxima appear at an angle of 90° and 270° related to the TM-polarized resonance along the major axis. It is also shown that the immunity against interfering polarization is about $\pm 30^\circ$. When the polarizer angle rotates from -30° to 30° , the TM-polarized reflected output light from TE mode can only be observed. Similarly, when the polarizer angle rotates from 60° to 120° , only output TE-polarized reflected light from TM mode appears.



The absorbance spectra under oblique incidence were also measured from 0° to 15° . Figure 5.3-2 shows the measured un-polarized spectra of the structure with the incident angles of 0° , 5° , 10° and 15° . It is clear that both TE and TM peaks do not shift which confirms the angle independent feature corresponding to the LSPP resonances. The LSPP resonances of the elliptical disk structure can also be tuned by either the major axis a or the minor axis b . The absorbance spectra varying with b were measured when the major axis was kept around 1511nm , as shown in Figure 5.3-3. It can be seen that the TE-mode resonance wavelength was blue-shifted as the size of the minor axis is decreased from 1511nm to 585nm while the TM-mode resonance wavelength kept almost the same position. We can expect the same thing happen (results not shown) for TM-mode resonance wavelength as we change the

major axis instead minor axis of the elliptical disk.

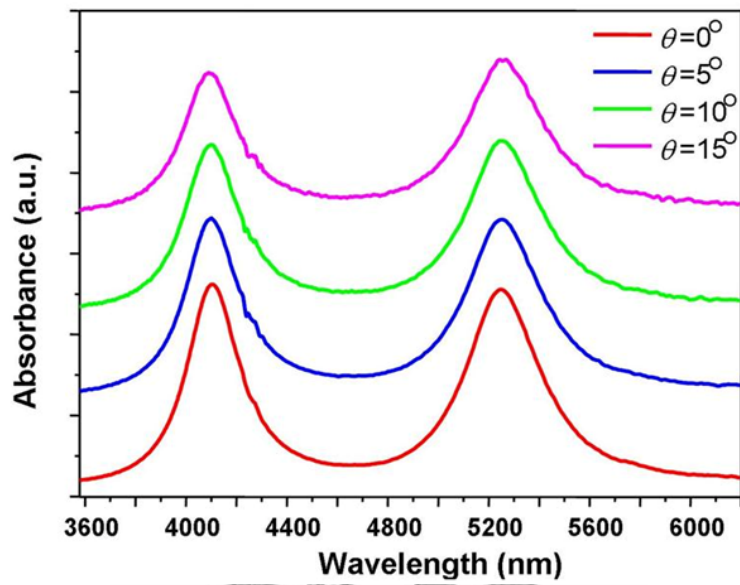


Fig. 5.3-2 Absorbance spectra at different incident angles from 0° to 15° .

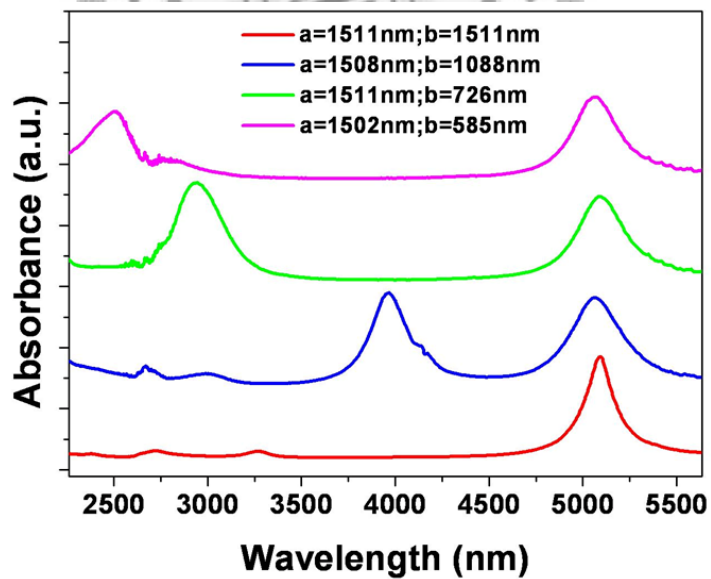
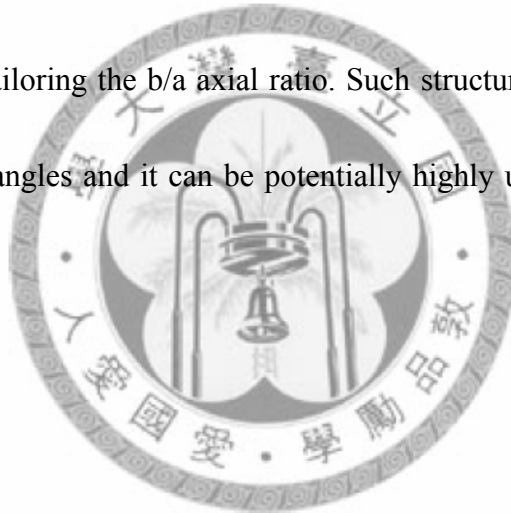


Fig. 5.3-3 Measured absorbance spectra for different minor axes from 585nm to 1511nm

when the major axis a is fixed approximately 1511nm.

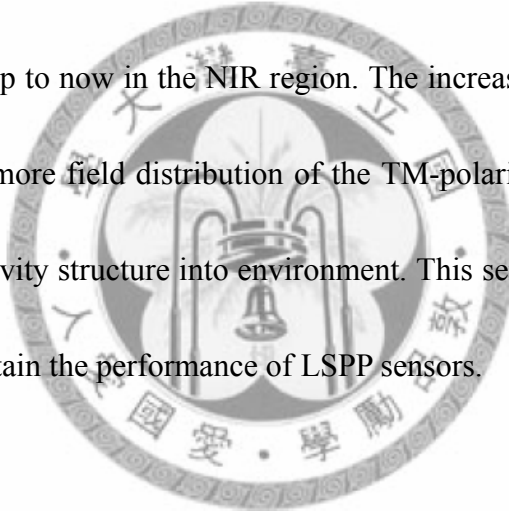
5.4 Summary

Plasmonic mid-infrared polarizer consisting of an elliptical metallic disk array on SiO₂ thin film layer has been investigated. We have shown that both TM- and TE-resonant wavelengths occur respectively at 5.25 μ m with a degree of polarization 99%, and 4.12 μ m with a degree of polarization 91%. The polarized wavelengths can also be controlled in a wide range by tuning its geometric parameters a or b. The extinction ratios for both TM and TE modes are found to be 15dB and 20dB, all of which can be further improved by tailoring the b/a axial ratio. Such structure has also an ultrahigh immunity to incident angles and it can be potentially highly used as a cheap mid-IR polarizer.



6. Plasmonic index sensor made of elliptical metal disk arrays

In the chapter, we will introduce a novel concept for the improvement in sensitivity and the reduction on sensing peak width broadening. Based on the elliptical shaped disk array structure in chapter 5 with the SiO₂ layer etching, a high-performance plasmonic index sensor operating at wavelengths from 1000nm to 1800nm can be realized. The sensitivity 691nm/RIU and FOM 2.5 can be achieved to be the highest record up to now in the NIR region. The increase of the sensitivity and FOM is due to much more field distribution of the TM-polarized LSPP mode out of the elliptical shaped cavity structure into environment. This sensing strategy can offer great potential to maintain the performance of LSPP sensors.



6.1 Device description

In Chapter 5, the oval-shaped disk structure as a MIR wide-angle polarizer (see Figure 5.1-1) was introduced. It possesses TE- and TM- polarized modes, corresponding to the transverse and longitude resonances along y and x axes, respectively. To restrict resonant peak broadening under sensing measurements as shown in the literature [69], an Au/SiO₂/Au based structure is therefore proposed because of the structure acting as a cavity able to provide a stable quality factor Q in its resonant frequency spectra. We also found that the shape of the Au/SiO₂/Au disk plays an important role in the field of high sensitivity optical sensing.

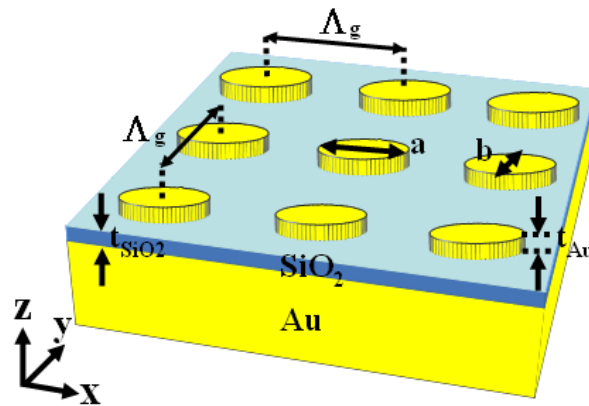


Fig. 6.1-1 Illustration of the Au/SiO₂/Au based structure.

As an example of the Au/SiO₂/Au structure ($\Lambda_g=1000\text{nm}$, $t_{\text{Au}}=20\text{nm}$, $t_{\text{SiO}_2}=90\text{nm}$) without the SiO₂ layer etching (Figure 6.1-1), when the aspect ratio b/a becomes smaller from 1 ($D=a=b=300\text{nm}$) to 0.57 ($a=300\text{nm}$, $b=171\text{nm}$), the percentage of the TM-mode $|H_y|^2$ field leaking out into the ambient is increased from 9% to 15%, as

shown in Figure 6.1-2(a) and 6.1-2(b). The leakage field is mainly caused by the off-resonance of the SPP coupling between the top metal disk and the bottom Au layer along y-axis. The leakage field strength and distribution in the ambient will distort the resonance field in the SiO₂ cavity structure, giving rise to a change in resonant wavelength shift per unit refractive index. The sensitivities of the round-shaped and oval-shaped disks are 372nm/RIU and 486nm/RIU (see Figure 6.1-4).

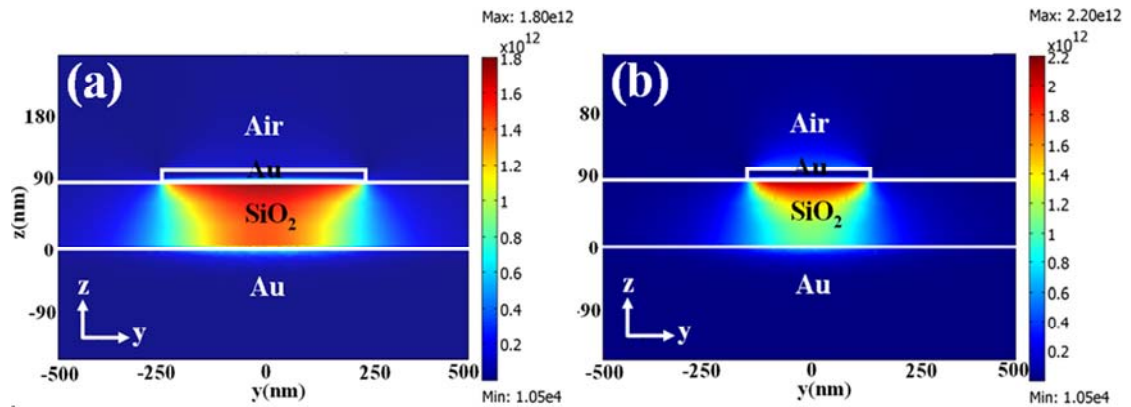


Fig. 6.1-2 $|H_y|^2$ distributions of the (a) round-shaped metal disk and (b) oval-shaped disk structures within one unit cell at the Y-Z plane when X=0.

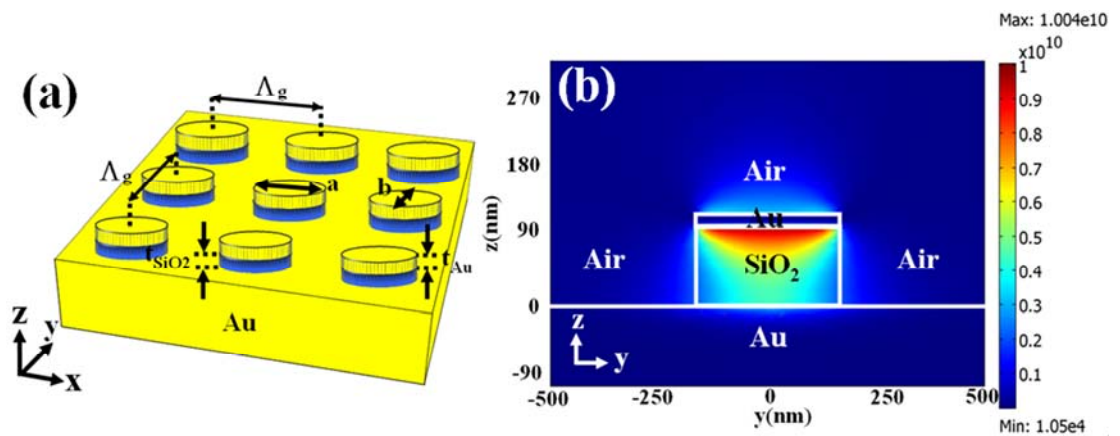
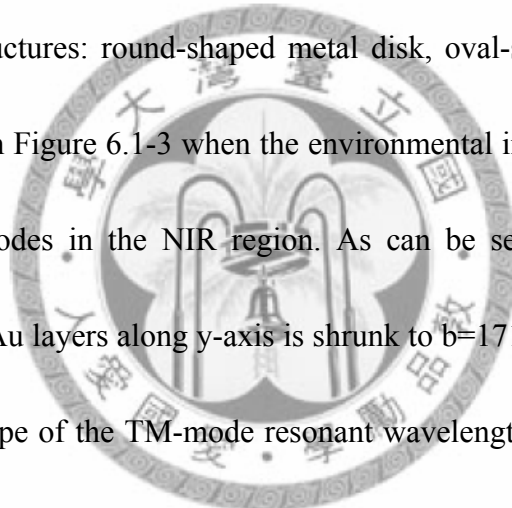


Fig. 6.1-3 (a) Illustration of the oval-shaped Au/SiO₂ disk structure. (b) $|H_y|^2$ distribution within one unit cell at the Y-Z plane when X=0.

To improve the sensitivity, strong leakage field strength and much more distribution leaking into the ambient are essentially concerned. The Au/SiO₂ elliptical disk structure with the SiO₂ layer etching is therefore proposed, as depicted in Figure 6.1-3(a). Because of the leakage field $|H_y|^2$ into the air for Au/SiO₂ elliptical disk array much more than the elliptical metal one (see Figure 6.1-2 (b) and Figure 6.1-3(b)), the sensitivity in the Au/SiO₂ elliptical disk structure will outperform that in the oval-shaped structure. Figure 6.1-4 presents the evaluation of the wavelength shifts of the three structures: round-shaped metal disk, oval-shaped metal disk, and Au/SiO₂ disk shown in Figure 6.1-3 when the environmental index is changed from 1 to 1.4 for the TM modes in the NIR region. As can be seen, when the Au disk structure on the SiO₂/Au layers along y-axis is shrunk to b=171nm and along x-axis is kept a=300nm, the slope of the TM-mode resonant wavelength change per refractive index unit becomes pronouncedly increasing to 486nm/RIU with respect to the round-shaped metal disk structure. As to the Au/SiO₂ elliptical shaped disk structure with a=300nm and b=171nm on the bottom Au layer, the sensitivity of the TM mode is remarkably increased and can be achieved to 956nm/RIU. In comparison to the former designs, a great sensitivity of the TM mode in the latter structure can therefore be feasibly achieved as a high-sensitivity sensor.



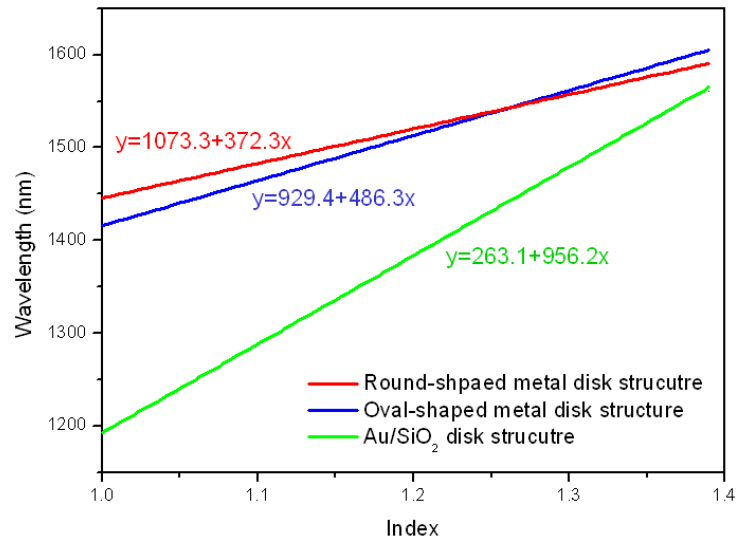


Fig. 6.1-4 Numerical simulations of the sensitivities for the three structures.

6.2 Fabrication of the Au/SiO₂ cavity based structure

A 5nm Cr adhesion layer and a 100 nm gold layer were deposited on the top of a silicon substrate, followed by a thickness of SiO₂ thin film and a 20nm gold layer deposited by PECVD and e-gun deposition (Recipes for the SiO₂ and Au depositions shown in Appendix C). A PMMA layer was then spin-coated on the top of the SiO₂ layer. An array of the elliptical disks as an etching mask periodically spaced with a lattice constant Λ in x and y directions was defined on the PMMA layer by electron beam lithography. After developing the resist, a reactive ion etching (RIE) system and an inductively coupled plasma (ICP) system with CHF₃/O₂ gas were applied to dry etch the top 20nm gold layer and the SiO₂ layer, respectively (RIE recipe for the Au layer and ICP recipe for the SiO₂ layer all shown in Appendix C). Finally, the sensor

structure was completed via a PMMA cleaning process. Figure 6.2-1 is a SEM image of the fabricated structure. The inset shows the details of the structure with a tilt angle of 30°.

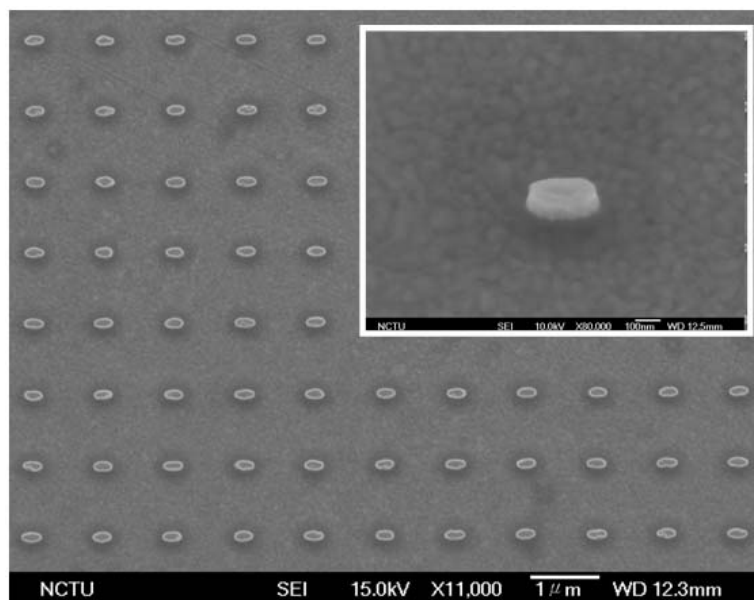


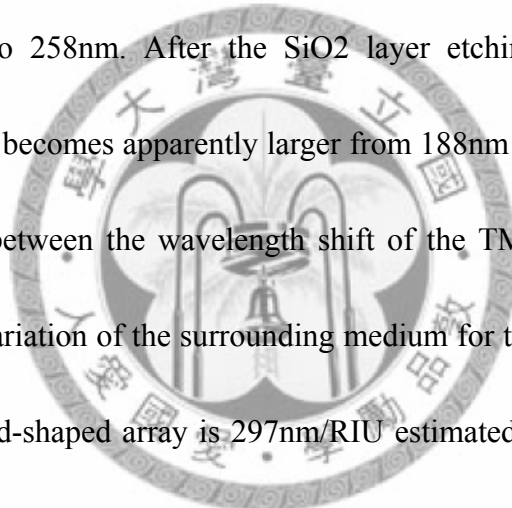
Fig. 6.2-1 SEM view of the oval-shaped Au/SiO₂ disk structure.

6.3 Experimental results and discussion

To obtain the absorbance spectra of the structures, a Bruker Fourier Transform IR spectrometer was used. A near-infrared (NIR) un-polarized light source was focused on the samples with a 0.4 numerical aperture. The back-reflected light from the samples through a 50μm×50μm slit was collected and detected using a MCT photodetector with a spectral resolution of 2 cm⁻¹.

The sensitivities were measured by immersing the samples in index matching liquids with the indices from 1.3 to 1.39. Figure 6.3-1 shows the measured absorbance

spectra of the three types of array structures in the wavelength range of 1000nm to 1800nm. In the measurements after sample immersion in the liquids, the peak wavelengths of the TM modes are all red-shifted. The full-width at half maximum (FWHM) of the measured resonance peak becomes increasing broader. For the Au round-shaped disk array with a diameter of $D=314\text{nm}$ on 90nm-thick SiO_2 and Au layers, the FWHM is increased from 134nm to 209nm. When the round-shaped disk is squeezed along y-axis with $b=171\text{nm}$, and $a=300\text{nm}$, the resonance peak width is varied from 180nm to 258nm. After the SiO_2 layer etching with $a=283\text{nm}$ and $b=146\text{nm}$, the FWHM becomes apparently larger from 188nm to 282nm. Figure 6.3-2 presents the relation between the wavelength shift of the TM-polarized LSPP band and refractive index variation of the surrounding medium for the three structures. The sensitivity of the round-shaped array is 297nm/RIU estimated by fitting the slope of the wavelength shifts with the method of least-squares, showing a good agreement with our simulation 300nm/RIU. The figure of merit (FOM) defined as the ratio of the sensitivity to the FWHM is found to be 1.4. For the Au oval-shaped disk array with and without the SiO_2 layer etching, the sensitivities are 515nm/RIU and 691nm/RIU with a FOM of 2.0 and 2.5, respectively. The improvement of the sensitivity and FOM is due to an increase in leakage field distribution out of the disk structure into ambience and the disk resonant cavity which is able to be against the FWHM



broadening when the sample is immersed in the index liquids during the measurements. The sensitivity 691nm/RIU with a high FOM of 2.5 is among the highest reported for LSPP-based plasmonic index sensors in the near-infrared (NIR) region when comparing the slablike gold nanoring structure with a sensitivity of 691nm/RIU and FOM near 1.7 [69]. From the above experimental data and simulated results, it suggests that the Au/SiO₂ oval-shaped disk array structure not only can offer high performance sensing quality, but also can provide omnidirectional detection and operating wavelength tunability. The structure therefore can be a good candidate as a highly performance incident-angle-independent plasmonic sensor.

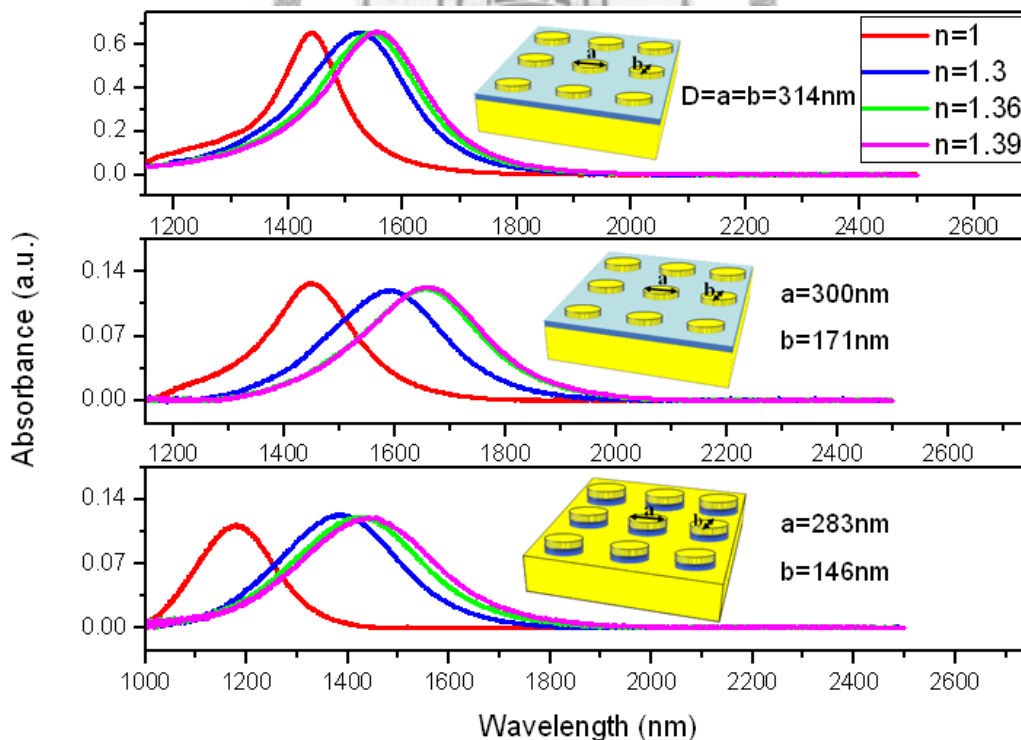


Fig. 6.3-1 Measured absorbance spectra of the three structures with liquid indices from 1 to 1.39.

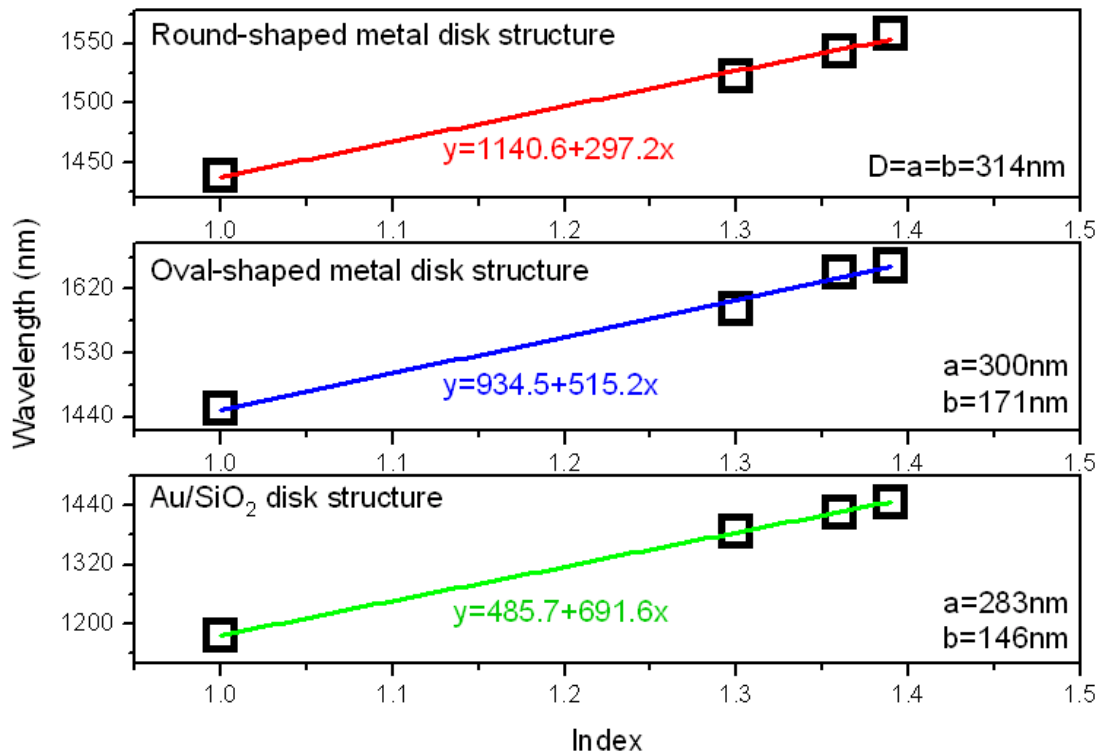


Fig. 6.3-2 Peak wavelength shifts in the TM-modes of the three structures.

6.4 Summary and future work

In summary, we have experimentally demonstrated a plasmonic index sensor in NIR region, which is independent of angle of incidence. With the Au/SiO₂ oval-shaped design, the sensitivity can achieve up to 691nm/RIU with a FOM of 2.5. The sensitivity and FOM are improved by increasing much more leakage field out of the Au/SiO₂ oval-shaped cavity into the surrounding environment. The sensing principle of the designed structure opens up a new pathway for the enhancement of plasmonic sensing. Such miniaturized sensor can be promisingly used in integrated sensing platforms or subwavelength optics on-a-chip for chemical and biomolecule

detections. In the future work, we will cooperate with Professor Yi-Chung Tung at Academic Sinica to produce target cells on such device for the cell detection.



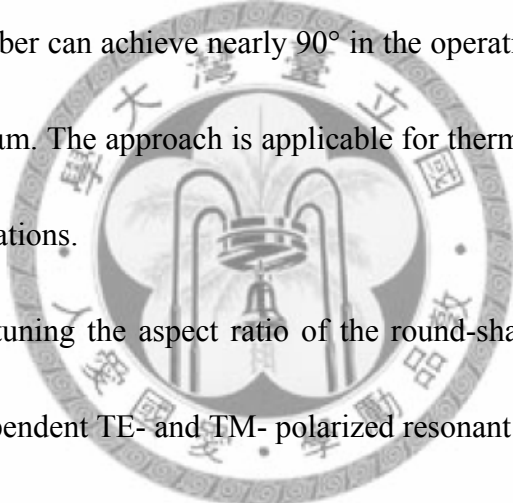
Chapter 7. Conclusion

Based on the Kirchhoff's law of thermal radiation, we demonstrated an angle and polarization independent narrow-band thermal emitter as an active plasmonic device. The device is made of metallic disks with $D=1.15\mu\text{m}$ and $\Lambda=3\mu\text{m}$ on a SiO_2/Ag substrate. The emission peak was found at $4.27\mu\text{m}$ with a FWHM of $0.25\mu\text{m}$ for both TE and TM polarization. The resonance peak also can be tuned by either changing the disk diameter or SiO_2 thickness. This kind of emission property with narrow bandwidth, low sideband and high intensity is very useful for the application in IR light sources.

Regarding to passive plasmonic devices, a one-dimensional angle-independent IR filter/absorber with $\Lambda_g=3000\text{nm}$, $t_{\text{Ag}}=100\text{nm}$, $t_w=50\text{nm}$, $W_T=800\text{nm}$, and $W_{\text{Ag}}=1100\sim 2000\text{nm}$ was investigated and characterized in chapter 4. The optical filtering/absorbing property is caused by a Fabry-Pérot resonance corresponding to an angle-independent LSPP mode. By adjusting the W_{Ag} from 1910nm to 1300nm , the LSPP resonance wavelength can be linearly tuned with a rate of 3.8 nm per nm in W_{Ag} , in agreement with our RCWA simulation. The T-shaped structure with the LSPP resonance therefore has a strong advantage for single-band rejection applications.

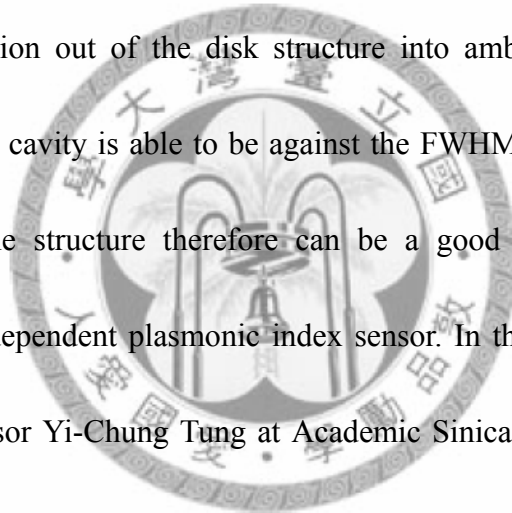
To further improve the absorption performance of the T-shaped structure, two-dimensional round-shaped metallic disk arrays on a $\text{SiO}_2/\text{Ag}/\text{Si}$ substrate was

peoposed. We found that the metallic disk exhibits a LSPP mode independent of the disk periodicities. Therefore, a broadband emitter composed of the sublattices with six different disks from 800nm to 1.35 μ m can be realized. The emission bandwidth could achieve 2000nm centered at the wavelength 4.32 μ m. In addition, by controlling the disk sizes and disk area-fill factor, the absorptivity of the 2D array absorber can be tuned. With the ideal, we demonstrated an angle and polarization independent dual-band absorber with two maximal peak absorptivities over 84%. The angle of incidence for the absorber can achieve nearly 90° in the operating mid-infrared region from 2.85 μ m to 3.65 μ m. The approach is applicable for thermal photovoltaic, sensor, and camouflage applications.



In chapter 5, by tuning the aspect ratio of the round-shaped disk structure, we found both angle-independent TE- and TM- polarized resonant peaks can be separated. Based of the strong absorption resonant bands and its low-cost building materials, a cheap omni-directional mid-IR polarizer made of an elliptical disk array with $\Lambda_g=2000$ nm, $a=1500$ nm, and $b=1000$ nm was demastrated. In the experiment, both TM- and TE- resonant wavelengths were observed respectively at 5.2 μ m with a degree of polarization 99%, and 4.1 μ m with a degree of polarization 91%. The extinction ratios for both TM and TE modes are 15dB and 20dB, all of which can be further improved by tailoring the b/a axial ratio.

In addition to the TE and TM separation property of the oval-shaped disk array structure, we found that the TM-mode $|H_y|^2$ field of the oval structure shows more leaky field to the atmosphere compared with the round-shaped structure, giving rise to an increase in the sensitivity to the environment. To further improve the sensitivity, an Au/SiO₂ elliptical shaped structure with a=283nm and b=146nm was proposed. The sensitivity 691nm/RIU and FOM 2.5 can be achieved to be the highest record up to now in the NIR region. The improvement of the sensitivity is caused by increasing leakage field distribution out of the disk structure into ambience. Furthermore, the Au/SiO₂ disk resonant cavity is able to be against the FWHM broadening, giving an increase in FOM. The structure therefore can be a good candidate as a highly performance angle-independent plasmonic index sensor. In the future work, we will cooperate with Professor Yi-Chung Tung at Academia Sinica to produce target cells on such device for the cell detection.



Appendix A

Characterization of the surface plasmon polariton band gap in an Ag/SiO₂/Ag T-shaped periodical structure

We investigated the localized surface plasmon polariton band gap based on an Ag/SiO₂/Ag asymmetric T-shaped structure [70]. The band gap will appear with an index contrast modification without additional periodic grating. The phenomenon to control the surface plasmon polariton band gap was simulated by RCWA and directly observed using a FTIR spectrometer. The T-shaped plasmonic periodical structure not only provides a new method for generating the band gap, but also provides a strategy to tune the LSPP band-gap with the geometry. Such a T-shaped structure with a LSPP band gap can be widely exploited in various applications, such as band gap waveguides, defect cavity lasers/emitters, and a study of nonlinear plasmonics.

Design and simulation

Figure A-1 shows the proposed Ag/SiO₂/Ag asymmetric T-shaped array with the geometric parameters as follows: $\Lambda_g = 1 \mu\text{m}$, $W_{\text{top}} = 550 \text{ nm}$, $t_{\text{top}} = 200 \text{ nm}$, $W_{\text{post}} = 200 \text{ nm}$, $t_{\text{post}} = 0 \sim 320 \text{ nm}$, $d = 50 \text{ nm}$, $G_t = 320 \text{ to } 0 \text{ nm}$, and $t_{\text{SiO}_2} = 320 \text{ nm}$.

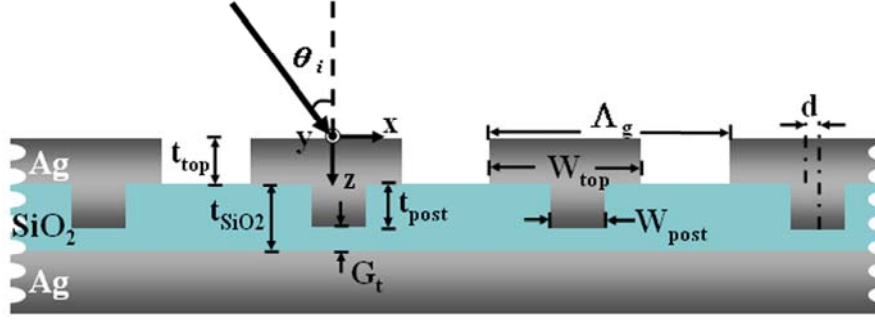


Fig. A-1 Schematic diagram of the T-shaped array structure

To understand the resonant behavior of the structure, its reflectance spectra and resonant mode profiles are calculated by RCWA simulation. In the simulation, because of no resonant response in the proposed structure for the TE-polarized light applied in our designed photon energy region, TM-polarized incident light (the magnetic field parallel to the y-axis) is used with different incident angles in the x-z plane. Figure A-2(a) shows the calculated reflectance spectra of the Ag/SiO₂/Ag multilayer structure ($t_{\text{post}}=0\text{nm}$ and $G_t=320\text{nm}$) with the photon energy ranging from 0.5 eV to 1.2 eV, while the angle of incidence θ_i varies from 0° to 90° . The crossings are from the grating coupling at the SiO₂/Ag interfaces and associated with the first Brillouin zone folding. The crossings all lies on the Bragg planes, and $k_x = m \pi/\Lambda_g$ where m is an integer. The slope of the dispersion indicates the group velocity ($v_g = \partial \omega / \partial k_x$) of the SPP propagation at the SiO₂/Ag interface. Due to less interaction between the two branches, the crossing point is found to be 0.87 eV at normal incidence, showing no energy gap in the dispersion relation. To form an energy gap,

additional periodic grating with a period of $\Lambda_g/2$ is commonly used [55, 71, 72]. The periodicity $\Lambda_g/2$ is designed to couple an energy gap region with photons inside the light line.

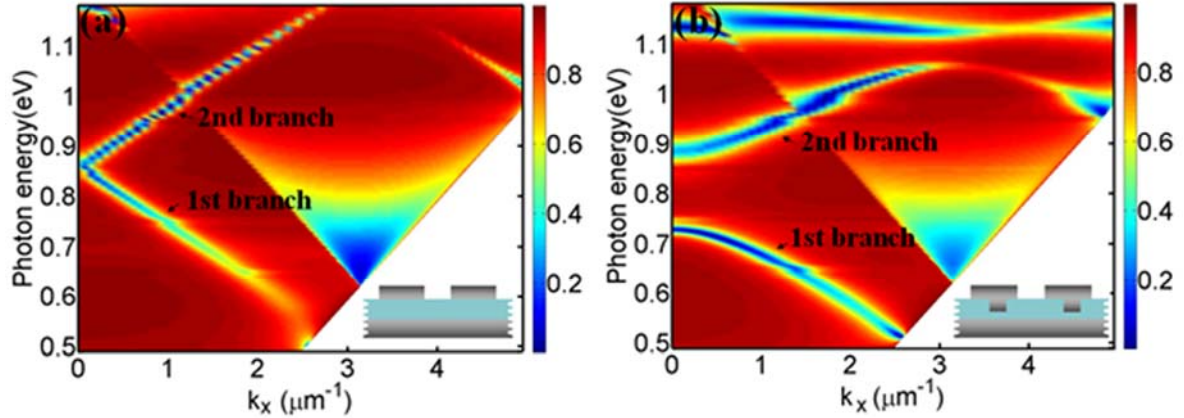


Fig. A-2 (a) Stimulated reflectance spectra of the multilayer structure with design parameters of $\Lambda_g=1 \mu\text{m}$, $W_{\text{top}}=550 \text{ nm}$, $t_{\text{top}}=200 \text{ nm}$, $W_{\text{post}}=200 \text{ nm}$, $d=0 \text{ nm}$, $t_{\text{post}}=0 \text{ nm}$, and $G_t=320 \text{ nm}$. (b) Stimulated reflectance spectra of the T-shaped structure when $d=50 \text{ nm}$, $t_{\text{post}}=170 \text{ nm}$, and $G_t=150 \text{ nm}$.

However, this study found that without using extra periodic grating, an energy gap can be opened when t_{post} is introduced, as shown in Figure A-2(b). The slope of the bent dispersion curves provides the group velocity in the x-direction as a function of the resonance wavelength and incident angle. At small values of k_x , we also found that a momentum band gap will occur in the first branch if the T-shaped structure becomes symmetric ($d=0\text{nm}$). The momentum gap is due to the non-coupling strength in the first branch and determined by the relative phase between the top grating strip

and the post structure [71, 73]. Regarding the $|H_y|^2$ distributions at normal incidence for the two branches of the designed structures, Figure A-3(a) shows the free-propagation-like field distribution at the bottom SiO₂/Ag interface along the x-direction in one pitch of the multilayer structure. Figures A-3(b) and A-3(c) are the field distributions for the two standing wave solutions at the first and second branches when the $t_{\text{post}} = 170$ nm. Most of the field intensity is concentrated in the corners between the post and the grating on the top layer for the first branch. Regarding the second branch, the intensity distribution reveals a periodicity equal to half the pitch period, with the strong field in the SiO₂ spacer below the post.

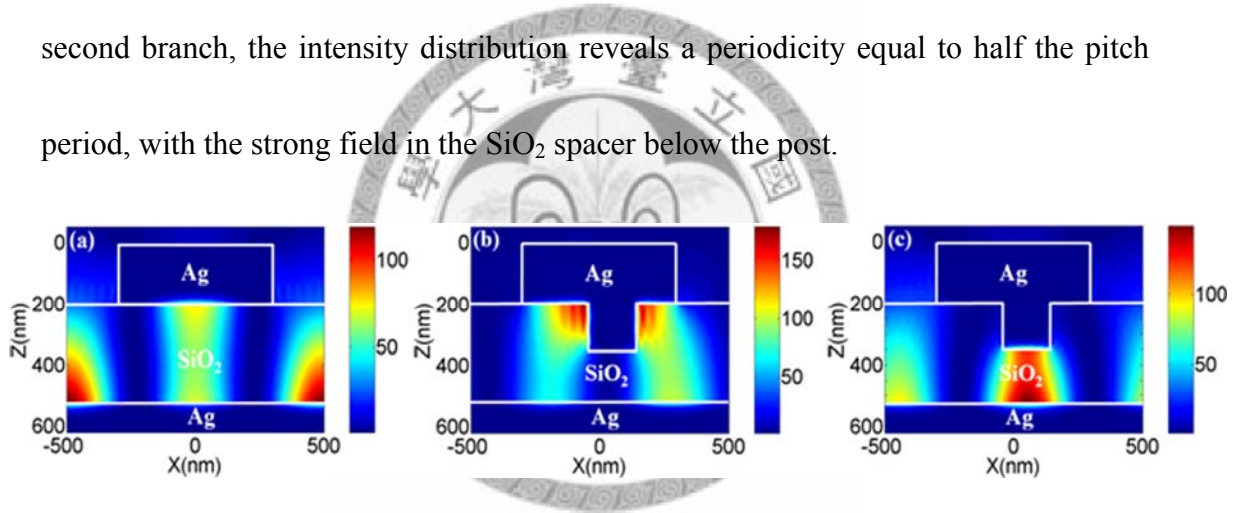
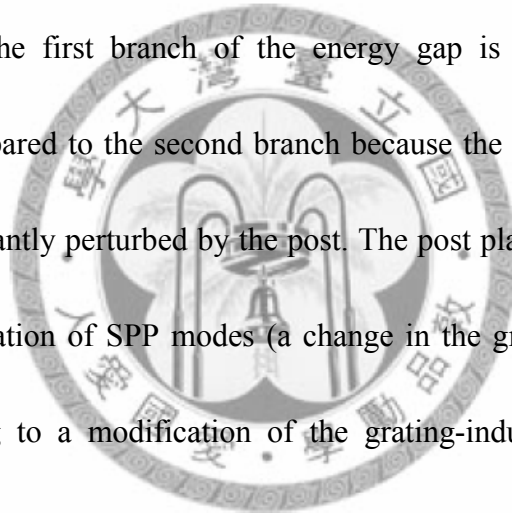


Fig A-3 $|H_y|^2$ distribution at normal incidence in one period of (a) the Ag/SiO₂/Ag multilayer structure at the crossing point 0.87 eV, and (b) the first and (c) second branches of the T-shaped structure when $d=50$ nm, $t_{\text{post}}=170$ nm, and $G_t=150$ nm.

The mechanism of the dispersion-relation modification arises from the impedance mismatch [74] between the metal-metal and single metal regions of the T-shaped structure, where the impedances of the metal-metal regions strongly depend on the geometric parameters t_{post} and W_{post} , and when the t_{SiO_2} and W_{top} are fixed. As

the t_{post} increases, the band gap progressively opens and is linearly proportional to the post height (t_{post}) when $0 < t_{\text{post}} \leq 270$ nm, as shown in Figure A-4(a). Because $t_{\text{post}} > 270$ nm ($G_t < 50$ nm), the band gap increase rate becomes nonlinear (not shown) due to the resonant mode of the second branch beginning to form Fabry–Perot resonance in the gap (G_t) between the post and the bottom layer. When G_t is decreased, the effective index of the mode will increase [63, 64]; hence, the resonant wavelength of the second branch is red-shifted. This study also observes that the resonance wavelength shift in the first branch of the energy gap is extremely sensitive to variations of t_{post} compared to the second branch because the field distribution in the first branch is significantly perturbed by the post. The post plays an important role in perturbing the propagation of SPP modes (a change in the group index for the SPP propagations), leading to a modification of the grating-induced line shape in the dispersion relation and energy-gap opening. This study also explores the energy-gap behavior in the varied W_{post} , as shown in Figure A-4(b). When the W_{post} increases, the first band is shifted upwards to high energy, whereas the second band is moved downwards. Eventually, both branches meet at approximately 0.80 eV when $W_{\text{post}} = 450$ nm. We expect that when the W_{post} is adjusted, both resonance modes of the two branches (see Figures A-3(b) and A-3(c)) are modified along the x-axis, shifting all their resonance energies. In comparison to the results shown in Figures 4.1-4(a) and



A-4(b), the band gap's tunability with the post is clearly much greater and simpler regarding the W_{post} and our previously proposed structure [73]. The band gap tuning rate is approximately 1 meV per nm in the t_{post} . In addition to the tunability, varying post lengths in the T-shaped structure are easier fabricated.

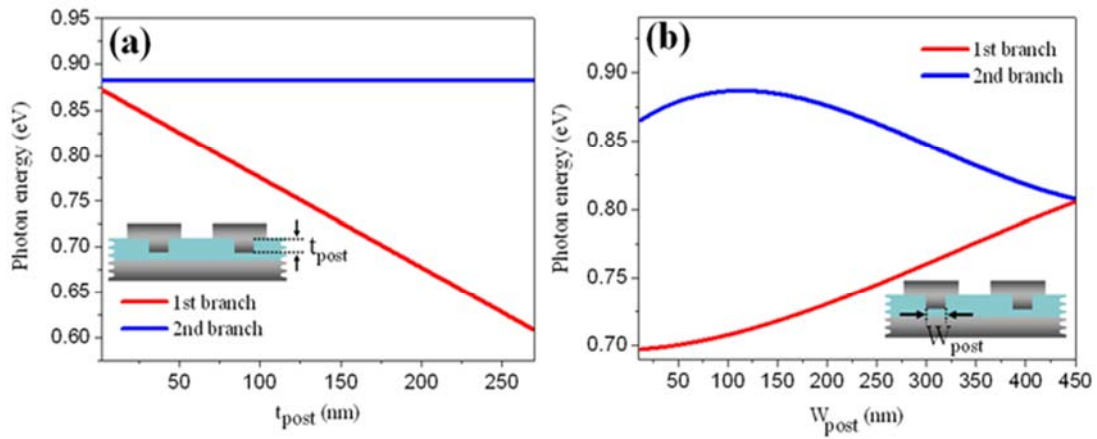


Fig. A-4. (a) Energy gap of the T-shaped structure varying with t_{post} when the W_{post} is fixed at 200 nm. (b) Energy gap versus W_{post} when the $t_{\text{post}} = 170$ nm.

Fabrication of the asymmetric T-shaped array

The fabrication processes of the structures are described as follows (see Figure A-5(a)). A 100 nm Ag film and a 320 nm SiO_2 layer were deposited on a silicon substrate using an electron gun evaporator and RF sputtering system. Then a PMMA layer as an e-beam resist was spin coated on the SiO_2 layer. The grating pattern with a lattice constant Λ_g and line spacing W_{post} was exposed with electron beam lithography, followed by a dry etching step with a mixture gas of $\text{CHF}_3/\text{O}_2/\text{Ar}$ in an inductively coupled plasma (ICP) system. (ICP recipe shown in Appendix C) After etching a

depth of t_{post} , an O_2 plasma ashing process in Appendix C was used for 6 seconds. A silver film was then evaporated on the surface with a thickness of t_{post} . After removing the residual PMMA, another PMMA periodic structure with a period Λ_g , line spacing W_{Top} , and displacement d was formed by the alignment in the second EBL. Finally, a 200-nm-thick silver film (t_{top}) was deposited, and the T-shaped structure was completed via a PMMA lift-off process.

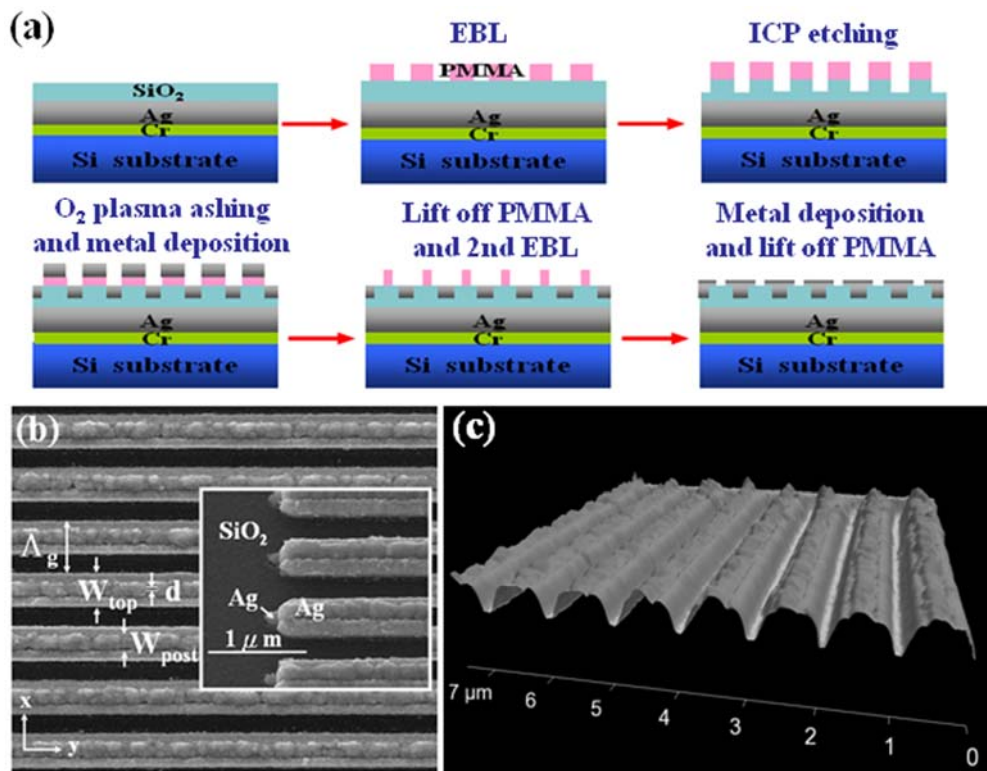


Fig. A-5 (a) The fabrication process of the T-shaped Ag/SiO₂/Ag structure. (b) SEM view of the T-shaped array with a displacement of $d=50$ nm. The inset shows the details of the structure with a tilt angle of 25° at the ends of the grating slabs on the Ag posts. (c) AFM image profile of the T-shaped grating.

Figure A-5(b) is the scanning electron microscope (SEM) image of the fabricated structure with a tilt angle of 25° , where a bump structure is on the top of the silver grating due to the imperfect nature of the fabrication process. Figure A-5(c) is the atomic force microscopy (AFM) image profile of the fabricated T-shaped grating.

Experimental results and discussion

To characterize the band structures varying with the t_{post} , the absorbance spectra under oblique incidence in x-z plane was measured using a FTIR spectrometer. The light source was focused on the sample that was placed on wedges with tilt angles θ_i during the FTIR measurements. The back-reflected light from the sample through a $50\mu\text{m}\times 50\mu\text{m}$ slit was collected and detected using a MCT (mercury-cadmium-telluride) photodetector with a spectral resolution of 2 cm^{-1} . In order to verify the bandstructure of the T-shaped grating from TM mode response (see Fig. A-2(b)), a near-infrared polarizer was used to select input light polarization. Figure A-6 exhibits the absorbance spectra for TE-, TM-, and un-polarized incident light. As can be seen, two pronounced absorption peaks occurs at $\lambda=1.41\mu\text{m}$ and $\lambda=1.85\mu\text{m}$ for both TM- and un-polarized cases, corresponding to the LSPP band gap, while there is no peak for the TE mode. The evidence clearly shows the band-gap feature originates from TM polarization. Due to the limitation of our current setup

with the polarizer, the absorbance spectra of the structures with two different t_{post} and incidence angles from 0° to 10° were also measured under un-polarized illumination.

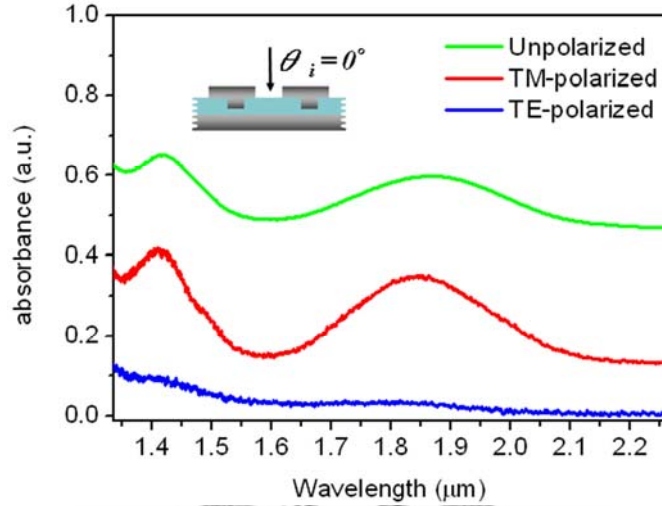
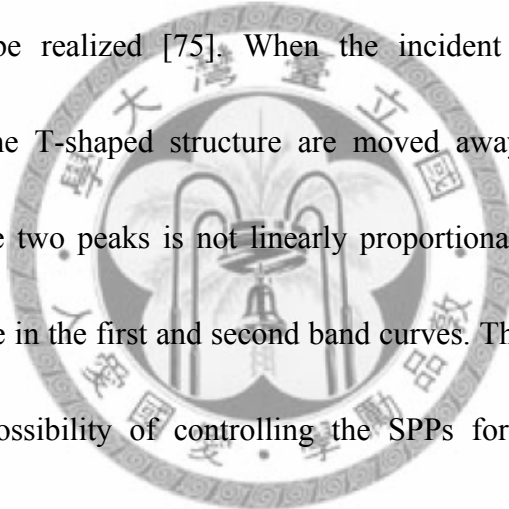


Fig. A-6 Experimental absorbance spectra of the T-shaped grating ($\Lambda_g=1 \mu\text{m}$, $W_{\text{top}}=620 \text{ nm}$, $t_{\text{top}}=200 \text{ nm}$, $W_{\text{post}}=200 \text{ nm}$, $t_{\text{post}}=170 \text{ nm}$, and $Gt=150 \text{ nm}$) at normal incidence under TE-, TM-, and un-polarized illumination.

Figure A-7(a) shows the absorbance spectra of the proposed structure when $t_{\text{post}} = 0 \text{ nm}$, and its simulation result. The results show that as θ_i increases, the resonance peak at $\lambda=1.43 \mu\text{m}$ at normal incidence is split into two, one peak is red-shifted and the other is blue-shifted, corresponding to the grating-coupled SPP at the bottom SiO_2/Ag interface. The distance difference between the two split peaks is linearly increased with an increasing incidence angle in the presence of a 3 % measurement error. The measured absorbance spectra of the T-shaped structure with $d=50 \text{ nm}$ and $t_{\text{post}}=170 \text{ nm}$ was also observed in Figure A-7(b). Two clear resonance peaks at

normal incidence are found at $\lambda=1.83\mu\text{m}$ for the first band and $\lambda=1.41\mu\text{m}$ for the second band, demonstrating an energy gap between them in accordance with our simulation. The width of the band gap is up to 420 nm, much larger than the 188 nm created by the silicon-loaded bihamonic metallic grating [72]. Because of the wider band gap occurring on the Bragg plane $k_x=0$ (incident angle $\theta_i = 0^\circ$), the structure is feasible for band gap defect cavities and band gap defect mode laser applications. Moreover, if the post t_{post} reaches 320 nm ($G_r=0$ nm), an angle-independent band-stop reflective filter can be realized [75]. When the incident angle increases, both resonance peaks of the T-shaped structure are moved away, and the wavelength difference between the two peaks is not linearly proportional to the incident angle. This indicates a change in the first and second band curves. Therefore, the band curve feature implies the possibility of controlling the SPPs for dielectric-loaded SPP waveguides. The propagation loss for the SPPs is mainly from the roughness of dielectric/metal interfaces and ohmic heating loss in the metal. To reduce the loss and extend the propagation length, much energy concentrated in the dielectric medium and smaller values of group velocity dispersion should be taken into account [76].



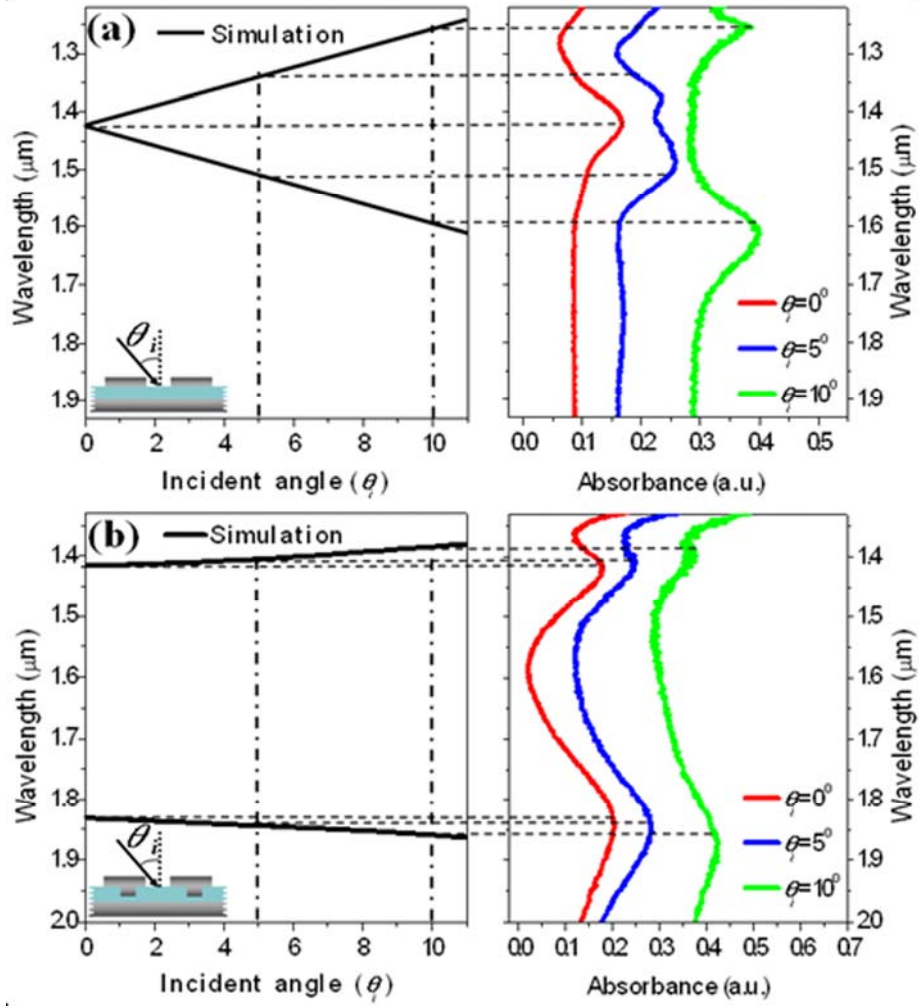


Fig. A-7 Experimental absorbance spectra of (a) the multilayer structure ($\Lambda_g=1 \mu\text{m}$, $W_{\text{top}}=570 \text{ nm}$, $t_{\text{top}}=200 \text{ nm}$, $W_{\text{post}}=200 \text{ nm}$, $t_{\text{post}}=0 \text{ nm}$, and $Gt=320 \text{ nm}$) and (b) the T-shaped structure ($\Lambda_g=1 \mu\text{m}$, $W_{\text{top}}=620 \text{ nm}$, $t_{\text{top}}=200 \text{ nm}$, $W_{\text{post}}=200 \text{ nm}$, $t_{\text{post}}=170 \text{ nm}$, and $Gt=150 \text{ nm}$) for the different incident angles $\theta_i = 0^\circ$, 5° , and 10° . In both (a) and (b), the simulated absorbance spectra are represented by black solid curves.

Because most of the field intensity of the SPP propagation is on the bottom SiO_2/Ag interface (see Figure A-3(a)), and the SPP effective index can be modified by different metallic slit widths, this study proposes a simple 1D photonic crystal slab to

qualitatively interpret the SPP band gap behavior. Figure A-8 shows the dispersion relation of the 1D photonic slab with a periodicity of $1\ \mu\text{m}$ and a SiO_2 thickness of $320\ \text{nm}$, where n_1 is the SiO_2 index and n_2 is a high-index in the W_{post} region. An energy gap at $k_x=0$ caused by the index contrast between the constituent dielectrics can be found in its dispersion relation, which behaves similarly to that shown in Figure A-2(b). Overall, these results substantially prove that the band curves and the band gap between the first and second bands can be engineered by varying the post depth. The unique properties of the T-shaped configuration can be applied to control the light localization and propagation at the dielectric/metal interface.

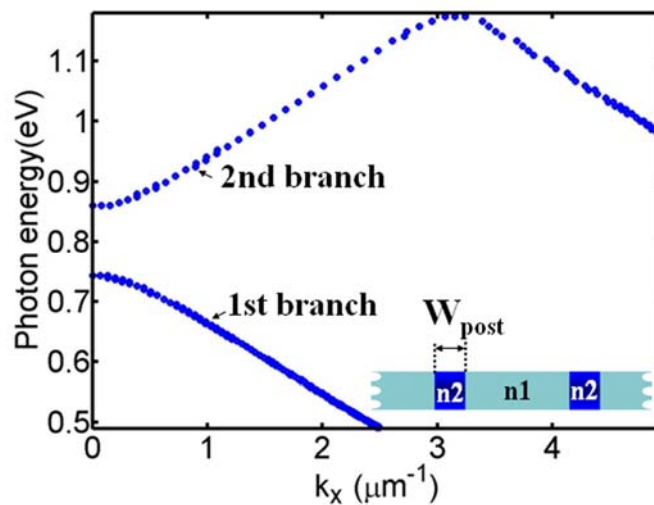
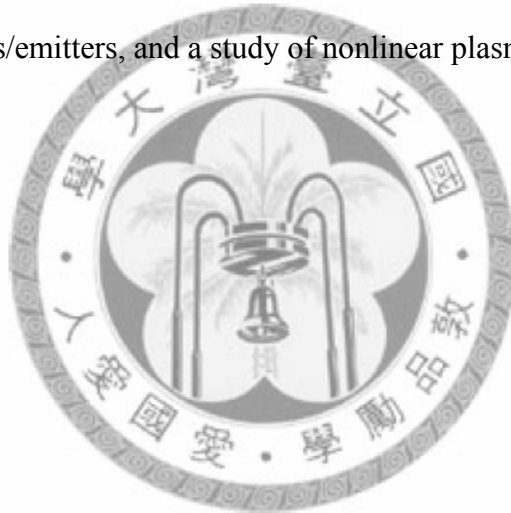


Fig. A-8 1D photonic dispersion curve of the slab with the constituent dielectrics $n_1=1.414$ and $n_2=2.236$, when $\Lambda_g=1\ \mu\text{m}$, $t_{\text{SiO}_2}=320\ \text{nm}$, and $W_{\text{post}}=200\ \text{nm}$.

Summary

In summary, this study demonstrated the localized surface plasmon-polariton band gap based on an Ag/ SiO_2 /Ag asymmetric T-shaped structure. The localized

surface plasmonic band gap was characterized with a measured absorbance spectra from the FTIR system. This band gap is attributed to the index contrast between the metal-metal and single metal regions, and is linearly proportional to the increased t_{post} ($t_{\text{post}} \leq 270$ nm). When the band gap opens, the shift of the first branch is much greater than that of the second branch because of the perturbed SPP mode of the first branch caused by the post. The plasmonic band gap structure suggests applications for plasmonic devices with LSPP band gap manipulations, such as band gap waveguides, and defect cavity lasers/emitters, and a study of nonlinear plasmonics.



Appendix B

Hydrodynamic modeling of surface plasmon enhanced photon induced current in a gold grating

We cooperated with professor Wan Kuang's group at Boise State University to study photon induced voltage on an Au grating slab [77]. A semi-classical electrodynamic model is developed for the Au grating slab under the weak nonlinearity approximation. The electrons in the conduction band are treated as an electron gas in the presence of the self-consistent electromagnetic field. The model was solved by finite element method and compared with our measurements. The calculated photon induced voltage as a function of incident angles and wavelengths was found to be in qualitatively agreement with the experimental measurements. The results show that increasing surface plasmon spatial variation enhances photon induced current.

Fundamental study of semi-classical electrodynamic model

Enhancement of optical properties by plasmon resonances in metallic materials has attracted much attention over the past two decades. Strong local fields from plasmon resonances are particularly important for nonlinear optical processes which scale with a high power of electromagnetic fields strength. A light beam with a frequency of ω can produce the photon induced current on metallic structures. The

overall shapes of the metallic structures play a significant role in determining the induced current response [78, 79]. In the chapter, we will introduce the hydrodynamic theory developed by Goff and Schaich [80] to qualitatively explain the response. Based on the model using the finite element method (FEM), the photon induced current on an Au grating slab is also investigated numerically.

The photon induced current can be treated by the Maxwell's equation with an explicit current density \vec{J} ,

$$\nabla \times \vec{H}(\vec{r}, t) = \epsilon_0 \frac{\partial \vec{E}(\vec{r}, t)}{\partial t} + \frac{\partial \vec{P}(\vec{r}, t)}{\partial t} + \vec{J}(\vec{r}, t) \quad (1)$$

where \vec{J} is the current density due to electron transport in metal. The electric field \vec{E} and polarization \vec{P} in Eq. (1) are written out separately because of numerical convenience. In the absence of interband transitions, the electrons in the conduction band can be treated as an electron gas with an effective mass m^* in the presence of the self-consistent fields \vec{E} and \vec{H} [81]. The hydrodynamic equation of motion for the average velocity $\vec{v}(\vec{r}, t)$ is given by,

$$\frac{\partial \vec{j}}{\partial t} + \vec{v}(\nabla \cdot \vec{j}) + (\vec{j} \cdot \nabla) \vec{v} = \frac{e}{m^*} (n \vec{E} + \vec{j} \times \vec{B}) - \frac{\nabla p}{m^*} - \frac{\vec{j}}{\tau_m} \quad (2)$$

where $\vec{j}(\vec{r}, t)$ is electron flux density which related to electron number density n multiplied by the average velocity (ie $\vec{j} = n \vec{v}$), and pressure p is attributed to quantum mechanical Coulomb correlations and exchange contribution. A

phenomenological decay time τ_m is employed to describe other Coulomb scattering.

To simplify and calculate the nonlinear current density $\vec{j}(\vec{r}, t)$, we ignore the influence of the magnetic field \vec{B} and expand the variables in Eq. (2) as a series of orders where $A(\vec{r}, t) = A_0(\vec{r}) + \tilde{A}_1(\vec{r})e^{i\omega t} + \tilde{A}_2(\vec{r})e^{i2\omega t} + \dots + c.c.$. $\vec{A}(\vec{r}, t)$ can be either \vec{E} , n , v or p . A_0 is the equilibrium value of the variable and A_i are complex values.

For electron flux density \vec{j} , it is important in obtaining the following series equation

$$\vec{j}(\vec{r}, t) = \vec{j}_0(\vec{r}) + \vec{j}_v(\vec{r}) + \tilde{j}_1(\vec{r})e^{i\omega t} + \tilde{j}_2(\vec{r})e^{i2\omega t} + \dots + c.c. \quad (3)$$

Here, we assume $\vec{j}_0(\vec{r}) = 0$ because of no external field or voltage applied to the devices. Substituting Eq. (3) and the expansions in \vec{E} , n , and p to Eq. (2), it can generate a sequence of equations of fixed order terms. For the second harmonic term, we can obtain the following equation:

$$i2\omega \tilde{j}_2 + [(\nabla \cdot \vec{j}) \vec{v} + (\vec{j} \cdot \nabla) \vec{v}]_2 = \frac{e}{m^*} [n\vec{E}]_2 + \left[\frac{\vec{j}}{\tau_m} \right]_2 - \frac{\nabla \tilde{p}_2}{m^*} \quad (4)$$

where $[(\nabla \cdot \vec{j}) \vec{v} + (\vec{j} \cdot \nabla) \vec{v}]_2$, $[n\vec{E}]_2$, $\left[\frac{\vec{j}}{\tau_m} \right]_2$ are short-hand expressions for the second order terms. It should be noted that this second order term include both DC and second harmonic 2ω components. This inclusion of DC and second harmonic components can be observed by the simple expansion of the second order term:

$$\begin{aligned} [(\nabla \cdot \vec{j}) \vec{v} + (\vec{j} \cdot \nabla) \vec{v}]_2 &= (\nabla \cdot \tilde{j}_1) \tilde{v}_1 + (\tilde{j}_1 \cdot \nabla) \tilde{v}_1 + (\nabla \cdot \tilde{j}_1^*) \tilde{v}_1^* + (\tilde{j}_1^* \cdot \nabla) \tilde{v}_1^* \\ &\quad + (\nabla \cdot \tilde{j}_1) \tilde{v}_1^* + (\tilde{j}_1 \cdot \nabla) \tilde{v}_1^* + (\nabla \cdot \tilde{j}_1^*) \tilde{v}_1 + (\tilde{j}_1^* \cdot \nabla) \tilde{v}_1 \end{aligned} \quad (5)$$

The first two terms on the right-hand-side has the frequency of 2ω and the last two terms are DC components.

The electron pressure p described by a Thomas-Fermi statistic is assumed to be

$$p(\bar{r}, t) = \zeta n^{5/3}(\bar{r}, t) = \zeta n_0^{5/3} + \frac{5}{3} \zeta n_0^{2/3} (\tilde{n}_1 e^{i\omega t} + \tilde{n}_2 e^{i2\omega t} + \dots + c.c.) + \frac{5}{9} \zeta n_0^{-1/3} (\tilde{n}_1^2 e^{i2\omega t} + 2\tilde{n}_1 \tilde{n}_1^* + \dots + c.c.) + \dots \quad (6)$$

where $|\tilde{n}_2| \ll |\tilde{n}_1| \ll n_0$ and $\zeta = \frac{9}{25} m^* n_0^{-2/3} v_{F,0}^2$. The $v_{F,0}$ is called Fermi velocity.

Equation (6) also shows that the change of electron density, n_1 , can lead to another DC component of the electron pressure which contributes to the photon induced current \bar{j}_v . The DC component is given by $p_v = \frac{10}{9} \zeta n_0^{-1/3} |\tilde{n}_1|^2$. With the p_v , DC components in Eq. (5), and the \bar{j} expression in Eq. (3), the photon induced electron flux \bar{j}_v derived from Eq. (2) becomes

$$\begin{aligned} \frac{\bar{j}_v}{\tau_m} + (\nabla \cdot \tilde{j}_1) \tilde{v}_1^* + (\tilde{j}_1 \cdot \nabla) \tilde{v}_1^* + (\nabla \cdot \tilde{j}_1^*) \tilde{v}_1 + (\tilde{j}_1^* \cdot \nabla) \tilde{v}_1 \\ = \frac{e}{m^*} (\tilde{n}_1 \tilde{E}_1^* + \tilde{n}_1^* \tilde{E}_1) - \frac{10\zeta}{9m^*} \nabla |\tilde{n}_1|^2 \end{aligned} \quad (7)$$

The Eq. (7) can be rewritten as

$$\bar{j}_v = 2 \operatorname{Re} \left[\frac{e\tau_m}{m^*} (\tilde{n}_1 \tilde{E}_1^* - \tau_m (\nabla \cdot \tilde{j}_1) \tilde{v}_1^* - \tau_m (\tilde{j}_1 \cdot \nabla) \tilde{v}_1^*) \right] - \frac{10\tau_m \zeta}{9m^*} \nabla |\tilde{n}_1|^2 \quad (8)$$

where $\operatorname{Re}[\]$ denotes the real part of the expression. Through the Eq. (8), it is clearly shown that the photon induced current is not only determined by the internal

parameters ($m^* \tau_m \tilde{n}_1 \zeta$) and external field, but also affected by the spatial distribution of \tilde{j}_1 which correlates closely with the geometry of metallic device structures.

Eq. (8) was solved by finite element method using a commercial software, COMSOL, in the general equation mode. Considering a 50nm-thick Au grating on a fused silica substrate, the grating has a periodicity of 1.22 μm and a line width of 790nm. The simulation part was collaborated with professor Wan Kuang's group.

Figure B-1 shows the photon induced current density of the grating structure as a function of incident angle and wavelength simulated by the hydrodynamic model. The white open circles indicates the position of peak response for a given incident wavelength.

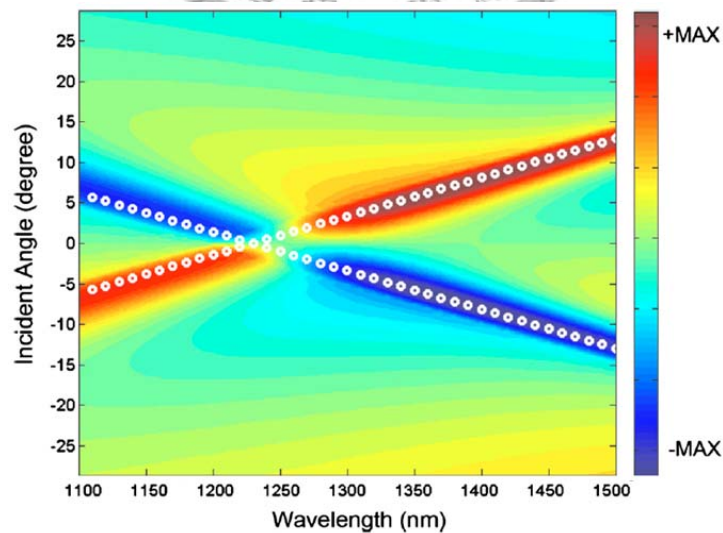


Fig. B-1 Photon induced current density as calculated by the hydrodynamic model where the white open circles indicate the position of peak response.

Fabrication of the Au grating slab

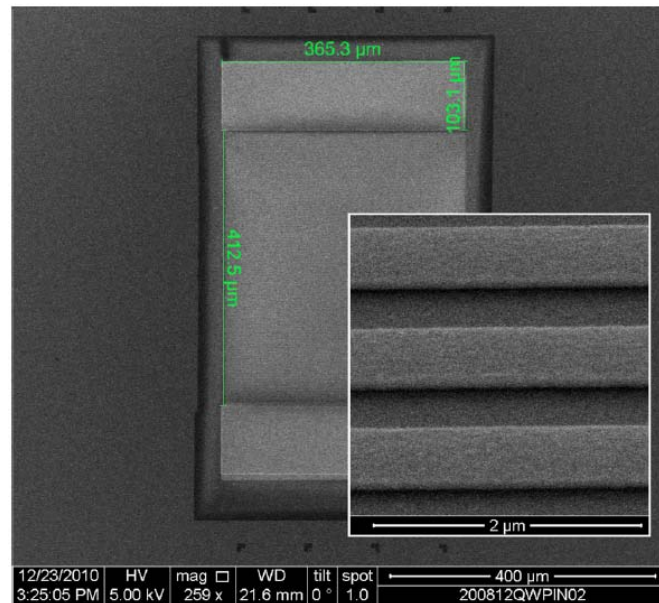


Fig. B-2 SEM image of an Au grating. The inset shows the details of the grating.

The Au grating structure was fabricated on a silica substrate. A 50 nm Ag film and a 5nm Cr adhesion layer were evaporated on the substrate. A PMMA layer was coated on the Au surface. The structure with a lattice constant (Λ) of 1.2μm and a line spacing of 430nm (W) was then defined on the PMMA layer by electron beam lithography. The pattern was transferred to Cr layer by an ion beam etching (IBE) system with an etching time of 17sec (IBE recipe shown in Appendix C). After the sample cleanup with the resist remover PV-218, photolithography was applied with a photo mask used to electrically isolate from the surrounding Au film. The second IBE was executed for 40 sec to transfer the mask pattern from the photoresist layer to the silica substrate. The photoresist residue was then cleaned by acetone, isopropyl

alcohol and deionized water, respectively. To make the electrical contacts on the Au grating, the second time photolithography was used with the contacts defined both ends of the grating slab. Finally, a 200nm Au layer was deposited and the Au grating structure was obtained via a photoresist lift-off process. Figure B-2 is the image of the fabricated grating slab with a tilt angle of 35°.

Experimental results and discussion

The incident light source was produced from an optical parametric oscillator pumped by a frequency-tripled Q-switched YAG laser whose wavelength was varied from 1000 to 1600 nm in the measurements. The electrical contacts on the sample were wire-bounded to SMA connectors. The induced voltage from the sample was fed to a 350 MHz preamplifier (Stanford Research System, SR445A) and measured by a 4 GHz digital storage oscilloscope (Agilent, Infinium 83000) triggered by the Q-switch of the laser. The laser beam was focused at the sample surface with a beam size of approximately 0.3 mm. The polarization of the incidence was maintained TM-polarized for all measurements. The induced voltage was measured as a function of incident angle and wavelength.

Figure B-3 shows the peak response from the Au grating slab as a function of incident angle and wavelength. The direction of induced current reverses when the incident angle changes sign. This behavior is consistent with centro-symmetric

structure. The peaks occurring between $\pm 15^\circ$ are the result of surface plasmon resonance at the air and Au interface. The propagation constant for surface plasmon at the air and Au interface can be approximately given by

$$k_{SP} = k_0 \sqrt{\frac{\epsilon_m}{1 + \epsilon_m}}$$

where ϵ_m is the dielectric constant of Au. The condition at which surface plasmons are excited for a given incident wavelength is therefore depends on the diffraction order, m , of the grating as $k_{SP} = k_0 \sin \theta + 2m\pi/a$, where the grating periodicity $a = 1.2 \mu\text{m}$. At the incident wavelength of 1200 nm and 1300 nm, the surface plasmon resonance is excited by diffraction order -1 and 1 , respectively. The polarity of photon induced voltage is expected to be reversed. Additional peaks at incident angles larger than 15° is due to surface plasmon excitation at Au and substrate interface. To compare the measurement with the theoretical model, the photon induced voltage on the Au grating slab was measured from 1100 nm to 1500 nm at an interval of 50 nm and from 0° to 30° incidence at an interval of 1° . Figure B-4 shows the photon induced voltage as a function of incident angle and wavelength. The step-like appearance of the plot is due to the limited wavelength samples. This result is compared with its simulation as shown Figure B-1. The agreement between the hydrodynamic model and the measurement can be observed. However, calculated response at larger incident angles

is found to be slightly different from the measurement result. The difference is probably due to the efficiency of the surface plasmon excitation increased by surface roughness at the Au and substrate interface.

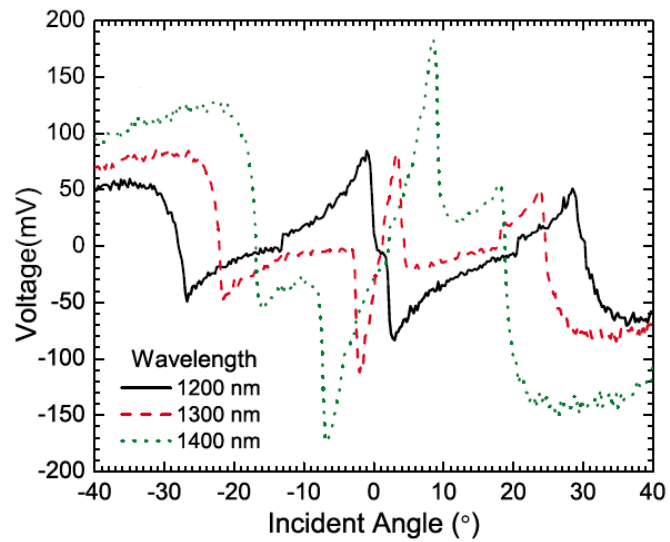


Fig. B-3 Induced voltage peaks as a function of incident angle for incident wavelengths of 1.2, 1.3, and 1.4 μ m.

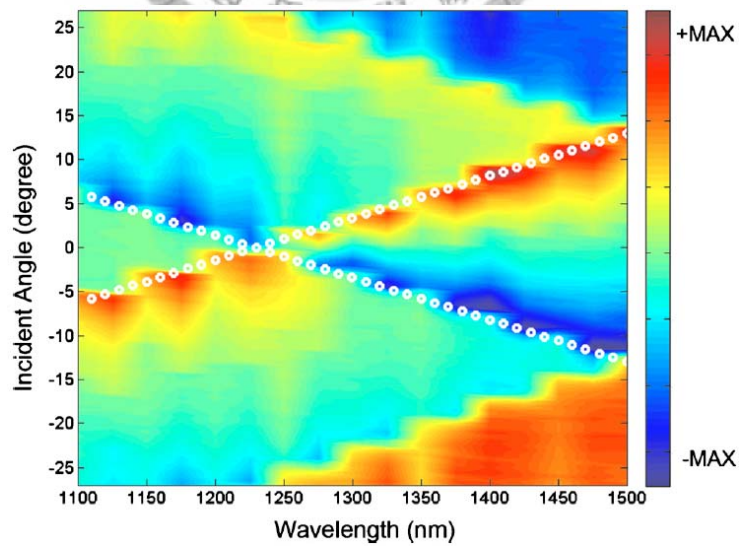


Fig. B-4 Measured photon induced voltage as a function of incident angle and wavelength.

Summary

The photon induced current on an Au grating slab is investigated numerically and experimentally. The calculated photon induced voltage based on the semi-classical electrodynamic model as a function of incident angles and wavelengths is found to be in qualitative agreement with the experimental measurements. The nonlinear electron transport over the structured grating surface is accounted for in this model. It provides a pathway for the study of devices with more detailed photon electron interactions.



Appendix C

<i>E-gun evaporation of Au/Ag films</i>						
Metals	Density (gm/cm ³)	Impedance (×10 ⁵ .gm/cm ² .sec)	Pressure (×10 ⁻⁶ Torr)	Current (A)	Temperature (°C)	Deposition rate (A/sec)
Au	19.38	23.18	~9.5	100~110	<70 °C	1 A/sec
Ag	10.5	16.69	~4.5	48~55	<70 °C	1 A/sec

* 7 cc crucible used for target materials AST Peva-400E evaporator at RCAS

<i>Dry etching of Au/Ag films</i>									
	Gas (sccm)	Power (W)	Pressure (mTorr)	Strike pressure (mTorr)	Ramp rate (mTorr/cycle)	Reflected power (W)	DC bias (V)	Cooling temperature (°C)	Etching rate (nm/min)
RIE	Ar:40	290	10	50	10	0	590-600	18	Au: 33 Ag: 35

OXFORD Plasmalab 80 plus REI system at RCAS

	Gas (sccm)	Pressure (×10 ⁻⁴ Torr)	Neutralized emission current (A)	Accelerator	Beam	Discharge	Cathode current (A)	Filament current (A)	Etching rate (nm/min)
IBE	Ar:1.5	1.7	61	Current: 4A Voltage: 800V	Current: 54mA Voltage: 750V	Current: 2.21A Voltage: 38V	4.22	4.25	Au: 228 Ag: 180

高教, KD-Ion Etch at ANPL

<i>SiO₂ layer deposition</i>							
	Density (gm/cm ³)	Impedance (×10 ⁵ .gm/cm ² .sec)	Pressure (pa)	Power (W)	Gas (sccm)	DC bias (V)	Deposition rate (nm/min)
RF sputtering	2.2	8.250	0.8	100	Ar:30	492	7.8

RF-sputter ULVAC at RCAS

	Pressure (mTorr)	Power (W)	Gas (sccm)	Table temperature (°C)	Deposition rate (nm/min)
PECVD	900	25	SiH ₄ : 10 N ₂ O: 830	492	56

OXFORD plasmalab 80 plus at NDL

Dry etching of SiO₂ layer

	Gas (sccm)	RF power (W)	ICP power (W)	Pressure (mTorr)	Strike pressure (mTorr)	Ramp rate (mTorr/cycle)	Reflected power (W)	DC bias (V)	Cooling temperature (°C)	Etching rate (nm/min)
ICP	O ₂ : 2 CHF ₃ : 20	150	0	55	0	0	0	386-422	20	47

OXFORD plasmalab system 100 at ITRI

	Gas (sccm)	Power (W)	Pressure (Pa)	Reflected power (W)	DC bias (V)	Cooling temperature (°C)	Etching rate (nm/min)
ICP	O ₂ : 2 Ar: 5 CHF ₃ : 20	100	0.6	0	20	20	46

Samco, RIE-10iP at RCAS

O₂ plasma ashing

	Gas (sccm)	Power (W)	Pressure (Pa)	DC bias (V)	Cooling temperature (°C)	PMMA Etching rate (nm/min)
ICP	O ₂ : 2	100	0.6	20	20	37

Samco, RIE-10iP at RCAS

Bibliography

1. R. W. Wood, "On a Remarkable Case of Uneven Distribution of Light in a Diffraction Grating Spectrum," Proc. Phys. Soc. London **18** (1902).
2. J. C. M. Garnett, "Colours in Metal Glasses and in Metallic Films," Phil. Trans. R. Soc. London **A203**, 385-420 (1904).
3. J. W. Strutt, "On the Light from the Sky, its Polarization and Colour," Philos. Mag. **41**, 107-120, 274-279 (1871).
4. G. Mie, "Beiträge zur Optik trüber Medien, speziell kolloidaler Metallösungen," Leipzig, Ann. Phys. **330**, 377- 445 (1908).
5. D. Pines, "Collective energy losses in solids," Rev. Mod. Phys. **28**, 184-199 (1956).
6. R. H. Ritchie, "Plasma Losses by Fast Electrons in Thin Films," Phys. Rev. **106**, 874–881 (1957).
7. A. Otto, "Excitation of Non-Radiative Surface Plasma Waves in Silver by the Method of Frustrated Total Reflection," Z. Phys. **216**, 398 (1968).
8. E. Kretschmann, and H. Raether, "Radiative Decay of Non-Radiative Surface Plasmons Excited by Light," Z. Phys. **239**, 2135 (1968).
9. U. Kreibig, and P. Zacharias, "Surface Plasma Resonances in Small Spherical Silver and Gold Particles," Zeitschrift Für Physik **231**, 128-143 (1970).
10. S. I. Bozhevolnyi, J. Erland, K. Leosson, P. M. Skovgaard, and J. M. Hvam, "Waveguiding in Surface Plasmon Polariton Band Gap Structures," Phys. Rev. Lett. **86** (2001).
11. V. Mikhailov, G. A. Wurtz, J. Elliott, P. Bayvel, and A. V. Zayats, "Dispersing light with surface plasmon polaritonic crystals," Phys. Rev. Lett. **99**, 083901 (2007).
12. M. Fleischmann, P. J. Hendra, and A. J. McQuillan, "Raman spectra of pyridine adsorbed at a silver electrode," Chem. Phys. Lett. **26**, 163–166 (1974).
13. J. N. Anker, W. P. Hall, O. Lyandres, N. C. Shah, J. Zhao, and R. P. V. Duyne, "Biosensing with plasmonic nanosensors " Nat. Mater. **7**, 442 - 453 (2008).
14. E. Cubukcu, S. Zhang, Y.-S. Park, G. Bartal, and X. Zhang, "Split ring resonator sensors for infrared detection of single molecular monolayers " Appl. Phys. Lett. **95**, 043113 (2009).
15. T. W. Ebbesen, H. J. Lezec, H. F. Ghaemi, T. Thio, and P. A. Wolff, "Extraordinary optical transmission through sub-wavelength hole arrays," Nature **391**, 667-669 (1998).
16. N. Fang, H. Lee, C. Sun, and X. Zhang, "Sub-Diffraction-Limited Optical Imaging with a Silver Superlens," Science **308**, 534-537 (2005).
17. A. Hohenau, J. R. Krenn, A. L. Stepanov, A. Drezet, H. Ditlbacher, B.

Steinberger, A. Leitner, and F. R. Aussenegg, "Dielectric optical elements for surface plasmons," *Opt. Lett.* **30**, 893-895 (2005).

18. T.-B. Wang, X.-W. Wen, C.-P. Yin, and H.-Z. Wang, "The transmission characteristics of surface plasmon polaritons in ring resonator," *Opt. Express* **17**, 24096-24101 (2009).

19. B. Min, E. Ostby, V. Sorger, E. Ulin-Avila, L. Yang, X. Zhang, and K. Vahala, "High-Q surface-plasmon-polariton whispering-gallery microcavity," *Nature* **457**, 455-458 (2009).

20. C. M. Wang, Y. C. Chang, M. W. Tsai, Y. H. Ye, C. Y. Chen, Y. W. Jiang, S. C. Lee, and D. P. Tsai, "Angular independent infrared filter assisted by localized surface plasmon polariton," *IEEE Photon. Tech. Lett.* **20** (2008).

21. C.-W. Cheng, M. N. Abbas, Z.-C. Chang, M. H. Shih, C. M. Wang, M. C. Wu, and Y.-C. Chang, "Angle-independent plasmonic infrared band-stop reflective filter based on the Ag/SiO₂/Ag T-shaped array," *Opt. Lett.* **36**, 1440-1442 (2011).

22. Z. H. Jiang, S. Yun, F. Toor, D. H. Werner, and T. S. Mayer, "Conformal Dual-Band Near-Perfectly Absorbing Mid-Infrared Metamaterial Coating," *ACS Nano* **5**, 4641-4647 (2011).

23. F. J. Beck, A. Polman, and K. R. Catchpole, "Tunable light trapping for solar cells using localized surface plasmons," *J. Appl. Phys.* **105**, 114310 (2009).

24. K. B. Alici, and E. Ozbay, "Photonic metamaterial absorber designs for infrared solar cell applications," *Proc. of SPIE* **7772**, 77721B-77721B-77723 (2011).

25. V. E. Ferry, J. N. Munday, and H. A. Atwater, "Design Considerations for Plasmonic Photovoltaics " *Adv. Mater.* **22**, 4794-4808 (2010).

26. K. Nakayama, K. Tanabe, and H. A. Atwater, "Plasmonic nanoparticle enhanced light absorption in GaAs solar cells " *Appl. Phys. Lett.* **93**, 121904 (2008).

27. M. A. Noginov, G. Zhu, A. M. Belgrave, R. Bakker, V. M. Shalaev, S. Stout, E. Herz, T. Suteewong, and U. Wiesner, "Demonstration of a spaser-based nanolaser," *Nature* **460**, 1110-1112 (2009).

28. Y. H. Ye, Y. W. Jiang, M. W. Tsai, Y. T. Chang, C. Y. Chen, D. C. Tzuang, Y. T. Wu, and S. C. Lee, "Localized surface plasmon polaritons in Ag/SiO₂/Ag plasmonic thermal emitter," *Appl. Phys. Lett.* **93**, 033113 (2008).

29. Y. T. Chang, Y. H. Ye, D. C. Tzuang, Y. T. Wu, C. H. Yang, C. F. Chan, Y. W. Jiang, and S. C. Lee, "Localized surface plasmons in Al/Si structure and Ag/SiO₂/Ag emitter with different concentric metal rings," *Appl. Phys. Lett.* **92**, 233109 (2008).

30. Y. C. Chang, C. M. Wang, M. N. Abbas, M. H. Shih, and D. P. Tsai, "T-shaped plasmonic array as a narrow-band thermal emitter or biosensor," *Opt. Express* **17**, 13526-13531 (2009).

31. M. N. Abbas, C.-W. Cheng, Y.-C. Chang, M.-H. Shih, H.-H. Chen, and S.-C. Lee,

"Angle and polarization independent narrow-band thermal emitter made of metallic disk on SiO₂," *Appl. Phys. Lett.* **98**, 121116 (2011).

32. T. J. Coutts, "A review of progress in thermophotovoltaic generation of electricity," *Renewable and Sustainable Energy Rev.* **3**, 77 (1999).

33. M. Laroche, R. Carminati, and J.-J. Greffet, "Near-field thermophotovoltaic energy conversion " *J. Appl. Phys.* **100**, 063704 (2006).

34. C.-W. Cheng, M. N. Abbas, C.-W. Chiu, K.-T. Lai, M.-H. Shih, and Y.-C. Chang, "Wide-angle polarization independent infrared broadband absorbers based on metallic multi-sized disk arrays," *Opt. Express* **20**, 10376-10381 (2012).

35. W. L. Barnes, Alain Dereux, and T. W. Ebbesen, "Surface plasmon subwavelength optics," *Nature*, 824-830 (2003).

36. J. D. Jackson, *Classical Electrodynamics* (John Wiley & Sons, Inc, 1998).

37. A. V. Zayats, and I. I. Smolyaninov, "Near-field photonics: surface plasmon polaritons and localized surface plasmons," *J. Opt. A: Pure Appl. Opt.* **5**, S16-S50 (2003).

38. S. A. Maier, *Plasmonics: Fundamentals and Applications* (Springer, 2007).

39. H. Raether, *Surface Plasmons on Smooth and Rough Surface and on Gratings* (Springer, 1988).

40. 邱國斌, and 蔡定平, "金屬表面電漿簡介," *物理雙月刊* **28**, 472-485 (2006).

41. S. Bozhevolnyi, *Plasmonic Nanoguides and Circuits* (Pan Stanford Publishing, 2008).

42. C. F. Bohren, and D. R. Huffman, *Absorption and Scattering of Light by Small Particles* (John Wiley & Sons, Inc, 1998).

43. S. Kawata, *Near-field optics and surface plasmon polaritons* (Springer, 2001).

44. M. Born, and E. Wolf, *Principles of Optics* (Cambridge University Press, 1999).

45. H. C. v. d. Hulst, *Light scattering by small particles* (Dover publication Inc., 1957).

46. H. T. Miyazaki, and Y. Kurokawa, "Controlled plasmon resonance in closed metal/insulator/metal nanocavities " *Appl. Phys. Lett.* **89**, 211126 (2006).

47. M. N. Abbas, "Plasmonic nanostructure for photonic integrated circuit," in *Engineering and System Science*(National Tsing Hua University, Hsinchu, 2011).

48. M. G. Moharam, E. B. Grann, D. A. Pommet, and T. K. Gaylord, "Formulation for stable and efficient implementation of the rigorous coupled-wave analysis of binary gratings," *JOSA A* **12**, 1068-1076 (1995).

49. M. G. Moharam, D. A. Pommet, E. B. Grann, and T. K. Gaylord, "Stable implementation of the rigorous coupled-wave analysis for surface-relief gratings: enhanced transmittance matrix approach," *JOSA A* **12**, 1077-1086 (1995).

50. L. Li, "Use of Fourier series in the analysis of discontinuous periodic structures,"

JOSA A **13**, 1870-1876 (1996).

51. E. D. Palik, *Handbook of Optical Constants of Solids* (Academic, Boston, 1985).
52. R. Siegel, and J. Howell, *Thermal Radiation Heat Transfer* (Hemisphere Publishing Corporation, New York, 1981).
53. M.-W. Tsai, "Transmission properties of periodic metal/dielectric hole array and its application to narrow bandwidth infrared thermal emitter," in *Electronics Engineering*(National Taiwan University, Taipei, 2007).
54. D. L. Brundrett, E. N. Glytsis, and T. K. Gaylord, "Normal-incidence guided-mode resonant grating filters: design and experimental demonstration," *Opt. Lett.* **23**, 700-702 (1998).
55. F. Lemarchand, A. Sentenac, and H. Giovannini, "Increasing the angular tolerance of resonant grating filters with doubly periodic structures," *Opt. Lett.* **23**, 1149-1151 (1998).
56. A.-L. Fehrembach, A. Talneau, O. Boyko, F. Lemarchand, and A. Sentenac, "Experimental demonstration of a narrowband, angular tolerant, polarization independent, doubly periodic resonant grating filter," *Opt. Lett.* **32**, 2269-2271 (2007).
57. Z. Wu, J. W. Haus, Q. Zhan, and R. L. Nelson, "Plasmonic Notch Filter Design Based on Long-range Surface Plasmon Excitation Along Metal Grating " *Plasmonics* **3**, 103-108 (2008).
58. C. M. Wang, Y. C. Chang, M. W. Tsai, Y. H. Ye, C. Y. Chen, Y. W. Jiang, S. C. Lee, and D. P. Tsai, "Angle-Independent Infrared Filter Assisted by Localized Surface Plasmon Polariton," *IEEE Photon. Tech. Lett.* **20**, 1103-1105 (2008).
59. N. Liu, M. Mesch, T. Weiss, M. Hentschel, and H. Giessen, "Infrared Perfect Absorber and Its Application As Plasmonic Sensor," *Nano Lett.* **10**, 2342-2348 (2010).
60. M. Pu, C. Hu, M. Wang, C. Huang, Z. Zhao, C. Wang, Q. Feng, and X. Luo, "Design principles for infrared wide-angle perfect absorber based on plasmonic structure," *Opt. Express* **19**, 17413-17420 (2011).
61. E. D. Palik, *Handbook of Optical Constants of Solids* (Academic Press, Boston, 1985).
62. H. T. Miyazaki, and Y. Kurokawa, "Controlled plasmon resonance in closed metal/insulator/metal nanocavities," *Appl. Phys. Lett.* **89**, 211126 (2006).
63. R. Gordon, "Light in a subwavelength slit in a metal: Propagation and reflection," *Phys. Rev. B* **73**, 153405 (2006).
64. S. Collin, F. Pardo, and J.-L. Pelouard, "Waveguiding in nanoscale metallic apertures," *Opt. Express* **15**, 4310-4320 (2007).
65. X. Liu, T. Tyler, T. Starr, A. F. Starr, N. M. Jokerst, and W. J. Padilla, "Taming the Blackbody with Infrared Metamaterials as Selective Thermal Emitters," *Phys. Rev.*

Lett. **107**, 045901 (2011).

66. D. F. Swinehart, "The Beer-Lambert Law," J. Chem. Educ. **39**, 333-335 (1962).
67. V. E. Ferry, L. A. Sweatlock, D. Pacifici, and H. A. Atwater, "Plasmonic nanostructure design for efficient light coupling into solar cells," Nano Lett. **8**, 4391–4397 (2008).
68. J. B. Young, H. A. Graham, and E. W. Peterson, "Wire Grid Infrared Polarizer," Appl. Opt. **4**, 1023-1026 (1965).
69. C.-Y. Tsai, S.-P. Lu, J.-W. Lin, and P.-T. Lee, "High sensitivity plasmonic index sensor using slablike gold nanoring arrays " Appl. Phys. Lett. **98**, 153108 (2011).
70. C.-W. Cheng, M. N. Abbas, M.-H. Shih, and Y.-C. Chang, "Characterization of the surface plasmon polariton band gap in an Ag/SiO₂/Ag T-shaped periodical structure," Opt. Express **19**, 23698-23705 (2011).
71. W. L. Barnes, T. W. Preist, S. C. Kitson, and J. R. Sambles, "Physical origin of photonic energy gaps in the propagation of surface plasmons on gratings," Phys. Rev. B **54**, 6227-6244 (1996).
72. A. Kocabas, S. S. Senlik, and A. Aydinli, "Plasmonic band gap cavities on biharmonic gratings," Phys. Rev. B **77**, 195130 (2008).
73. M. N. Abbas, Y.-C. Chang, and M. H. Shih, "Plasmon-polariton band structures of asymmetric T-shaped plasmonic gratings," Opt. Express **18**, 2509-2514 (2010).
74. Y. Todorov, L. Tosetto, J. Teissier, A. M. Andrews, P. Klang, R. Colombelli, I. Sagnes, G. Strasser, and C. Sirtori, "Optical properties of metal-dielectric-metal microcavities in the THz frequency range," Opt. Express **18**, 13886-13906 (2010).
75. C.-W. Cheng, M. N. Abbas, Z.-C. Chang, M. H. Shih, C.-M. Wang, M. C. Wu, and Y.-C. Chang, "Angle-independent plasmonic infrared band-stop reflective filter based on the Ag/SiO₂/Ag T-shaped array," Opt. Lett. **36**, 1440 (2011).
76. B. Han, and C. Jiang, "Plasmonic slow light waveguide and cavity," Appl. Phys. B **95**, 97-103 (2009).
77. A. English, C.-W. Cheng, L. L. II, M.-H. Shih, and W. Kuang, "Hydrodynamic modeling of surface plasmon enhanced photon induced current in a gold grating," Appl. Phys. Lett. **98**, 191113 (2011).
78. N. Feth, S. Linden, M. W. Klein, M. Decker, F. B. P. Niesler, Y. Zeng, W. Hoyer, J. Liu, S. W. Koch, J. V. Moloney, and M. Wegener, "Second-harmonic generation from complementary split-ring resonators," Opt. Lett. **33**, 1975–1977 (2008).
79. Y. Zeng, W. Hoyer, J. Liu, S. W. Koch, and J. V. Moloney, "Classical theory for second-harmonic generation from metallic nanoparticles," Phys. Rev. B **79**, 235109 (2009).
80. J. E. Goff, and W. L. Schaich, "Hydrodynamic theory of photon drag," Phys. Rev. B **56**, 15421 (1997).

81. N. Bloembergen, R. K. Chang, S. S. Jha, and C. H. Lee, "Optical Second-Harmonic Generation in Reflection from Media with Inversion Symmetry," Phys. Rev. **174**, 813 (1968).



鄭程文

Cheng-Wen Cheng

Department of Physics, National Taiwan University,
No 1, Sec. 4, Roosevelt Rd.,
Taipei 10617, Taiwan, ROC.

■ **Journal papers**

- [1] Ngoc Luong, Cheng-Wen Cheng, Min-Hsiung Shih, Elton Graugnard, and Wan Kuang*, “Phase matching for surface plasmon enhanced second harmonic generation in a gold grating slab,” Appl. Phys. Lett. **100**, 181107 (2012)
(5-year IF=3.863; Ranking: 15/118 = 13% in Physics, Applied)
- [2] Cheng-Wen Cheng, Mohammed Nadhim Abbas, Chao-Wei Chiu, Kun-Ting Lai, Min-Hsiung Shih*, and Yia-Chung Chang, “Wide-angle polarization independent infrared broadband absorbers based on metallic multi-sized disk arrays,” Opt. Express **20**, 10376-10381 (2012)
(5-year IF=3.939; Ranking: 3/78 = 4% in Optics)
- [3] Cheng-Wen Cheng, Mohammed Nadhim Abbas, Min-Hsiung Shih*, and Yia-Chung Chang, “Characterization of the surface plasmon polariton band gap in an Ag/SiO₂/Ag T-shaped periodical structure,” Opt. Express **19**, 23698-23705 (2011)
(5-year IF=3.939; Ranking: 3/78 = 4% in Optics)
- [4] Alex English, Cheng-Wen Cheng, Lloyd Lowe II, Min-Hsiung Shih and Wan Kuang*, “Hydrodynamic modeling of surface plasmon enhanced photon induced current in a gold grating,” Appl. Phys. Lett. **98**, 191113 (2011)
(5-year IF=3.863; Ranking: 15/118 = 13% in Physics, Applied)
- [5] Cheng-Wen Cheng, Mohammed Nadhim Abbas, Zi-Chang Chang, M. H. Shih*, Chih-Ming Wang, M. C. Wu and Yia-Chung Chang, “Angle-independent plasmonic infrared band-stop reflective filter based on the Ag/SiO₂/Ag T-shaped array,” Opt. Lett. **36**, 1440 (2011)
(5-year IF=3.548; Ranking: 7/78 = 9% in Optics)
- [6] Mohammed Nadhim Abbas, Cheng-Wen Cheng, Yia-Chung Chang*, Min-Hsiung Shih, Hung-Hsin Chen, and Si-Chen Lee, “Angle and polarization independent narrow-band thermal emitter made of metallic disk on SiO₂,” Appl. Phys. Lett. **98**, 121116 (2011)
(5-year IF=3.863; Ranking: 15/118 = 13% in Physics, Applied)
- [7] Mohammed Nadhim Abbas, Cheng-Wen Cheng, Yia-Chung Chang, and Min-Hsiung Shih*, “An omni-directional mid-infrared tunable plasmonic

polarization filter,” Nanotechnology (accepted)

■ **Conference papers**

- [1] Cheng-Wen Cheng (oral), Zi-Chang Chang, Mohammed Nadhim Abbas, M. H. Shih, Chih-Ming Wang, M. C. Wu and Yia-Chung Chang, “*Characterization of the localized surface plasmon polariton mode in Ag/SiO₂/Ag T-shaped array,*” Integrated Photonics Research, Silicon and Nano Photonics (IPR) (2010)

